Nanoscale Thermal Transport with Photons and Phonons

Thesis by

Ding Ding

In Partial Fulfillment of the Requirements

for the Degree of

Doctor of Philosophy

California Institute of Technology

Pasadena, California

2017

(Defended March 8, 2016)

Abstract

Recent progress in nanosciences challenges the conventional understanding of Fourier's law for heat conduction and Planck's law for thermal radiation, calling for theoretical and experimental advancement to improve our understanding at these length scales. Advances in both theoretical and experimental progress at these length scale have been made in the past two decades, but there are still many challenges and possibilities in further understanding how heat conducts or radiates at these length scales.

The first half of this thesis focuses on topics in nanoscale thermal radiation. First, we will discuss an effort to modify thermal emission using a hyperbolic metamaterial (HMM). Recent efforts in utilizing different metamaterial designs to modify thermal emission has led to greater control over the spectral and directional properties of thermal radiation, and the HMM is one such metamaterial. HMM is typically made up of sub-wavelength alternating layers of metal and dielectric that result in an anisotropic permittivity. Here we demonstrate that an annular, transparent HMM lens enables selective controlling of the plasmonic resonance such that a nanowire emitter, surrounded by an HMM, appears dark to incoming radiation from an adjacent nanowire emitter unless the second emitter is surrounded by an identical lens.

While many metamaterial schemes exist to modify thermal emission, these schemes are ultimately limited by the maximum possible emission of a blackbody. In an effort to further increase radiative thermal emission, we made another effort to explore the possibility of removing the enhanced but trapped thermal radiation energy density at sub-wavelength distances. Here, we propose and numerically demonstrate an active scheme that exploits the monochromatic nature of near-field thermal radiation to

drive a transition in a laser gain medium, which, when coupled with external optical pumping, allows the resonant surface mode to be emitted into the far-field. We compare this proposed active radiative cooling (ARC) approach to the better-understood laser cooling of solids (LCS) technique, which achieves cooling by extracting phonons instead of thermal radiation. We show that LCS and ARC can be described with the same mathematical formalism and find that ARC can achieve higher efficiency and extracted power over a wide range of conditions.

In the second half of thesis, we switch our attention to nanoscale heat conduction where phonons are the dominant heat carriers. Phonons require a medium to travel, unlike thermal radiation, and thus experience much stronger interaction with the medium. Typical assumptions of many scattering events of phonons at the larger length scales break down at the nanoscale when phonon transport can no longer be accurately described by diffusion theory. Here, we present a numerical modeling effort using the Boltzmann Transport Equation to accurately model nanoscale phonon transport of a recent experiment. We show a calculated trend of pump beam size dependence on thermal conductivity similar to results from the time-domain thermal reflectance (TDTR) experiment. We also identify the radial suppression function that describes the suppression in heat flux, compared to Fourier's law, that occurs due to quasiballistic transport and demonstrate good agreement with experimental data.

While time-domain thermal reflectance (TDTR) experiment is widely used to characterize thermal transport, it is not ideal for in-plane thermal measurements compared to the transient grating (TG) techniques which utilize interference of two beams to create a in-plane grating pattern for thermal measurements. In the last part of my thesis, we highlight details of an experimental effort to develop the ultrafast transient grating (TG) technique capable of measuring fast thermal decays. We will then highlight the results of thermal and acoustic measurements of molybdenum disulphide that can be obtained from this technique. Our results are in good agreement with other measurements and calculations.

With nanosciences paving way for the future of technology, understanding thermal management at the nanoscale is crucial for device performance and reducing energy

waste. We believe that these results in thermal radiation and conduction will benefit thermal management at the nanoscale.

Published Content and Contributions

Ding, D. et al. (2014). "Radial quasiballistic transport in time-domain thermoreflectance studied using Monte Carlo simulations. Applied Physics Letters, 104(14), 143104. doi:10.1063/1.4870811

D.D. participated in the conception of the project, solved and analyzed the results, prepared the data, and participated in the writing of the manuscript.

Ding, D., & Minnich, A. J. (2015). "Selective radiative heating of nanostructures using hyperbolic metamaterials". Optics Express, 23(7), A299A308. doi:10.1364/OE.23.00A299

D.D. participated in the conception of the project, solved and analyzed the results, prepared the data, and participated in the writing of the manuscript.

Zhang, H., Hua, C., Ding, D., & Minnich, A. J. (2015). "Length Dependent Thermal Conductivity Measurements Yield Phonon Mean Free Path Spectra in Nanostructures". Scientific Reports, 5, 9121. doi:10.1038/srep09121

D.D. participated in solving and analyzed of the results.

Ding, D. et al. (2016). "Active thermal extraction of near-field thermal radiation". Physical Review B, 93(8), 081402. doi:10.1103/PhysRevB.93.081402

D.D. participated in the conception of the project, solved and analyzed the results, prepared the data, and participated in the writing of the manuscript.

Ding, D. et al. (2016). "Active Thermal Extraction and Temperature Sensing of Near-field Thermal Radiation". Scientific Reports, 6, 32744. doi:10.1038/srep32744

D.D. participated in the conception of the project, solved and analyzed the results, prepared the data, and participated in the writing of the manuscript.

Dedication

To my wife, moms, dads and fellow siblings

Acknowledgements

My time at Caltech has been a rewarding experience. The opportunity to learn and work with very outstanding individuals has allowed me to learn and be independent in my scientific pursuits. Professor Austin Minnich has been an extremely patient and understanding adviser and I'm especially grateful for his support and encouragement. Scientifically, Austin has always been eager to spend his time discussing problems with me and pointing out basic scientific sanity checks that have been extremely helpful in solving the problems I faced. The members of the Minnich group, past and present, have also been extremely helpful in every way. Hang Zhang and Xiangwen Chen have been great collaborators in works that I'll present here. Chengyun Hua and Navaneetha Krishnan Ravichandran have been very helpful in various aspects of my research and I would like to thank them both sincerely. Also my thanks to Nate Thomas for characterization samples, Nick Dou for many discussions, and Andrew Robbins for all the fun group activities. Many thanks to Taeyong Kim for his various contributions to the thermal radiation project and the transient grating experimental measurements.

Outside the group, my interactions with the EFRC (Energy-Frontier Research Center) and JCAP (Joint-Center for Artificial Photosynthesis) have been equally rewarding. Many thanks to Stefan Omelchenko and Dennis Friedrich for reviving the optics lab (G141b) in JCAP. Without both of you the experiment would not have been possible. Many thanks to Darius Torchinsky and Hao Chu for their tips for my experiment. I'm also very grateful to Professor Jho and his group members at GIST for the samples and sample characterizations. Thanks to Ke Sun, Michael Lichtman, and Jesus M. Velazquez for various characterization samples. Last but not least,

I would like to thank Professor Atwater for allowing the Minnich Group to use the laser facility in JCAP and for being on my committee. I would like to thank Professor Vahala, Professor Fultz, Professor Faraon, and Professor Bernardi for agreeing to be on my PhD committee. I would also like to thank Professor Bellan for discussions on my research work in hyperbolic metamaterials and Dr. Andreas Pusch of Imperial College for discussions in active thermal extraction. Finally, I would like to thank my undergraduate advisor Professor Rashid Zia who has been a role model and great mentor over the years.

My first two-and-half years were spent in the Kimble Group and I would like to thank Professor Kimble for his mentorship and guidance over those years. I would also like to thank all past and present members of the Kimble group whom I have worked closely with.

Finally, I would like to thank my family for being so supportive over all these years away from home and to my wife Bilin for her utmost support over the years.

Contents

List of Figures

List of Tables

Chapter 1

Introduction

1.1 Current Issues in Thermal Transport

1.1.1 Introduction

Thermal radiation and thermal conduction are two primary forms of heat transport. Thermal radiation involves the transfer of heat through electromagnetic waves or photons, while thermal conduction in solids involves lattice vibrations, which are known as phonons. Thermal radiation typically occurs in a vacuum and thus will not experience scattering unlike phonons propagating in solids. As a result, the description of thermal radiation as rays does not apply to phonons at macroscopic length scales. Likewise, the low density of states for photons in vacuum compared to the much higher density of states for phonons in solids makes heat transfer by radiation much less effective than conduction.

Recent progress in nanosciences have, however, challenged our conventional understanding of thermal radiation and heat conduction. Thermal radiation at the nanoscale can experience vast changes in density of states, greatly increasing the heat transfer what the well-known Stefan-Boltzmann law predicts. Thermal conduction can occur at length scales where scattering is no longer so frequent and the phonons starts to behave like rays in thermal radiation. In this chapter, we will first highlight the progress, issues and challenges in thermal radiation and conduction at the nanoscale and move on to describe the outline of the thesis.

1.1.2 Challenges in Nanoscale Heat Transfer with Photons

Thermal conduction and thermal radiation do share some similarities. First of all, the energy carriers (photons or phonos) always follow the Bose-Einstein distribution. Second, ballistic phonons behave like thermal radiation due to the lack of scattering events in each case. However, the issues surrounding thermal photons are very different from that of thermal phonons. The main reason is because while we are still trying to understand how thermal phonons propagate in a solid, the propagation of thermal photons is much better understood due to the weaker interaction of photon with medium compare to phonons. Thus, current research in thermal radiation focuses on manipulating and engineering radiative heat transfer.

Thermal radiation is electromagnetic waves emitted by bodies at finite temperatures. Engineering thermal radiation is of importance for a number of technologies, including infrared imaging, energy conversion, thermal insulation, thermal signature control, and thermal management [10]. In the far-field, where the distance of separation between bodies far exceeds the thermal wavelength, the blackbody limit governs the maximum radiative flux between two bodies. Recent works have demonstrated that far-field spectral and angular characteristics of thermal radiation can be controlled using photonic crystals [11–13] and metamaterials [14–17]. Also, hyperbolic metamaterials (HMMs) have been under intense investigation for their potential to control thermal radiation. HMMs possess dielectric constants of opposite sign along different axes and hence allow the propagation of high momentum modes within the HMM due to the hyperbolic dispersion [18]. In particular, HMMs have been studied for their potential to enhance near-field heat transfer [19–22] as well as control the spectral and angular distribution of far-field radiation [23–26] and offer potential for other applications in thermal radiation control.

In the near field, radiative heat transfer can be greatly enhanced due to the presence of evanescent waves [27, 28] as shown in Fig. 1.1. Recently, a number of works have demonstrated that near-field radiative heat transfer is enhanced by many orders of magnitude compared to the far-field limit for closely spaced objects with either

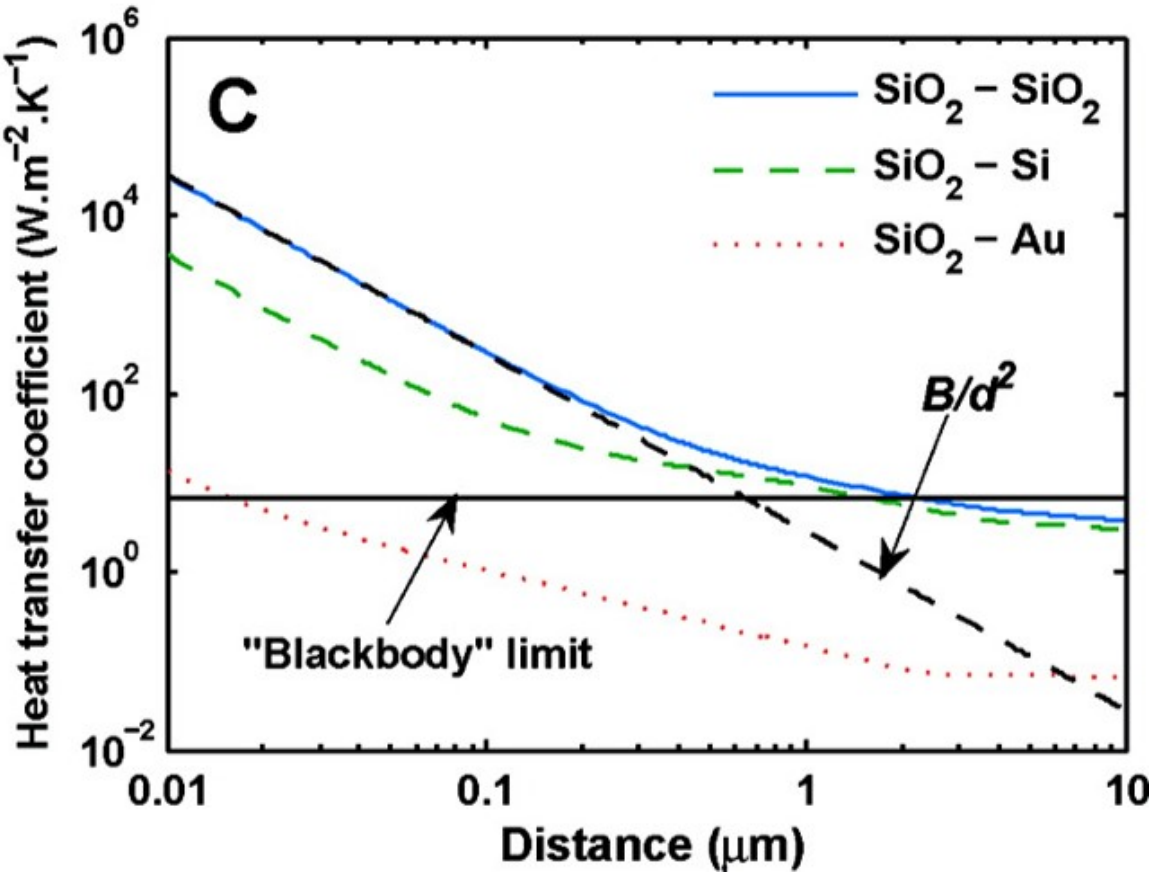

Figure 1.1: Radiative heat transfer coefficients versus the distance between two parallel plates at an average temperature of 300 K. The black solid line is the limit of thermal radiation predicted by the Planck's law, and the dashed line is the asymptotic relation at small gaps (B/d^2). The enhancement in radiative heat transfer by orders of magnitude is especially prominent for the two plates of the same material due to a common surface evanescent wave resonance. Figure taken from Ref. [2]

natural [2, 29] or engineered resonant surface modes [19, 20, 30–32]. There have also been efforts to couple these near-field modes into the far-field with the use of grating structures [33], antennas [34], and a thermal extraction lens [35, 36]. While these techniques have enabled enhanced thermal radiation into the far-field, the strong and monochromatic thermal energy in the near-field can certainly be utilized in many other interesting ways, such as driving transitions in gain medium.

1.1.3 Challenges in Nanoscale Heat Transfer with Phonons

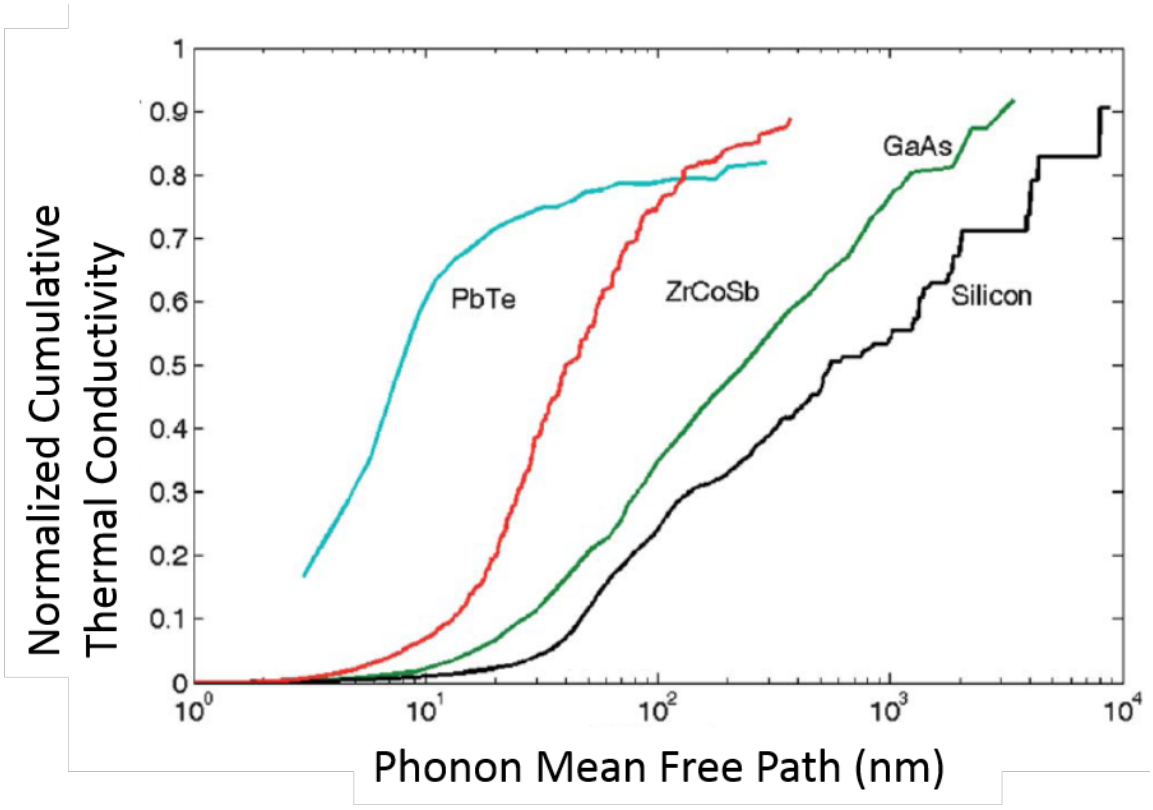

Figure 1.2: Normalized cumulative thermal conductivity at room temperature versus mean free path calculated from first-principles. Figure take from Ref. [3].

Lately, there are still many issues surrounding how thermal phonons propagate in a solid, especially on the length scale comparable to the wavelength and mean-free paths (MFPs) of the phonons [3,37–40]. For phonons, heat transport has traditionally been described by diffusion theory, namely the well-known Fourier's law, which states

that the time rate of heat transfer per unit area through a material is proportional to the negative gradient in the temperature at which the heat flows. Fourier's law is valid as long as the time or length scale of heat transport is much longer than the scattering relaxation time or the scattering mean-free-path (MFP), respectively. However, phonon transport approaching the length scale of its MFP can deviate strongly from the predictions of Fourier's Law [41]. This deviation is due to the lack of scattering events at such short length scales that renders the phonon transport quasi-ballistic instead of diffusive. Recently, some materials such as Si have been predicted [42] and experimentally demonstrated [8, 43] to have long MFPs on the order of μm . Also, materials structured at the length scales of the MFPs have been shown to achieve properties that are not achievable in the bulk form [44–53]. An MFP distribution of phonons such as those in Fig. 1.2 shows the cumulative thermal conductivity as a function of phonon MFP. Ration engineering requires knowledge of phonon MFPs and Fig. 1.2 is very useful especially for engineering thermal conductivity in materials at the nanoscale [54].

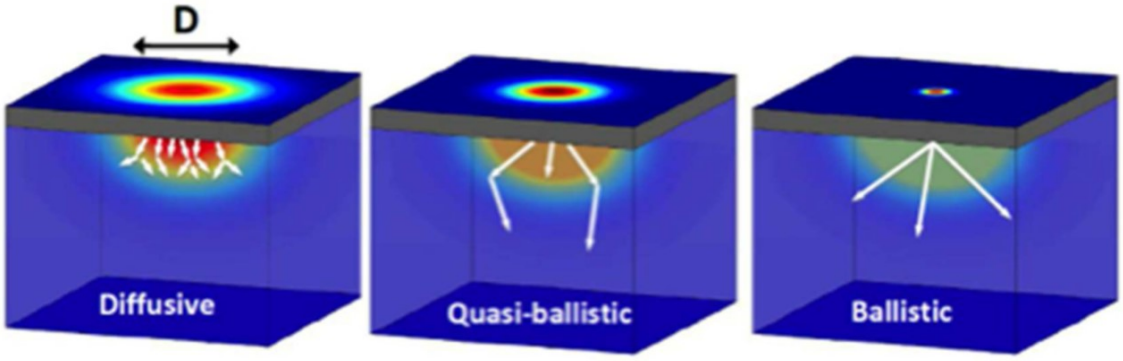

Figure 1.3: Illustration of change from diffusive transport on the left to quasi-ballistic and finally to ballistic transport on the right. This change in transport regime is a result of a change in the pump diameter from being much larger than the MFPs to eventually being smaller than the MFPs. In the quasi-ballistic and ballistic regimes, phonons with long MFPs do not scatter much compared to predictions from Fourier's law and contribute less to the overall thermal conductivity. Figure taken from Ref. [4]

There have been various experimental progress in non-contact optical experimental techniques and materials fabrication has allowed us to predict and measure thermal conductivity of materials [8, 43, 55–60] to acquire the MFP spectrum. Many of these

techniques [8, 55, 58, 60] utilize an ultrafast pump laser pulse to heat up the sample followed by a spatially delayed probe pulse that measures the change in reflectance on the sample surface. As Fourier's law fails when the length scale of heat transport is comparable to phonon MFPs, the basic concept of many experimental techniques involves varying the heating length scale over the range comparable to typical phonon MFPS [8, 55, 58], such as changing the pump beam size shown in Fig. 1.3. The MFP distribution can then be obtained by analyzing the change in measure thermal conductivity as a function of a thermal length scale. However, the interpretation of the measurements to obtain MFP distribution is not always straight-forward and depends largely on the specific geometry of the heating profile.

Another measurement technique that enables accurate interpretation of MFP distribution from experimental measurements is the transient grating (TG) spectroscopy [43, 61]. In this technique, interference from two laser beams results in formation of a one-dimensional grating geometry on the sample and the thermal length scale is the grating wavelength. This technique is much more sensitive to in-plane thermal transport than other pump probe techniques and has been used to measure thermal diffusion of superlattices [62] and novel materials such as nuclear materials [63]. More effort to further develop and utilize this technique for measurements of fast thermal processes will be of great interest.

1.2 Outline of the Thesis

Despite the above-mentioned advances, there are still many unresolved issues in both areas of thermal transport. For phonons, one primary challenge is to develop methods to better retrieve phonon MFP spectrum from experimental measurements. For photons, the challenge primarily lies in how to utilize and manipulate the thermal radiation both in the far-field and near-field. Interesting far-field manipulation is possible with the advent of HMMs. Also, while many efforts have been made to engineer near-field interaction, controlling near-field thermal radiation in novel ways can potentially allow us to circumvent conventional limits in the far-field.

The purpose of this thesis is to explore the physics of nanoscale thermal transport with phonons and photons and to determine ways to better understand and manipulate these energy carriers. The first half of the thesis focuses on developing techniques to manipulate thermal radiation. Chapter 2 discuss how we use an annular transparent HMM to enable selective heating of a sub-wavelength plasmonic nanowire by controlling the angular mode number of a plasmonic resonance. We find that a nanowire emitter, when surrounded by an HMM, appears dark to incoming radiation from an adjacent nanowire emitter unless the second emitter is surrounded by an identical lens such that the wavelength and angular mode of the plasmonic resonance match.

In Chapter 3, we propose and numerically demonstrate an active scheme to extract near-field thermal radiation to the far-field. Our approach exploits the monochromatic nature of near-field thermal radiation to drive a transition in a laser gain medium, which, when coupled with external optical pumping, allows the resonant surface mode to be emitted into the far-field. We modeled a typical gain medium and found strong near-field coupling limits our cooling efficiency. We thus proposed a way to circumvent the issue, leading to almost ideal cooling efficiencies. Then, we compare our scheme to laser cooling of solids and found that our scheme can potentially outperform laser cooling of solids under certain conditions.

The next half of my thesis focuses on issues in thermal transport with phonons. Chapter 4 studies phonon MFP spectroscopy in TDTR experiments. We use Monte-Carlo solution to the Boltzmann Trasnport Equation to obtain a similar trend of how thermal conductivity varies with pump beam diameter in TDTR. From this trend, we identify the radial suppression function that describes the suppression in heat flux, compared to Fourier's law, that occurs due to quasi-ballistic transport and demonstrate good agreement with experimental data.

Alongside the numerical effort to construct MFP spectrum for TDTR experiments, we also devote a large amount of effort to developing experimental techniques for fast thermal processes. In Chapter 5, we outline an experimental effort for an ultra-fast transient grating technique that combines the merits of the transient grating setup

and the time resolution achieved in TDTR for better detection of fast thermal processes. This technique is well-suited for novel materials with high in-plane thermal conductivity. Chapter 6 outlines results of experimental measurements of molybdenum disulphide from the ultrafast transient grating setup.

Finally, Chapter 7 summarizes the possibilities for future work and concludes the thesis.

Chapter 2

Selective Radiative Heat Transfer Using Hyperbolic Metamaterials

Contents of this chapter can also be found in Ref. [64].

2.1 Introduction

Engineering thermal radiation is of importance for a number of technologies, including infrared imaging, energy conversion, thermal insulation, thermal signature control, and thermal management [10]. Recent works have demonstrated that far-field spectral and angular characteristics of thermal radiation can be controlled using photonic crystals [11–13] and metamaterials [14–17]. These structures can also enable near-field resonant surface modes to propagate into the far-field using gratings [33] and antennas [34] to out-couple surface modes. In the near field, radiative heat transfer can be greatly enhanced due to the presence of evanescent waves [27, 28]. These enhancements have recently been demonstrated experimentally [2,29,65,66]. Thermal radiation into the far-field can also be enhanced in a thermal extraction scheme in which an impedance-matched extraction device allows the propagation of internally reflected modes [35].

Recently, hyperbolic metamaterials (HMMs) have been under intense investigation for their potential to control thermal radiation. HMMs possess dielectric constants of opposite sign along different axes and hence allow the propagation of high momentum modes within the HMM due to the hyperbolic dispersion [18]. HMMs can

be fabricated in practice as a multilayer stack with alternating materials of opposite sign of dielectric constant. HMMs were originally of interest for their potential to project images with resolution below the diffraction limit into the far-field, as proposed theoretically [67, 68] and later demonstrated experimentally [69]. For thermal radiation, HMMs have been studied for their potential to enhance near-field heat transfer [19–22] as well as control the spectral and angular distribution of far-field radiation [23–26].

Here, we examine how HMMs modify the far-field thermal emission spectrum of nanostructures. We find that a lossy plasmonic nanowire surrounded by a transparent, annular HMM lens yields thermal emission that primarily occurs only at a specific wavelength and angular mode number and greatly exceeds that of the nanowire alone. This angular mode resonance enables highly selective radiative heating because only nanowires that are surrounded by identical HMM lenses can exchange radiation, as illustrated in Fig. 2.1.

In this chapter, we begin by introducing the details of the transfer matrix method (TMM) in cylindrical coordinates and how it is used to simulate our structure. Then, we discuss the nature of the angular-mode-dependent resonances and how we achieve selective heating. Lastly, we examine the effects of losses on the scheme.

2.2 Transfer Matrix Method in Cylindrical Coordinates

TMM is ubiquitous for calculations of planar layered structures. However, its application in cylindrical coordinates has not been so widely used. Refs. [70–72] use this method for calculating cylindrically-shaped Bragg reflectors for lasers. In this section, we will go through the details of the TMM in cylindrical coordinates as outlined in Refs. [70–72] .

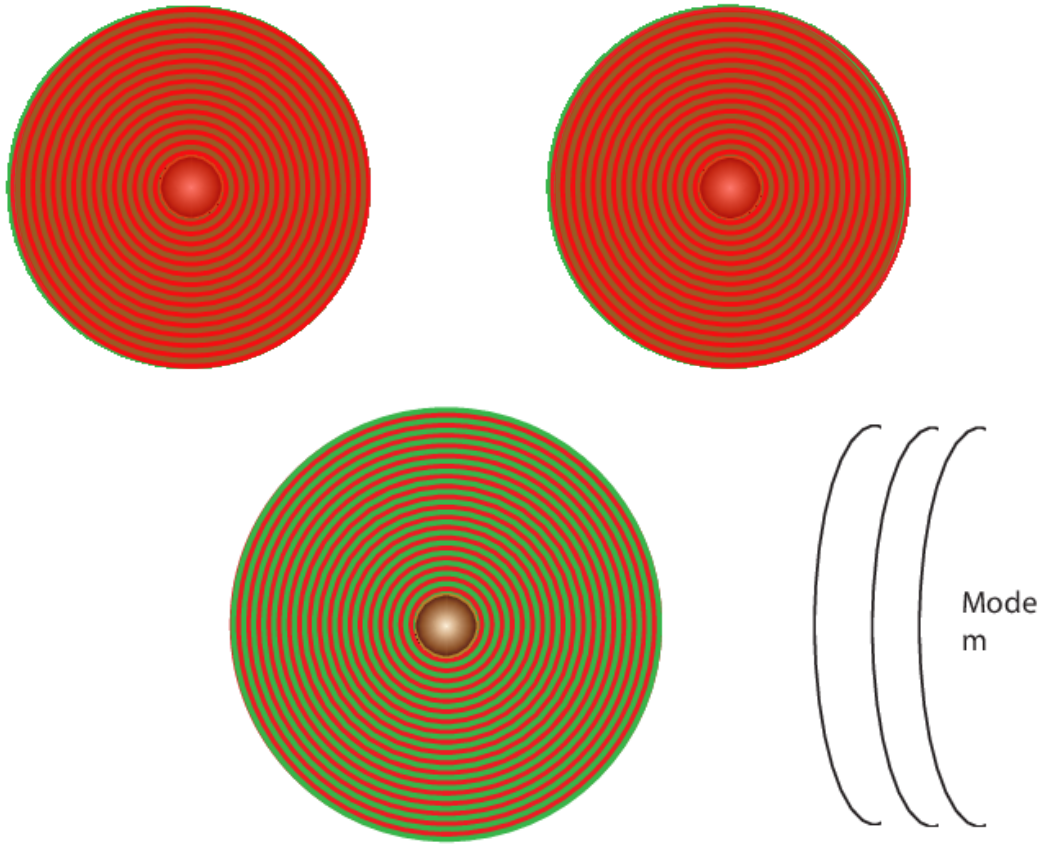

Figure 2.1: A nanowire emitter, surrounded by an HMM, appears dark to incoming radiation from an adjacent nanowire emitter, unless the second emitter is surrounded by an identical lens such that the wavelength and angular mode of the plasmonic resonance match.

2.2.1 Bessel and Hankel Functions

From Maxwell's equations, we can obtain Laplace equation for electromagnetic waves in cylindrical coordinates as [73]

$$\frac{\partial^2\Phi}{\partial\rho^2}+\frac{1}{\rho}\frac{\partial\Phi}{\partial\rho}+\frac{1}{\rho^2}\frac{\partial^2\Phi}{\partial\phi^2}+\frac{\partial^2\Phi}{\partial z^2}=0 \tag{2.1}$$

Using separation of variables and solving the z and ϕ dependent functions from Eq. 2.1,

$$\Phi(\rho,\phi,z) = e^{\pm\beta z}e^{\pm im\phi}R(\phi) \tag{2.2}$$

$$\frac{d^2R}{dx^2} + \frac{1}{x}\frac{dR}{dx} + (1 - \frac{m^2}{x^2})R = 0 \tag{2.3}$$

where R is the solution from Eq. 2.3 with $x = \beta\rho$. The solution to this differential equation are Bessel functions of the first and second kind $J_m(x)$ and $Y_m(x)$ respectively. One can also take linear combinations of them that will still be a solution to Equation 2.3. These functions are $H_m^{(1)}(x) = J_m(x) + iY_m(x)$ and $H_m^{(2)}(x) = J_m(x) - iY_m(x)$ which are known as Hankel functions of the first and second kind. One useful fact about these functions is its behavior at large values of x [73]

$$J_m(x) \to \sqrt{\frac{2}{\pi x}}\cos(x - \frac{m\pi}{2} - \frac{\pi}{4}) \tag{2.4}$$

$$Y_m(x) \to \sqrt{\frac{2}{\pi x}}\sin(x - \frac{m\pi}{2} - \frac{\pi}{4}) \tag{2.5}$$

$$H_m^{(1)}(x) \to \sqrt{\frac{2}{\pi x}}\exp(i(x - \frac{m\pi}{2} - \frac{\pi}{4})) \tag{2.6}$$

$$H_m^{(2)}(x) \to \sqrt{\frac{2}{\pi x}}\exp(-i(x - \frac{m\pi}{2} - \frac{\pi}{4})) \tag{2.7}$$

2.2.2 Mathematical Form of Transfer Matrices

We begin by considering a lossy nanowire core of radius a that is in optical contact with a lens medium in vacuum, as shown in the inset of Fig. 2.2(a). The system is assumed to be infinite in the z direction with the polarization such that $\mathbf{E} \perp z$. The magnetic field $H_z(\vec{r})$ from an incident plane wave can be expressed as

$$H_z(\vec{r}) = \begin{cases} \sum_{m=-\infty}^{\infty}(i)^m\left(J_m(k_0\rho) - a_m H_m^{(1)}(k_0\rho)\right)\exp(im\phi): & \rho > b \\ \sum_{m=-\infty}^{\infty}(i)^m\left(c_m^{(j)}J_m(k_j\rho) + d_m^{(j)}H_m^{(1)}(k_j\rho)\right)\exp(im\phi): & a < \rho < b \\ \sum_{m=-\infty}^{\infty}(i)^m b_m J_m(k_1\rho)\exp(im\phi): & \rho < a \end{cases} \tag{2.8}$$

where J_m and $H_m^{(1)}$ are Bessel and Hankel functions of the first kind of angular mode number m in cylindrical coordinates [70] and a_m and b_m are the coefficients of the Hankel function of the scattered field in outermost vacuum ($\rho > b$) and the Bessel function of the transmitted field of core ($\rho < a$), respectively. $c_m^{(j)}$ and $d_m^{(j)}$ are the coefficients for the Bessel and Hankel function of the field in the jth layer, and k_j denotes the wave vector of each jth layer up to the core, where $j = 1$. k_0 denotes the wave vector in vacuum.

The coefficients a_m, b_m, $c_m^{(j)}$, and $d_m^{(j)}$ can be solved by matching boundary conditions of tangential fields at the boundary of each layer using the Transfer Matrix Method (TMM) in cylindrical coordinates [70–72]. To do so, we first use Maxwell's Curl equations [70]

$$E_\phi(r) = \frac{i}{k^2}\omega\mu\frac{\partial H_z(r)}{\partial\rho} \tag{2.9}$$

to obtain the ϕ component of the electric field from the magnetic field in Eq. 2.8. Then, using the continuity of H_z, E_ϕ between layer j and $j+1$ at an interface located at ρ_j, we obtain

$$c_m^{(j)}J_m(k_j\rho_j) + d_m^{(j)}H_m^{(1)}(k_j\rho_j) = c_m^{(j+1)}J_m(k_{j+1}\rho_j) + d_m^{(j+1)}H_m^{(1)}(k_{j+1}\rho_j) \tag{2.10}$$

$$\frac{1}{k_j^2}\left(\omega\mu k_j\left(c_m^{(j)}J_m'(k_j\rho_j) + D_jH_m^{(1)'}(k_jR_j)\right)\right) =$$
$$\frac{1}{k_{j+1}^2}\left(\omega\mu k_{j+1}\left(c_m^{(j+1)}J_m'(k_{j+1}R_j) + d_m^{(j+1)}H_m^{(1)'}(k_{j+1}R_j)\right)\right) \tag{2.11}$$

Now, we write Eqs. 2.10 and 2.11 in matrix form as

$$M(m, k_{j+1}, \rho_j)\begin{pmatrix} c \\ d \end{pmatrix}_{m,j+1} = M(m, k_j, \rho_j)\begin{pmatrix} c \\ d \end{pmatrix}_{m,j} \tag{2.12}$$

where

$$M(m, k, \rho) = \begin{bmatrix} J_m(k\rho) & H_m^{(1)}(k\rho) \\ \frac{1}{k}J_m'(k\rho) & \frac{1}{k}H_m^{(2)'}(k\rho) \end{bmatrix} \tag{2.13}$$

in Eq. 2.12 such that

$$\begin{pmatrix} c \\ d \end{pmatrix}_{m,j+1} = M^{-1}(m, k_{j+1}, \rho_j) M(m, k_j, \rho_j) \begin{pmatrix} c \\ d \end{pmatrix}_{m,j} = T(m, k_j, k_{j+1}, \rho_j) \begin{pmatrix} c \\ d \end{pmatrix}_{m,j} \tag{2.14}$$

We can also obtain a similar set of expressions like Eqs. 2.13 and 2.14 for the case where the electric field $\mathbf{E} \parallel z$.

2.2.3 Computing Emissivity Using Transfer Matrices

The absorption efficiency Q_{abs} can then be expressed as

$$Q_{abs} = \sum_{m=-\infty}^{\infty} Q_{abs,m} = \frac{2}{k_0 a} \sum_{m=-\infty}^{\infty} \mathrm{Re}(a_m) - |a_m|^2 \tag{2.15}$$

where $Q_{abs,m}$ is the partial absorption efficiency or absorption efficiency per mode and $\mathrm{Re}(a_m)$ is the real part of the coefficient for mode m defined in Eq. 2.8 according to Mie theory [74, 75]. By Kirchoff's law, the absorptivity equals the emissivity for each direction and wavelength [76], and hence Q_{abs} can be interpreted as the emissivity. Note that the emissivity can exceed unity for subwavelength objects because the absorption cross-section can be larger than the geometric cross-section [75].

To obtain a_m in Eq. 2.15, we need to use TMM by solving Eq. 2.14 for each layer. For instance, if we start from starting from the first layer with ($j = 1$ and $\rho < a$) to the outermost layer ($j = N$ and $\rho > b$) in Eq. 2.8, we can successively apply Eq. 2.14 to form the following matrix equation

$$\begin{pmatrix} b_m \\ 0 \end{pmatrix} = T_{1,N} \begin{pmatrix} 1 \\ -a_m \end{pmatrix} \tag{2.16}$$

such that $T_{1,N} = T(m, k_N, k_0, \rho_N)...T(m, k_2, k_3, \rho_2)T(m, k_1, k_2, a)$.

Then we can solve for a_m using

$$a_m = -\frac{T_{1,N}(2,1)}{T_{1,N}(2,2)} \tag{2.17}$$

where $T_{1,N}(p,q)$ represent the matrix element in the pth row and qth column of $T_{1,N}$.

In the following section, we will highlight some of the results that we obtain using TMM.

2.3 Results and Discussion

2.3.1 Absorption of nanowire and annular HMM lens

The HMM lens consists of an alternating layered structure of dielectric and metal leading to anisotropic permittivity along the radial and tangential direction. These anisotropic dielectric constants can be expressed using effective medium theory (EMT) according to $(\epsilon_\rho, \epsilon_\theta) = (\epsilon_m\epsilon_d/\left((1-f)\epsilon_m + f\epsilon_d\right), f\epsilon_m + (1-f)\epsilon_d)$, where f is the volume fraction occupied by the metal and ϵ_m, ϵ_d are the respective metal and dielectric permittivities [67]. We assume the lens to be lossless and define Q_{abs} with respect to the core radius a. Neglecting loss in the lens means that the lens cannot exchange thermal radiation with the core, and thus its contribution to heat transfer can be neglected.

First, we consider the emissive properties of only the nanowire core of radius a in a vacuum without any lens. Figure 2.2(a) shows the computed emissivity Q_{abs} for the nanowire core with a permittivity of $-1.05 + 0.01i$ and $a = 0.1\lambda$, where λ is the wavelength of the incident field. We choose the core permittivity close to the ideal plasmonic resonance condition to demonstrate our result but other negative real permittivity values can be chosen with similar results. We assume a typical wavelength $\lambda = 10$ μm, corresponding to the maximum of the blackbody spectrum around 290 K, giving $a = 1$ μm and yielding an emissivity of 0.5. The maximum emissivities for the nanowire core decrease with increasing size parameter as the absorption efficiency scales as $1/a$. Note that plasmonic resonances do occur at specific sizes for a given

permittivity for a nanowire core [77], but tuning the angular mode number of the resonance requires changing the permittivity of the nanowire.

Now, consider the nanowire surrounded by a transparent material called the "lens" as shown in the inset of Fig. 2.2(a). The transparent lens is assumed to be lossless such that it cannot exchange radiation with the core. The total thickness of the core and lens b considered in Fig. 2.2(a) ranges from $1-7$ μm with corresponding size parameters $k_0 b$ shown. We assume that a vacuum gap of width $\lambda/200$ (50 nm for $\lambda = 10$ μm) exists to prevent heat conduction, although this assumption does not affect our conclusions. The addition of this lens with a lossless metal of permittivity $\epsilon = -1.05$ or a dielectric of permittivity $\epsilon = 10$ results in a lower emissivity Q_{abs} than the bare core (Core-Vacuum) case. This reduction in emissivity can be attributed to the impedance mismatch between the lens and vacuum that reflects some modes before they reach the absorptive core.

Next, consider the nanowire surrounded by a transparent HMM lens. We compute a_m in this case using either EMT or considering each individual layer of the HMM with a transfer matrix. For the EMT-HMM case, we scale m in Eq. 2.8 of the HMM layer [78] to $m' = m\sqrt{\epsilon_\theta/\epsilon_\rho}$. Thus, there are only three interfaces ($N = 3$ in Eq. 2.16) including the air gap in the TMM calculations. For the layer by layer case, the thickness of each metal-dielectric bi-layer is chosen to be $\lambda/400$ (25 nm for $\lambda = 10$ μm). We examine both the metal-dielectric (TMM-md) and dielectric-metal (TMM-dm) structures such that the first layer adjacent to the core is a metal or a dielectric, respectively. For the EMT-HMM case, we take the optical constants to be $(\epsilon_\rho, \epsilon_\theta) = (10, -0.025)$ according to EMT. For the TMM calculation, we take $(\epsilon_m, \epsilon_d) = (-5.1, 3.4)$ with $f = 0.4$, giving the same values of $(\epsilon_\rho, \epsilon_\theta) = (10, -0.025)$ as EMT.

This calculation is plotted in Fig. 2.2(a). In contrast to the decrease of emissivity Q_{abs} with the metal and dielectric lens, the emissivity Q_{abs} with the HMM lens exhibits strong peaks as the size parameter increases for both the EMT and TMM calculations. The emissivity Q_{abs} peaks in the TMM-md and TMM-dm cases are in close proximity to the right and left of the EMT-HMM peaks, respectively, and converge to the EMT

result as the layer thickness decreases. Thus, by placing an HMM lens of the right size at one of these peaks around the core, the emissivity can be increased by about three times compared to the same bare nanowire core. Larger enhancements of 4-5 times relative to the bare core can be achieved at larger core sizes for the same loss of the core. Enhancements greater than 50 times that of a larger bare core can be achieved if the loss of the core is optimized but the required small loss is not realistic for any available plasmonic materials and thus is not considered further.

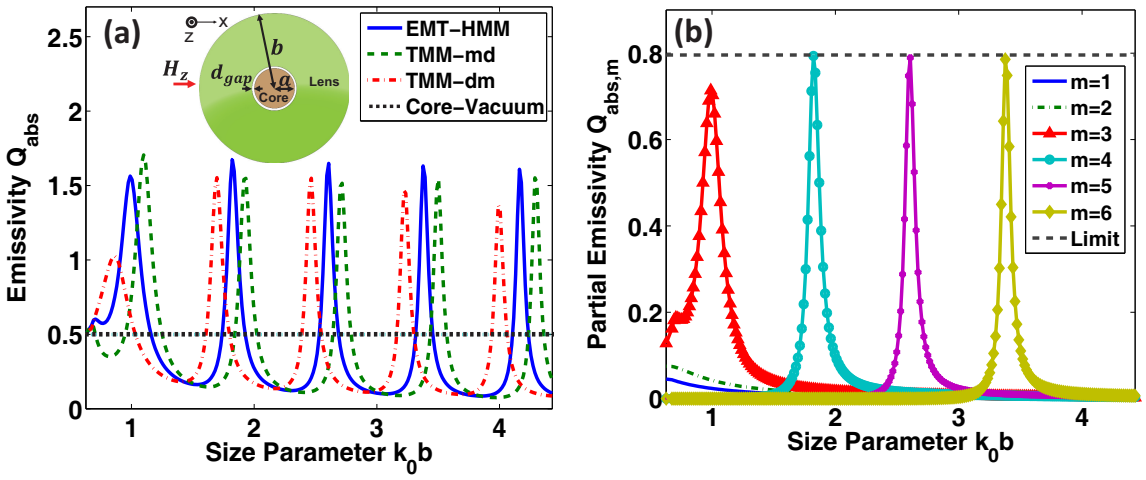

Figure 2.2: (a) Absorption efficiency, or equivalently emissivity, versus size of lens b for core size of $a = 0.1\lambda$ with different lenses surrounding a plasmonic core. Core-Vacuum (black dotted line) indicates Q_{abs} of only a core of size a. Q_{abs} for the core-HMM lens calculated using EMT, TMM-md, and TMM-dm are shown as the dark blue solid, green dashed, and the red dotted-dashed line, respectively. There are many resonant peaks that enhance the emissivity over that of the bare core when the HMM lens is present. Inset: Schematic of the geometry. The core and the lens have radius a and b, respectively. (b) Partial contribution to total absorption efficiency for each angular mode m in (a). The dashed black line is the single-channel limit defined in the text. The mode $m = 4$ achieves the single channel limit, unlike $m = 3$.

2.3.2 Angular-mode specific resonances

To understand the origin of these peaks, we examine the decomposition of absorptivity from the EMT-HMM case in Fig. 2.2(a) into partial absorptivity for modes $m = 1$ to $m = 6$, as shown in Fig. 2.2(b). The $m = 1$ and $m = 2$ cases do not have

resonant peaks for the given size range but modes $m = 3$ to $m = 6$, each have a specific resonance at different size parameters $k_0 b$. These resonant size parameters correspond to the same peak positions in Fig. 2.2(a) and achieve emissivity close to the well-known single channel limit [34]. At a given size parameter, most of the total absorption cross-section is due to a single resonant angular mode.

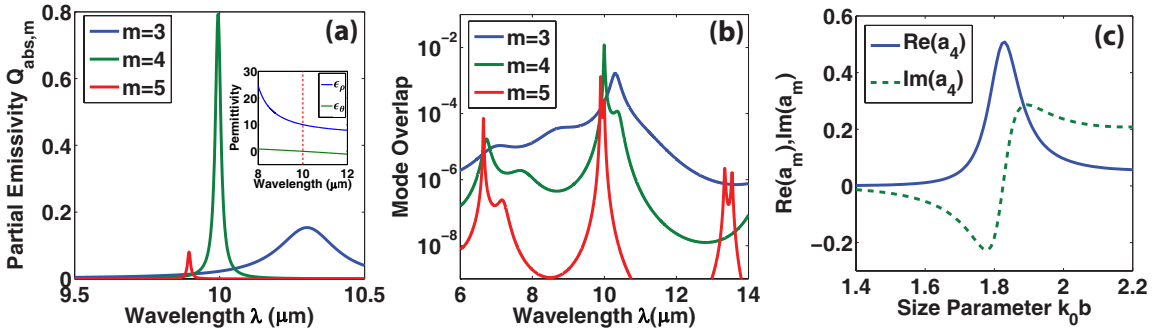

Figure 2.3: (a) Partial emissivity versus wavelength assuming that all optical properties follow a Drude model. Only a few angular modes contribute to radiative transfer at specific wavelengths. Inset: relative permittivities $(\epsilon_\rho, \epsilon_\theta)$ of the HMM lens for the range of wavelengths considered. The red dashed line at 10μm indicates the permittivities used in Fig. 2.2. (b) Product of partial emissivity $Q_{abs,m}$, as in (a), versus wavelength for two size parameters $k_0 b = 2.6$ and $k_0 b = 1.8$ for the modes $m = 3, 4, 5$. There is very little overlap of all modes as two systems do not share an angular mode resonance. (c) Real and imaginary part of a_m defined in Eq. 2.8 for $m = 4$ in Fig. 2.2. This angular mode satisfies the condition for single-channel limit at the chosen size parameter of $k_0 b = 1.8$.

Further, assuming a Drude model for optical properties, this resonance yields by far the largest emissivity over a considerable range of wavelength. We examine the wavelength dependence of the enhancement in thermal emission that can be achieved using the HMM lens using a Drude model given by $\epsilon_m = 1 - \omega_p^2/(\omega^2 + i\gamma\omega)$, where ω is the frequency and ω_p is the plasmon frequency. For the core, $\gamma = 0.0035\omega_p$ and $\lambda_p = 2\pi c/\omega_p = 7$ μm. The metal in the HMM is assumed to have a Drude dispersion that is lossless ($\gamma = 0$) and $\lambda_p = 4.05$ μm. These parameters yield the same permittivities as used in Fig. 2.2 at a wavelength $\lambda = 10$ μm as shown in the inset in Fig. 2.3(a). The partial emissivity $Q_{abs,m}$ versus wavelength for size parameter $k_0 b = 1.8$, at the resonance for $m = 4$, is plotted in Fig. 2.3(a). At a particular wavelength, the emissivity is nearly entirely due to a single angular mode;

for example, the resonant peak at 10 μm is nearly completely due to $m = 4$ mode, with a small additional contribution from $m = 3$ but not from $m = 5$.

We now compare the overlap of these resonances for identical nanowires surrounded by HMM lenses of different size parameters by multiplying the partial emissivity $Q_{abs,m}$ from Fig. 2.3(a) for two different size parameters, $k_0 b = 2.6$ and $k_0 b = 1.8$, for modes $m = 3, 4, 5$. As shown in Fig. 2.3(b), there is negligible overlap between the partial emissivity of the two cases over the full range of the blackbody spectrum at 290 K. Although not plotted, negligible overlap also occurs for higher order modes $m > 6$. Physically, this small overlap indicates that little of the emitted radiation from a core lens system of size $k_0 b = 1.8$ will be absorbed by a core lens system of a size parameter $k_0 b = 2.6$ and vice versa.

We thus arrive at the principal result of our study. Nanowires surrounded by HMM lenses interact with radiation primarily at a particular wavelength and angular mode with absorptivity that can reach the single channel limit. Therefore, radiation emitted by a nanowire with a certain HMM lens can only minimally exchange radiative heat with other identical nanowires surrounded by lenses of different size parameters. Unlike other selective heating schemes based on plasmonic resonances [79–83], the selective resonance identified here is based both on wavelength and angular mode number, enabling high selectivity. This effect is harder to realize with the plasmonic resonances of the bare nanowire alone because achieving similar mode selectivity close to the single channel limit requires tuning both size parameter or material permittivity of the nanowires, while all material properties remain fixed with our core-lens system.

2.3.3 Origin of angular selectivity

We investigate the origin of the angular selectivity by comparing the observed resonance with previous applications of curvilinear HMMs as hyperlenses [67,69]. Hyperlenses are used to convert high angular momentum, evanescent modes to propagating modes using conservation of angular momentum as the mode propagates radially outward. The mode becomes propagating inside the HMM lens when size parameter

$k_0 b \geq m$. However, $k_0 b$ is 1.8 for the $m = 4$ mode on resonance in Fig. 2.2(a), indicating that the excitation in vacuum is actually evanescent. This observation indicates that the HMM lens here is modifying the plasmon resonance of the core similar to the mechanism of enhancement in Ng et al. [84] rather than converting evanescent and propagating waves. We confirm that the resonance is plasmonic in nature by noticing that little absorption is observed for the polarization for which $\mathbf{E} \parallel z$.

The origin of the selectivity is also not solely due to the hyperbolic dispersion. HMMs are typically of interest because the hyperbolic dispersion occurs over a broad spectral range, as is the case here. However, Fig. 2(a) and the inset shows that the mode selectivity only occurs around the ϵ_θ close to zero region of the HMM dispersion, making the selectivity narrowband. The angular selectivity thus requires the anisotropic properties of the HMM but also the epsilon-near-zero (ENZ) region of the dispersion along the θ direction.

Next, we examine the angular mode selectivity using the well-known single channel limit for absorption and scattering. Physically, the single-channel limit is achieved when radiative damping and absorptive loss both contribute equally to the absorption efficiency of the mode [85–87]. Mathematically, from Eq. 2.15 the maximum partial absorption cross-section occurs [34] when $\mathrm{Re}(a_m) = 1/2$ and $\mathrm{Im}(a_m) = 0$, yielding $Q_{abs,m} = 1/(2k_0 a)$. For example, when $a = 0.1\lambda$, the limit for partial emissivity is $Q_{abs,m} \approx 0.796$ as indicated in Fig. 2.2(b). Figure 2.3(c) plots the real and imaginary part of the coefficient a_m in Eq. 2.8 for mode $m = 4$ demonstrating that this mode meets the conditions required to reach the single-channel limit for $k_0 b = 1.8$. Likewise, modes $m = 5$ and $m = 6$ reach the single-channel limit in Fig. 2.2(b) and satisfy the same conditions for a_m at their respective resonant size parameters. However, due to the wavelength-dependence of permittivity, the requirements of the single-channel limit for a fixed size parameter can be met for a single angular mode but are unlikely to be satisfied for other angular modes, as in Fig. 2.3(a). This sensitivity of the angular resonance to the conditions of the single-channel limit contributes to the mode selectivity.

We further investigate this modal selectivity by examining the resonant mode

profiles using the TMM calculation. We reconstruct the field profile of $|H_z|$ in 2D for each mode $|m|$ with incident plane wave direction defined in Fig. 2.2(a). Although a_m is symmetric for positive and negative m, we must account for the phase factors $\exp(im\phi)$ to accurately plot the spatial profile. Figures 2.4(a)–2.4(d) show the 2D plots of $|H_z|$ corresponding to three different size parameters in Fig. 2.2(a) for the TMM-md case. The field magnitude $|H_z|$ at resonant size parameters $k_0 b \approx 1.1$ ($|m| = 3$) and $k_0 b \approx 1.9$ ($|m| = 4$) are plotted in Figs. 2.4(a) and 2.4(b), respectively. In Figs. 2.4(c) and 2.4(d), we plot $|H_z|$ for modes $|m| = 3$ and $|m| = 4$, respectively, for an intermediate size parameter $k_0 b \approx 1.62$ that is off resonance. We observe from Figs. 2.4(a) and 2.4(b) that the lobe patterns at the resonant mode number are highly-confined within the HMM lens. In contrast, in Figs. 2.4(c) and 2.4(d) the modes are not confined. Additionally, the fields magnitudes $|H_z|$ in Figs. 2.4(a) and 2.4(b) are higher than in Figs. 2.4(c) and 2.4(d) by a factor between 3 to 4. The strong, localized field intensities in Figs. 2.4(a) and 2.4(b) highlight the modal selectivity of the resonances at specific size parameters.

We can gain further insight into the origin of the thermal emission spectrum by examining the bulk behavior of an equivalent planar structure. We use the planar Transfer Matrix Method (pTMM) to simulate the equivalent bulk HMM structure on a semi-infinite metallic substrate of the same permittivity of $-1.05 + 0.01i$ as the core in Fig. 2.2. The HMM has the same bi-layer thickness of $\lambda/400$ and material arrangement, including the air-gap, as the TMM-md case of the HMM lens calculation in Fig. 2.2. We relate the wavevector component parallel to the vacuum-HMM interface $k_\parallel$ in the planar case to m in the cylindrical case by approximating the mode to lie within the HMM [86] such that $k_\parallel = m/r_{eff}$, where $r_{eff} = (a + b)/2$. The penetration of the modes through the HMM to the absorbing layer can be observed by the non-zero imaginary part of the Fresnel reflection coefficient $\mathrm{Im}(R_p)$ which describes the absorption of the incident evanescent field [88].

We plot $\log[\mathrm{Im}(R_p)]$ obtained from pTMM against the normalized parallel wave vector $k_\parallel/k_0$ and number of HMM bi-layers N in Fig. 2.5(a). As N increases, the position of maximum $\mathrm{Im}(R_p)$ decreases from the metal-vacuum surface plasmon con-

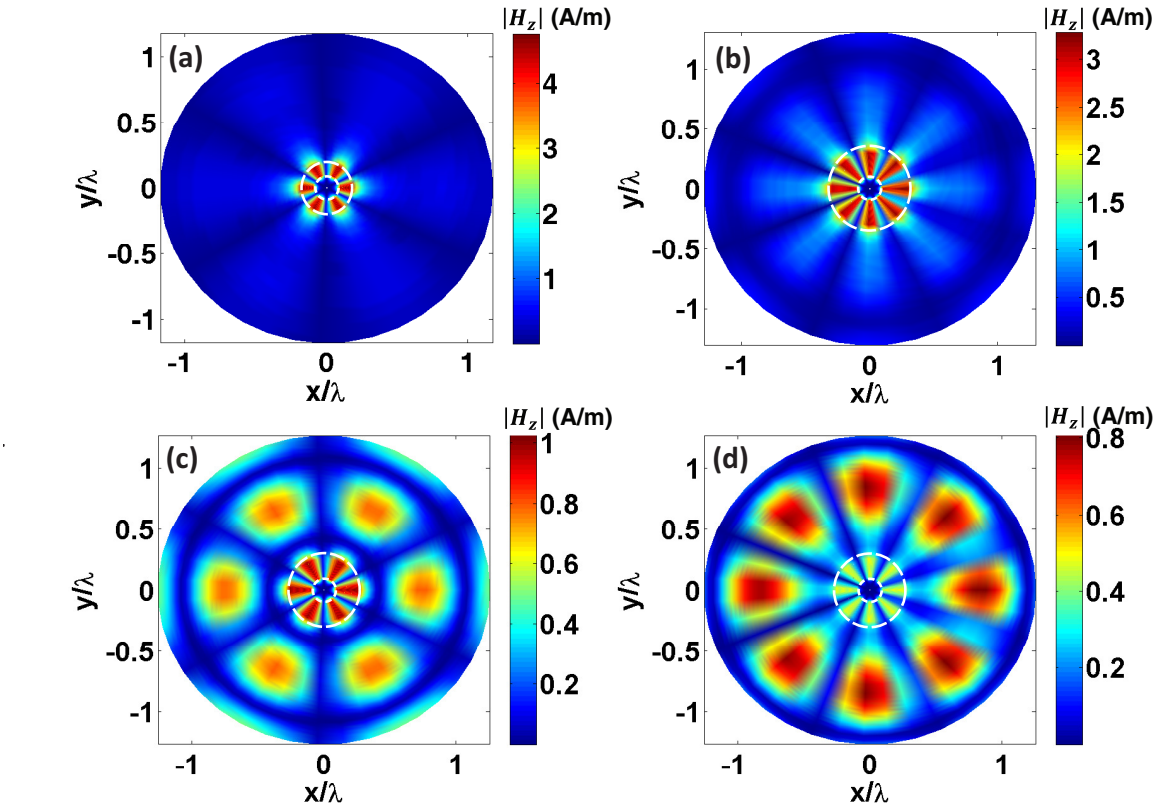

Figure 2.4: Field magnitude $|H_z|$ plotted versus x and y coordinates normalized by wavelength, of mode $|m|$ for the EMT-md case in Fig. 2.2(a). (a) $|m| = 3$, $k_0 b \approx 1.1$, (b) $|m| = 4$, $k_0 b \approx 1.9$, (c) $|m| = 3$, $k_0 b \approx 1.62$, and (d) $|m| = 4$, and $k_0 b \approx 1.62$. The dashed white circles represent the approximate inner and outer boundaries of the lens. (a) and (b) are at size parameters of resonances in Fig. 2.2(a) and we observe a dominant confined single mode with high field magnitude. However, (c) and (d) correspond to an off-resonant size parameter in which both modes are not confined and have lower field magnitudes than (a) and (b).

dition of $k_\parallel/k_0 \approx 4.6$ to around $k_\parallel/k_0 \approx 3$, decreasing the high parallel momentum for plasmonic resonance when the HMM is present. As m is a measure of the angular momentum, the above relationship $k_\parallel = m/r_{eff}$ indicates that the angular momentum for the mode is reduced, for a fixed effective radius r_{eff}, when $k_\parallel$ is decreased. We also plot $\log[\mathrm{Im}(R_p)]$ versus the converted effective m and size parameter $k_0 b$ in Fig. 2.5(b) and overlay the positions of the resonances of the cylindrical case in Fig. 2.2 onto Fig. 2.5(b). The resonant peaks in the cylindrical case closely follow the prediction of the planar case, allowing us to conclude that both resonances are of the same nature.

From this planar analysis, we can understand the relationship between the size parameter and mode number of the resonances in Fig. 2.2(b). After approximately 50 bi-layers, the parallel momentum required to excite the resonance becomes nearly constant as in Fig. 2.5(a). From the relation $k_{\|} = 2m/(a+b)$, if $k_{\|}$ is constant as b increases m must also increase, leading to the nearly linear increase of the mode number with size parameter as in Fig. 2.2(b).

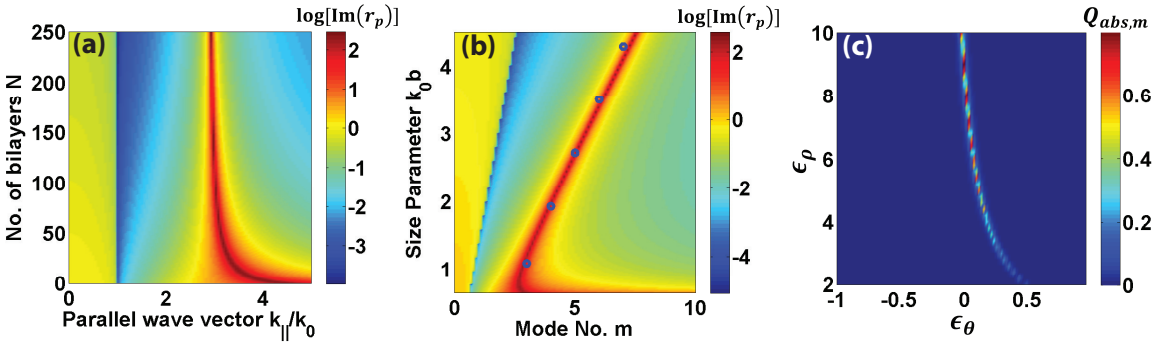

Figure 2.5: (a) Log plot of the imaginary part of the Fresnel reflection coefficient $\mathrm{Im}(R_p)$, indicating the magnitude of absorption of the incident evanescent field, using pTMM for different values of $k_{\|}/k_0$ and number of metal-dielectric bi-layers N. The HMM lowers the parallel momentum required for the resonance with slow variation versus number of bi-layers. (b) $\log[\mathrm{Im}(R_p)]$ for the planar case in (a) compared to the peak positions of the TMM-md case (symbols) in Fig. 2.2(b) for different equivalent values of m and size parameter $k_0 b$. The agreement between the planar and cylindrical calculations indicates that the composite plasmonic resonances are of the same nature. (c) Partial emissivity $Q_{abs,m}$ for $m = 4$ mode at a size parameter of $k_0 b \approx 1.8$ for EMT-HMM case in Fig. 2.2(a) for different values of ϵ_ρ and ϵ_θ. The region of interest for selective heating is $\epsilon_\rho > 5, \epsilon_\theta < 0$ for which the emissivity of the resonant mode is largest.

We now examine the optical properties of the HMM lens and core that will allow the selectivity by studying how the partial emissivity of a mode depends on the permittivity of the HMM lens. Figure 2.5(c) plots the partial emissivity for the $m = 4$ mode ($k_0 b \approx 1.8$ for EMT-HMM case in Fig. 2.2(a)) as ϵ_ρ and ϵ_θ varies. From Fig. 2.5(c), the largest enhancement occurs in the region of $\epsilon_\rho > 5$ and a negative but close to zero value of ϵ_θ. The enhancement for these permittivity values can be explained by the dispersion relation in the HMM [67], $k_\rho^2/|\epsilon_\theta| = k_\theta^2/\epsilon_\rho - k_0^2$, and noting that small and negative ϵ_θ, with $k_\theta/k_0 \approx 3$ and $\epsilon_\rho = 10$ for example, causes k_ρ to be

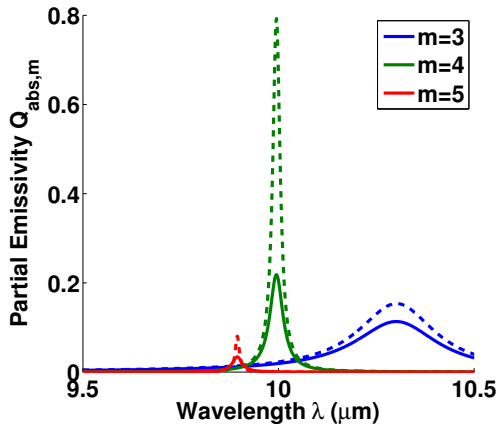

Figure 2.6: Partial emissivity $Q_{abs,m}$ versus wavelength for $m = 3, 4, 5$ with loss (solid lines) and without loss (dashed lines) in the HMM lens (where $a = 1$ μm and $k_0 b = 1.8$ for the mode $m = 4$ in Fig. 2.2). The presence of loss in the lens decreases the resonant absorption peak, $m = 4$, while the difference in emissivity between off-resonant modes such as $m = 3$ and the resonant $m = 4$ mode decreases. The colors indicating mode number m are the same for $Q_{abs,m}$ with and without loss.

very small and imaginary and allows the field to extend to the inner absorbing core. The sensitivity of the mode selective plasmonic resonances to the HMM parameters is unlike typical broadband enhancement effects of HMMs [19, 89].

2.3.4 Effects of lossy HMMs lens

Finally, we consider the effect of loss in the HMM lens. Physically, loss causes the lens to also play a role in radiative transfer. Since the temperature of the lens is not fixed, HMM lens will equilibrate to a temperature close to that of the heated core, allowing us to consider the core-lens structure as a single object for the purposes of analyzing radiative emission. We incorporate loss by modifying the Drude dispersion of the metal to have $\gamma = 0.001\omega_p$ so that $(\epsilon_m, \epsilon_d) = (-5.1+.015i, 3.4)$ at 10 μm, which is close to the lowest loss with negative real permittivity in the mid-infrared range of materials such as 4H-SiC [90]. The partial emissivity $Q_{abs,m}$ is now defined with respect to the size of the whole structure b. As shown in Fig. 2.6, adding loss decreases the peak absorptivity around 10 μm for $m = 4$ compared to the lossless case of Fig. 2.3(a). Also, with loss the $m = 4$ mode is no longer as dominant a resonance compared to

adjacent $m = 3$ and 5 modes in the wavelength range shown. We conclude that loss reduces the angular mode and wavelength selectivity for selective heating and thus that fully exploiting the thermal HMM lens requires low-loss plasmonic materials in the infrared. Recently, hexagonal Boron Nitride has been demonstrated as a low-loss material in the mid-infrared range with a hyperbolic dispersion [91, 92], potentially allowing the layered HMM lens to be replaced with a single material.

2.4 Conclusions

In summary, we theoretically demonstrated a new approach to selective radiative heating based on tuning angular mode resonances with HMM lenses. This approach enables selectivity for thermal radiative exchange due to the requirement that both wavelength and angular mode number of the emitter and absorber match. Our result could have applications in radiative thermal management. The following chapter proposes a new concept to manage near-field thermal radiation.

Chapter 3

Active Extraction of Near-field Thermal Radiation

Part of the contents of this chapter can also be found in Refs. [1, 93].

3.1 Introduction

The previous chapter highlights a metamaterial approach to engineer radiative heat transfer. While the ability to selectively transfer heat can be interesting and potentially useful, typically we are more concerned with how we can engineer thermal radiation for thermal management as in microelectronics [94], space technology [95] and buildings [96]. Typical techniques to control thermal radiation involve engineering the emissivity of the material and changing the surface area of emission or absorption. These techniques are passive which involves no energy input into the system and cannot cool objects below the temperature of the ambient environment the surface is interacting with. Another technique of thermal management is that of refrigerators which require work input but can maintain systems at desired temperature. Such techniques are active since energy input is needed but allows for cooling below ambient temperature without violating the laws of thermodynamics. Active thermal management techniques have only been utilized for thermal management through conduction and convection and not through thermal radiation.

In the far-field, the blackbody limit governs the maximum radiative flux between two bodies. Recently, a number of works have demonstrated that near-field radiative

heat transfer is enhanced by many orders of magnitude compared to the far-field limit for closely spaced objects with either natural [2, 29] or engineered resonant surface modes [19, 20, 30–32]. There have also been efforts to couple these near-field modes into the far-field with the use of grating structures [33], antennas [34], and a thermal extraction lens [35, 36].

While these passive schemes modify the heat flux flowing from a hot object to a cool object, active schemes extract energy from a system through external work and allow an object to be cooled below the ambient temperature. In optics, external work in the form of laser light has been used to cool gaseous matter to sub-millikelvin temperatures [97,98] by removing kinetic energy from the atoms. In solid-state materials, optical irradiation can also cool materials by emission of upconverted fluorescence [99] due to removal of energy in the form of phonons. This concept, known as laser cooling of solids (LCS), has been experimentally demonstrated to cool rare-earth doped glass [100,101] to cryogenic temperatures and recently to cool semiconductors by 40 K from the ambient temperature [102]. However, no active schemes have been proposed to extract energy out of a system as thermal radiation.

In Section 3.2, we took inspiration from LCS to theoretically propose and numerically demonstrate an active radiative cooling (ARC) scheme that extracts near-field thermal photons into the far-field. Our laser-based cooling approach exploits the monochromatic nature of near-field thermal radiation to drive a transition in a laser gain medium, which, when coupled with external optical pumping, allows the resonant surface mode to be emitted into the far-field. Our active scheme has an ideal efficiency that is orders of magnitude larger than that in traditional laser cooling of solids due to the relatively high energy of surface phonon polaritons compared to phonon energies. Furthermore, we show that the high energy density of monochromatic near-field thermal radiation is sufficient to pump transitions in gain media, a novel concept that could be used in other applications. Then, in Section 3.3, we apply the mathematical framework of LCS to create a generalized model of ARC [103, 104]. We show that LCS and ARC can be described with the same mathematical formalism by replacing the electron-phonon coupling parameter in LCS with the electron-photon

coupling parameter in ARC. We then compare LCS and ARC using realistic parameters and find that ARC can achieve higher efficiency and extracted power over a wide range of conditions.

3.2 A Simple System

A schematic of the method is given in Fig. 3.1(a). A laser gain medium containing emitters with discrete energy levels is placed in the near-field of a material that supports a resonant surface wave. We model the emitters as a three-level system, as shown in Fig. 3.1(b). An external pump laser is tuned to the 0-1 transition, exciting population into level 1. If the nearly-monochromatic thermal radiation drives the transition from 1-2 and the 2-0 transition is radiative with high quantum efficiency, the electron transition will emit blue-shifted photons in the far-field, thereby extracting the trapped near-field thermal radiation.

With a typical blackbody spectrum, the efficiency of such a scheme would be vanishingly small because of the low energy density and the broadband nature of thermal radiation [105]. However, in the near-field, it has been demonstrated that the radiative energy density is nearly monochromatic and far exceeds that in the far-field by several orders of magnitude [5]. Therefore, with near-field thermal radiation the 1-2 transition can be efficiently driven by matching the near-field energy resonance energy to the 1-2 transition energy.

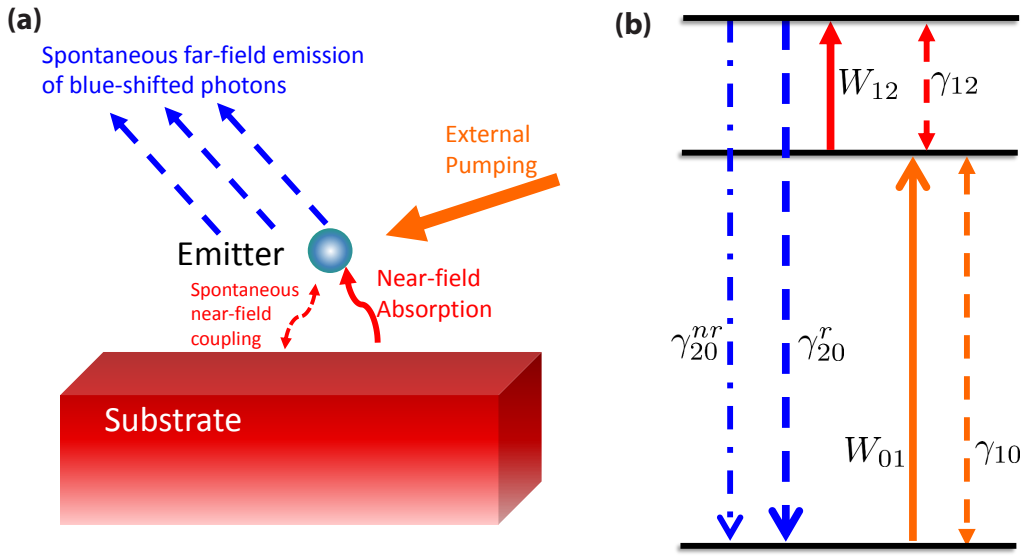

Figure 3.1: (a) Schematic of the active thermal extraction scheme. An emitter with discrete energy levels is placed in the near-field region of a semi-infinite planar substrate supporting a surface resonance. The external pumping couples with the near-field energy to be emitted as blue-shifted spontaneous emission in the far-field. (b) Energy level diagram of the emitter for our proposed concept. The 0-1 transition absorbs external pump photons, and near-field photons drive the 1-2 transition. Spontaneous emission from the 2-0 transition emits near-field photon to the far-field. The orange arrow indicates external optical pumping, the dashed arrows indicate various spontaneous decay channels with the blue arrows indicating the upconverted emitted photons carrying near-field energy into the far-field.

3.2.1 Theory

To study this system, we use rate equations to determine the steady-state populations in each energy level with external and near-field pumping:

$$\frac{dN_2}{dt} = -W_{12}(N_2 - N_1) - \gamma_{12}N_2 - \gamma_{20}N_2 \tag{3.1}$$

$$\frac{dN_1}{dt} = W_{12}(N_2 - N_1) - W_{01}(N_1 - N_0) - \gamma_{10}N_1 + \gamma_{12}N_2 \tag{3.2}$$

$$\frac{dN_0}{dt} = W_{01}(N_1 - N_0) + \gamma_{20}N_2 + \gamma_{10}N_1 \tag{3.3}$$

$$N_t = N_0 + N_1 + N_2 \tag{3.4}$$

where W_{12} is the absorption rate of the 1-2 transition as a result of the near-field energy density, W_{01} is the absorption rate of the 0-1 transition due to external pumping, N_i is population density of each level, N_t is the total population density for system, and γ_{ij} is the overall (radiative and non-radiative) spontaneous decay rate of the i-j transition. Here, γ_{ij}^r stands for radiative rate of the i-j transition such that $\gamma_{ij} = \gamma_{ij}^r + \gamma_{ij}^{nr}$. We assume that all energy levels are non-degenerate so that $W_{ij} = W_{ji}$. Solving Eqs. 3.1 to 3.4 in steady state yields the equilibrium population densities for each level from which the power density can be expressed as

$$\begin{aligned} P_{01} &= \hbar\omega_{10}W_{01}(N_0 - N_1) \\ &= \frac{\hbar\omega_{10}N_tW_{01}\left(W_{12}(\gamma_{10}+\gamma_{20}) + \gamma_{10}(\gamma_{12}+\gamma_{20})\right)}{W_{12}(\gamma_{10}+\gamma_{20}) + \gamma_{10}(\gamma_{20}+\gamma_{12}) + W_{01}\left(3W_{12} + 2(\gamma_{20}+\gamma_{12})\right)} \end{aligned} \tag{3.5}$$

$$\begin{aligned} P_{20,net} &= \hbar(\omega_{20} - \omega_{10})\gamma_{20}^r N_2 \\ &= \frac{\hbar(\omega_{20} - \omega_{10})N_tW_{01}\gamma_{20}^r W_{12}}{W_{12}(\gamma_{10}+\gamma_{20}) + \gamma_{10}(\gamma_{20}+\gamma_{12}) + W_{01}\left(3W_{12} + 2(\gamma_{20}+\gamma_{12})\right)} \end{aligned} \tag{3.6}$$

where P_{01} is the external power density absorbed by the 0-1 transition and $P_{20,net}$ is the net extracted power density into the far-field from the 2-0 transition.

Using Eqs. 3.5 and 3.6, the intrinsic efficiency of extraction can be expressed as the ratio of the amount of net extracted energy radiated into the far-field by the 2-0

transition with respect to the external pump energy absorbed by the 0-1 transition

$$\eta_{10} = \frac{P_{20,net}}{P_{01}} = \frac{(\omega_{20} - \omega_{10})\gamma_{20}^{r} W_{12}}{\omega_{10}(W_{12}(\gamma_{20} + \gamma_{10}) + \gamma_{10}(\gamma_{20} + \gamma_{12}))} \tag{3.7}$$

In the ideal limit of a dominant radiative 2-0 transition γ_{20} and strong near-field absorption W_{12}, Eq. 3.7 tends towards $(\omega_{20}/\omega_{10} - 1)(\gamma_{20}^{r}/\gamma_{20})$ which depends intuitively on the ratio of the emitted net energy and absorbed photon energy and on the radiative rate of the 2-0 transition for the photons that reach the far-field. When $\eta_{10} > 0$, there is net energy extracted from the system assuming no parasitic absorption of external pump energy. This assumption is reasonable as our pump wavelength is far from the resonance of the substrate such that the imaginary part of the permittivity is negligible. The intrinsic efficiency in Eq. 3.7 depends only on the internal parameters of the system and is independent of the absorption rate W_{01} of the external pumping (0-1) transition.

To estimate the efficiency of the scheme, we take properties based on rare-earth dopant embedded in gallium lanthanum sulfide (GLS) chalcogenide glass as the emitter system in the mid-infrared (MIR) region with typical values listed in Table 3.1 [106, 107]. We remove the magnetic dipole contribution to the 2-0 transition by reducing the overall quantum efficiency from 93% to 79%. Here, we choose the wavelength-independent permittivity of the GLS chalcogenide glass to be 4.8 [108].

Table 3.1: Parameters of a typical rare-earth emitter in GLS chalcogenide glass for modeling our proposed system. $\gamma_{ij}^{0}(\mathrm{s}^{-1})$ stands for the decay rate of the i-j transition for an isolated emitter and QE is the quantum efficiency of the transition.

Transition	$\lambda(\mu\mathrm{m})$	$\gamma_{ij}^{0}(\mathrm{s}^{-1})$	QE (%)
0-1	1.83	1034	100
2-0	1.22	1370	79
1-2	3.88	36	100

Then, we model the substrate permittivity with the expression $\epsilon(\omega) = \epsilon_{\infty}(\omega_L^2 - \omega^2 - i\gamma\omega)/(\omega_T^2 - \omega^2 - i\gamma\omega)$ where $\epsilon_{\infty} = 5.3$, $\omega_T = 388.4 \times 10^{12}$ s^{-1}, $\omega_L = 559.3 \times 10^{12}$ s^{-1} and $\gamma = 0.9 \times 10^{12}$ s^{-1}. We tailor the substrate resonance to match the 1-2 transition

with $\mathrm{Re}(\epsilon_{substrate}(\omega)) = -\epsilon_{medium}$ so as to enhance the energy density of the near-field thermal radiation with the emitter. Plasmonic resonances of the substrate in the MIR can be achieved with spoof plasmons in gold, for example [109].

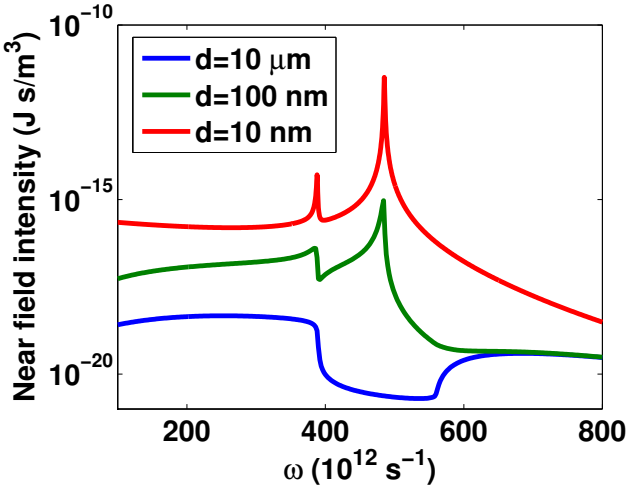

Figure 3.2: Energy density at different distances d from the surface of the substrate with the permittivity as described in the text. The top medium is GLS chalcogenide glass. The near-monochromatic nature of the near-field as distance is reduced is consistent with [5, 6].

To calculate the intrinsic extraction efficiency of this system using Eq. 3.7, we need to know near-field absorption rate W_{12}. We use the formulation from Ref. [6] to calculate the near-field energy density $I(\omega)$ of the substrate at 750 K shown in Fig. 3.2 where the blackbody spectrum peak matches the 1-2 transition wavelength in Table 3.1. Then, we approximate the near-field absorption rate W_{12} using the isotropic stimulated rate in Eq. (29) of Ref. [110]. We incorporate the energy per unit volume $I(\omega) = \int_0^\infty I(\omega, k)dk$ in Fig. 3.3(a) for the transition for different values of wave vector k to obtain

$$W_{ij,near-field} = \frac{\gamma_{ij}^0 \pi^2 c^3}{2\hbar\omega_0^3} \int_{-\infty}^{\infty}\int_0^\infty (1 + |\frac{k}{\sqrt{\epsilon_{medium} - k^2}}|^2) I(|\omega|, k) g(\omega) dk d\omega \tag{3.8}$$

$$g(\omega) = \frac{\frac{\Delta\omega}{2\pi}}{(\omega - \omega_0)^2 + (\Delta\omega/2)^2} \tag{3.9}$$

where γ_{ij}^0 is the spontaneous decay rate for an isolated emitter and $g(\omega)$ is the line-shape of the transition with a linewidth of $\Delta\omega$. The derivation of Eq. 3.8 is given in

Appendix A. The distance dependence of γ_{ij} of an isotropic emitter due to the modification of density of states by the surface in the near-field follows the formulation in Chance et al. [111].

The induced absorption rate W_{01} due to far-field pumping is calculated using the well-known expression for the stimulated rate [112] $W_{ij,external} = \lambda^2 g(\omega) I_v \gamma_{ij}^r / (8\pi n^2 \hbar\omega)$ where γ_{ij}^r is the radiative spontaneous decay rate that couples to external pumping from the far-field, I_v is the incident intensity of the external pumping field, and n is the index of the chalcogenide medium. The linewidth for the 0-1 and 2-1 transitions are assumed to be $2 \times 10^{11}\,\mathrm{s}^{-1}$, comparable to those of typical laser gain media [112].

3.2.2 Results

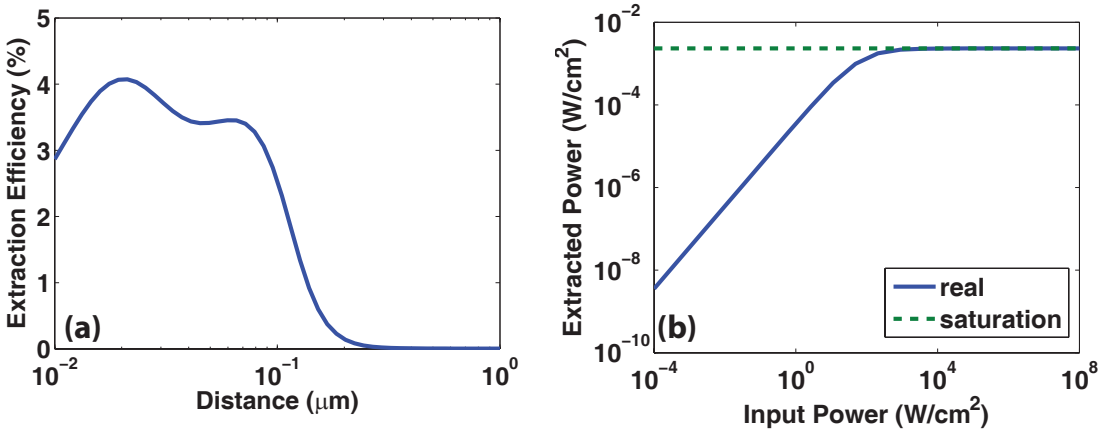

Figure 3.3: (a) Extraction efficiency η_{10} of external pumping from the 0-1 transition assuming properties in Table 3.1. The low efficiency in the blue line is a result of the large spontaneous rate for 1-2 transition in the near-field in Fig. 3.4(a). (b) Integrated power extracted for emitters uniformly distributed from surface. The density of emitters is assumed to be $10^{20}\,\mathrm{cm}^{-3}$. The saturation behavior approaches the green dashed "saturation" line due to the finite number of emitters in the system saturating the population difference at high input powers.

The intrinsic efficiency of thermal extraction versus distance from the emitter is shown in Fig. 3.3(a). The maximum efficiency is small, around 4% and decreases to zero beyond a few hundred nanometers. The total extracted intensity is defined as the integral of the power emitted by the 2-0 transition over all distances, $\int_{z_1}^{z_2} P_{20,net} dz$.

We integrate from $z_1 = 10$ nm onward until the intrinsic efficiency decreases to almost zero. Figure 3.3(b) shows the extracted power per unit area as a function of input power I_v. The extracted power increases linearly with the input power for low power inputs before saturating at higher powers, but the overall power extracted is orders of magnitude lower than the input power. A limiting case of Eq. 3.6 can be found for large W_{01} as $\hbar(\omega_{20} - \omega_{10})W_{12}\gamma_{20}^r N_t/(3W_{12} + 2(\gamma_{20} + \gamma_{12}))$. Integrating this limit over distance agrees with the saturation curve as plotted in Fig. 3.3(b).

Figure 3.3 shows that active thermal extraction is possible, but both the intrinsic efficiency and the total power extracted are very small for the chosen parameters. However, according to the limit of Eq. 3.7, the maximum efficiency should be around 35%, much higher than in the example. To understand the reason for this difference, we examine Eq. 3.7 in more detail. The maximum efficiency occurs when γ_{20} and W_{12} are large. We calculate the transition rates versus distance from the substrate in Fig. 3.4(a), and observe that the transition rates for 0-1 and 2-0 transitions are not affected by the presence of a surface, as they are off-resonant. However, the decay rate for the 1-2 transition γ_{12} is strongly enhanced as the emitter approaches the surface [111, 113, 114]. As a result, the near-field absorption rate is smaller by about two orders of magnitude compared to the decay rate even though both are enhanced by orders of magnitude due to the increase in the optical density of states in the near-field. Physically, this calculation indicates that as electrons are excited from energy level 1 to 2, they immediately decay back to level 1 at the rate γ_{12}.

The reason for this cycling is that the thermal near-field energy density is not sufficient to allow near-field absorption to dominate over near-field spontaneous decay. Archambault et al. [110] also highlight the need for some minimum energy density for stimulated emission to dominate spontaneous decay. Unlike the case for stimulated emission of surface plasmons with external pumping such as in Ref. [115–117] where the external laser field intensities can be tuned, here the thermal energy density is restricted to that for a blackbody. Thus, the spontaneous decay rate will always dominate over near-field absorption for realistic values of near-field energy density. On the other hand, Fig. 3.3(a) also shows that while a resonantly enhanced γ_{12} offsets

the enhanced absorption W_{12}, the extraction efficiency η_{10} still requires a large value of W_{12}. Beyond a emitter-substrate distance of about 100 nm, the extraction efficiency in Fig. 3.3(a) drops significantly as a result of the low near-field energy density, although the ratio W_{12}/γ_{12} remains of the same order of magnitude up to 1 μm.

Therefore, to break the cycling between levels 1 and 2, it is essential that the strongly radiative decay rate from 2-0 (γ_{20}) is comparable to the decay rate γ_{12} in the near-field. Figure 3.4(b) shows that the efficiency is boosted to almost the ideal limit at short distances if γ_{20} is increased substantially. In Eq. 3.7, if we increase γ_{20} to be more comparable to γ_{12} in the near-field, then the ratio of $\gamma_{20}^r/\gamma_{20}$ begins to dominate in the expression, increasing the extraction efficiency towards the ideal limit discussed earlier.

The factors discussed above affect the intrinsic efficiency, but the total extracted power also depends on the input power W_{01} and the emitter density N_t. Firstly, the absorption of the pump power W_{01} depends on the linewidth of the 0-1 transition, and decreasing the linewidth increases W_{01} in Eq. 3.6 due to the increased concentration of input power in a given bandwidth for each emitter. The pump absorption could also be increased by photon recycling as in traditional laser cooling of solids, but we do not account for this possibility here. Secondly, the total dopant density N_t also affects the extracted power. As discussed earlier, the saturation limit at higher incident powers is proportional to the dopant density, and therefore the dopant density must increase to increase the saturation limit.

Using this understanding, we now recalculate the efficiency and extracted power for an optimized gain medium with the spontaneous rate for the 2-0 transition increased to $1.37 \times 10^7\,\mathrm{s}^{-1}$, $\Delta\omega_{10} = 2 \times 10^9\,\mathrm{s}^{-1}$ and $N_t = 10^{21}\,\mathrm{cm}^{-3}$. Figure 3.4(c) shows that the intrinsic extraction efficiency is much higher than in Fig. 3.3(a) and almost near the ideal limit for small emitter-substrate distances. The decrease of efficiency at larger emitter-substrate distances is due to a decrease in near-field coupling. Figure 3.4(d) shows a much-increased integrated extracted power at each given input power compared to Fig. 3.3(b). The saturation limit derived earlier also agrees with the full calculation at higher input powers.

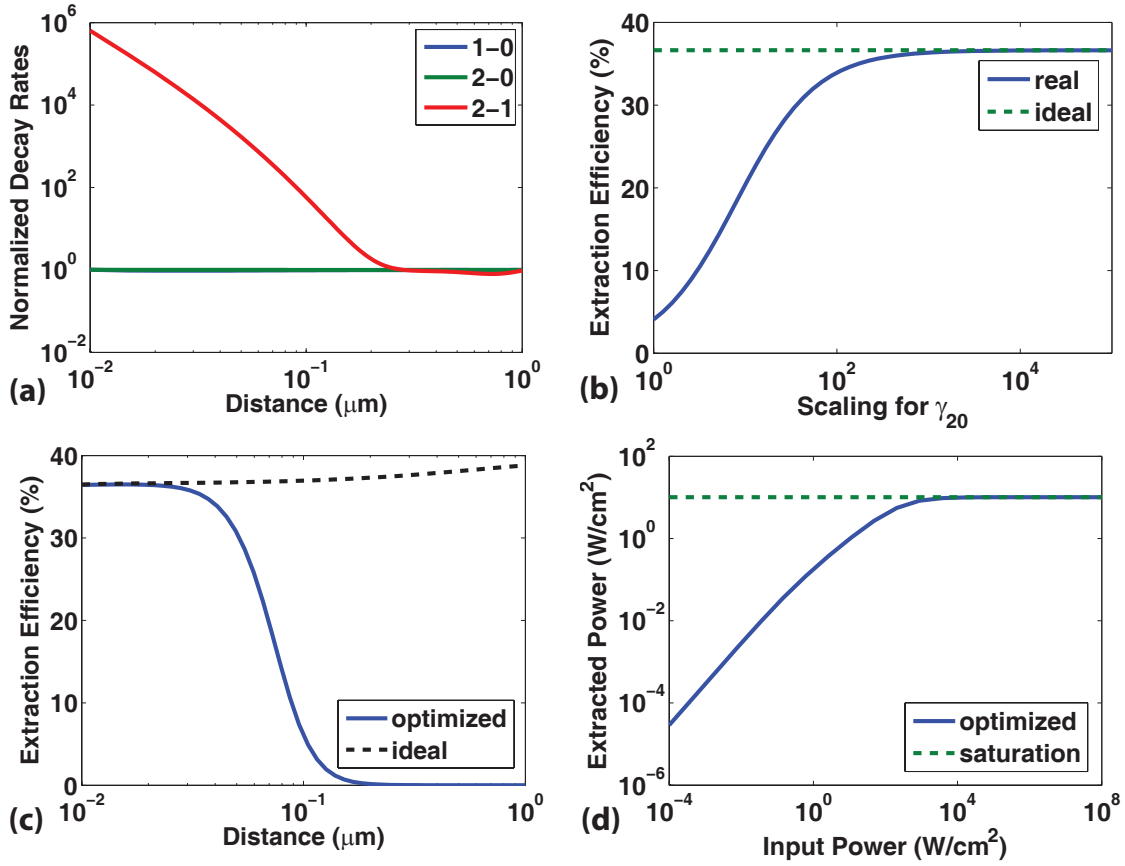

Figure 3.4: (a) Normalized spontaneous decay rates versus distance for three different transitions. The 2-1 transition is on resonance with the substrate dispersion and is enhanced greatly whereas the 0-1 and 2-0 transitions are not significantly affected by the presence of the substrate. (b) Intrinsic extraction efficiency η_{10} versus the scaling of the spontaneous rate γ_{20} at $d = 20$ nm. The blue line shows real behavior according to Eq. 3.7. Increasing γ_{20} greatly enhances the efficiency so that it approaches the ideal limit of the system. (c) Intrinsic extraction efficiency versus emitter-substrate distance for an optimized system. The extraction efficiency follows the ideal limit for small distances before decreasing due to a decreasing W_{12} and is much improved compared to Fig. 3.3(a). (d) Integrated power extracted of the optimized system with emitters uniformly distributed from the substrate surface. An increased pump absorption and a higher emitter density lead to a much higher saturation limit, shown as the dashed line.

This calculation shows that the active thermal extraction scheme has potential to efficiently extract a significant amount of near-field thermal radiative energy. The key to realizing this potential is to identify an appropriate emitter with a surface resonance and a gain medium with matching transitions in the mid-infrared wavelength range where photons are thermally populated at typical temperatures. Additionally, recycling the pump photons to increase absorption, as is done in traditional laser cooling of solids, is important to decrease the required pump power. A high dopant density is still required to increase the saturation limit. Cerium doped crystals can potentially be a candidate as they have a $4f^0 5d^1 \rightarrow 4f^1 5d^0$ transition with a short lifetime of around 40 ns [118], ideal for the 2-0 transition proposed here, as well as a mid-infrared transition of 4.5 μm [118] for the near-field absorption.

3.3 A Generalized Description on Radiative Near-field Active Thermal Extraction and Temperature Sensing

In Section 3.2, we theoretically proposed an active radiative cooling (ARC) scheme that extracts near-field thermal photons into the far-field and is capable of cooling an object below ambient temperature. An examination of ATX reveals a close analogy with laser cooling of solids, in which absorption of thermal phonons from the host crystal results in emission of upconverted photons. This process has been experimentally demonstrated to cool rare-earth doped glasses [100, 101, 119–121] to cryogenic temperatures and recently to cool semiconductors [102] and lead perovskites [122]. At the same time, LCS has been used as a means to measure temperature by observing the wavelengths of emitted light, with applications for temperature sensing at the nanoscale and in biological tissues [123–130].

In this work, we apply the mathematical framework of LCS [103, 104] to create a generalized model of ATX. We show that LCS and ATX can be described with the same mathematical formalism by replacing the electron-phonon coupling parameter

in LCS with the electron-photon coupling parameter in ATX. We then examine how ATX may be used for applications such as radiative cooling and temperature sensing.

This paper is organized as follows. We first summarize the derivation of the model for LCS in Section 3.4. Then, we derive an analogous generalized model for our ATX scheme and its associated quantities in Section 3.4. In Section 3.4, we explain the mathematical equivalence between electron-phonon coupling model in LCS and electron-photon coupling model in ATX. We next examine the potential of ATX for near-field extraction in terms of efficiency and net power in Section 3.5 and discuss how parasitics can affect the performance of ATX in Section 3.7. In Section 3.6, we consider how ATX may be used for non-contact temperature sensing. Finally, we end with a summary of the results in Section 3.8.

3.4 Theory

Generalized theory for laser cooling of solids

We first briefly describe a generalized model of upconversion in laser cooling of solids as given in Refs. [100,101,103,104,119,120,131] to facilitate the derivation in the next section. The basic principle of LCS is illustrated in Fig. 3.5(a). The gain medium consists of emitters embedded in a host lattice at finite temperature. The energy of the lattice due to its finite temperature will manifest itself as phonons or vibrations of the lattice atoms. These vibrations will couple to the emitters through perturbations of the valence electrons, exchanging energy with the emitters. The net result of this interaction is thermal equilibrium of the electron with phonons in the host. When an incident pump is introduced into the gain medium, the valence electron is excited to a higher energy level. It may in turn absorb a phonon and then emit upconverted light, thereby extracting thermal energy from the system.

Figure 3.5(b) shows the four-level system of Fig. 3.5(a) for LCS for applications of cooling in Refs. [103,104]. The ground state manifold consists of two closely spaced levels of $|0\rangle$ and $|1\rangle$ separated by energy δE_g, and the excited manifold consists of

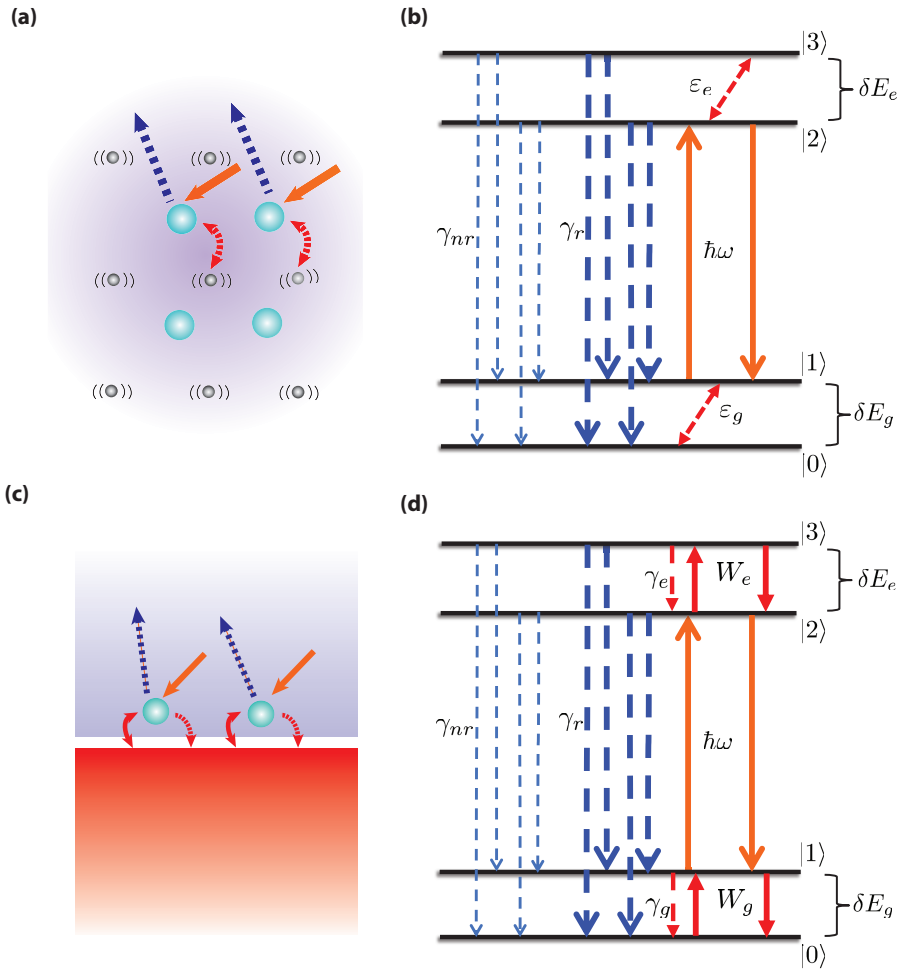

Figure 3.5: (a) Schematic of the concept in laser cooling of solids (LCS). The gain medium consists of rare earth emitters embedded in a host material at a finite temperature. The external pump photons excite the rare-earth emitter, and by absorption of a phonon, carry the energy away as upconverted fluorescence. (b) Energy diagram of the four-level system for LCS. A incident pump laser excitation with energy $\hbar\omega$ is shown by the solid orange arrow. The thick dark blue dashed arrows indicate spontaneous emission transitions with a rate of γ_r and the thin blue dashed arrows indicates the nonradiative decay rates (γ_{nr}). $\varepsilon_{e,g}$ is the electron-phonon coupling rate with the subscript "g" for the ground state manifold $|0\rangle$ and $|1\rangle$ and "g" for the excited state manifold $|2\rangle$ and $|3\rangle$, respectively. (c) Schematic showing the concept of active thermal extraction (ATX). A rare-earth doped gain medium is placed in the near-field of a substrate. The external pump photons excite the rare-earth emitter and result in blue-shifted fluorescence due to coupling to the near-field thermal radiation from the substrate, leading to extraction of thermal energy. (d) Energy diagram of the four-level system for ATX. $\gamma_{e,g}$ is the overall decay rate and $W_{e,g}$ is the absorption and stimulated emission rate for each of the manifold. The subscripts "e" and "g" refer to the same manifolds as (b).

$|2\rangle$ and $|3\rangle$ with an energy separation δE_e. The subscript "e" and "g" indicates the excited or ground state manifold, respectively. A incident pump laser excitation with energy $\hbar\omega$ is on resonance with the $|1\rangle$-$|2\rangle$ transition. The spontaneous emission transitions are labeled as γ_r and likewise the non-radiative decay rates are labeled γ_{nr}. The electron-phonon interaction rate given are by ε_g and ε_e. We assume unity degeneracy for all levels and let the overall decay rate $R = 2(\gamma_r + \gamma_{nr})$. The rate equations for the density populations N_0, N_1, N_2, and N_3 are:

$$\frac{dN_1}{dt} = -\sigma_{12}(N_1 - N_2)\frac{I}{\hbar\omega} + \frac{R}{2}(N_2 + N_3) - \varepsilon_g(N_1 - N_0\exp(-\delta E_g/kT)) \tag{3.10}$$

$$\frac{dN_2}{dt} = \sigma_{12}(N_1 - N_2)\frac{I}{\hbar\omega} - RN_2 + \varepsilon_e(N_3 - N_2\exp(-\delta E_e/kT)) \tag{3.11}$$

$$\frac{dN_3}{dt} = -RN_3 - \varepsilon_e(N_3 - N_2\exp(-\delta E_e/kT)) \tag{3.12}$$

$$N_t = N_0 + N_1 + N_2 + N_3 \tag{3.13}$$

where σ_{12} is the absorption cross section of the $|1\rangle$-$|2\rangle$ transition, I is the incident laser intensity, k is the Boltzmann constant and T is the lattice temperature. Evaluating the steady-state solution to Eqs. 3.10-3.13, we define the net power density as the difference between absorbed and radiated contributions as

$$P_{net} = \sigma_{12}(N_1 - N_2)I - \gamma_r(N_2(E_{21} + E_{20}) + N_3(E_{31} + E_{30})) \tag{3.14}$$

We have ignored a term that represents parasitic absorption of the pump laser in Refs. [103, 104] for the purpose of illustrating the concept of LCS. The net power density remaining in the system can then be expressed as

$$P_{net,LCS} = \alpha_{LCS}I(1 - \eta_q\frac{\hbar\omega_{f,LCS}}{\hbar\omega}) \tag{3.15}$$

where $\eta_q = \frac{\gamma_r}{\gamma_r+\gamma_{nr}}$ is the internal quantum efficiency of the transition and $\hbar\omega_f$ denotes the mean fluorescence energy of the four-level system given by

$$\hbar\omega_{f,LCS} = \hbar\omega + \frac{\delta E_g}{2} + \frac{\delta E_e}{1 + (1 + R/\varepsilon_e)\exp(\delta E_e/kT)} \tag{3.16}$$

with the ground state resonant absorption α_{LCS} given by

$$\alpha_{LCS} = \sigma_{12} N_t \left(1 + \exp(\frac{\delta E_g}{kT})\right)^{-1} \tag{3.17}$$

In deriving Eq. 3.15, we ignore saturation as in Refs. [103, 104].

The cooling efficiency is defined by $\eta_{LCS} = -P_{net,LCS}/P_{abs,LCS}$ and from Eq. 3.15

$$\eta_{LCS} = \eta_q \frac{\hbar\omega_{f,LCS}}{\hbar\omega} - 1 \tag{3.18}$$

Other than cooling, the upconverted fluorescence that occurs in LCS has also been exploited for temperature sensing [123–130]. In this case, the gain medium is in thermal equilibrium with the medium of interest. Again solving Eqs. 3.10-3.13, we can obtain the upconverted output power as

$$P_{upconvert,LCS} = \eta_q \alpha I(\frac{h\nu_{u,LCS}}{h\nu}) \tag{3.19}$$

where the up-converted mean photo-luminescence energy $h\nu_u$ is now defined as

$$h\nu_{u,LCS} = \frac{h\nu}{2}(1+\frac{1}{1 + e^{\delta E_e/k_B T}(1 + \frac{R}{w_2})})+\frac{\delta E_l}{2}+\frac{\delta E_u}{1 + (1 + 2(W_{rad} + W_{nr})/w_2)\exp(\delta E_u/kT)} \tag{3.20}$$

unlike Eq. 3.16. For temperature sensing, the sensitivity of the emitted fluorescence to variations in temperature $dP_{upconvert,LCS}/dT$ is the key parameter rather than the net extracted power. Taking ratios of the upconverted intensity with a reference is the widely used method today [123–130] but for simplicity we will focus on the absolute upconverted power for the generalized model here.

Generalized theory for active thermal extraction

Active thermal extraction (ATX) in Fig. 3.5(c) employs a laser gain medium containing emitters with discrete energy levels placed in the near-field of a material that supports a resonant surface wave. We assume no physical contact between the gain medium and the substrate so that thermal radiation is the only form of heat transfer between them. Similar to LCS, the emitters here exchange energy and thus are in quasi-thermal equilibrium with the thermal near-field. With external pumping, the near-field energy absorbed by the emitter can combine with the pump to be remitted as blue-shifted light into the far-field [93].

We model the emitters in our ATX scheme as a four-level system, as shown in Fig. 3.5(d). An external pump laser is tuned to the $|1\rangle$-$|2\rangle$ transition. The near-field thermal radiation drives the transition from $|0\rangle$-$|1\rangle$ and $|2\rangle$-$|3\rangle$. Two of the four spontaneous emission channels in Fig. 3.5(d), namely $|3\rangle$-$|0\rangle$ and $|2\rangle$-$|0\rangle$, will emit blue-shifted photons in the far-field thereby extracting thermal energy out of the system.

The generalized system of equations for the scheme in Fig. 3.5(d) can be written as

$$\frac{dN_1}{dt} = -\sigma_{12}(N_1 - N_2)\frac{I}{\hbar\omega} + \frac{R}{2}(N_2 + N_3) - W_g(N_1 - N_0) - \gamma_g N_1 \tag{3.21}$$

$$\frac{dN_2}{dt} = \sigma_{12}(N_1 - N_2)\frac{I}{\hbar\omega} - RN_2 + W_e(N_3 - N_2) + \gamma_e N_3 \tag{3.22}$$

$$\frac{dN_3}{dt} = -RN_3 - W_e(N_3 - N_2) - \gamma_e N_3 \tag{3.23}$$

$$N_t = N_0 + N_1 + N_2 + N_3 \tag{3.24}$$

where quantities are defined in the same way as Eqs. 3.10-3.13. The ground state manifold ($|0\rangle$ and $|1\rangle$) and the excited state manifold ($|2\rangle$ and $|3\rangle$) in Eqs. 3.21-3.24 are coupled to near-field thermal radiation. Spontaneous emission rates γ_g and γ_e are associated with the ground and excited state manifold, respectively. Absorption and stimulated emission associated with each manifold are defined as W_g and W_e, re-

spectively. Absorption and stimulated emission for each manifold are equal assuming unity degeneracy: $W_{01} = W_{10} = W_g$ and $W_{23} = W_{32} = W_e$.

Solving Eqs. 3.21-3.24 in steady state and using the same definition of net power as Eq. 3.14, one can express the net extracted power for ATX in the same form as Eq. 3.15.

$$P_{net,ATX} = \alpha_{ATX} I(1 - \eta_q \frac{\hbar\omega_{f,ATX}}{\hbar\omega}) \tag{3.25}$$

$$\alpha_{ATX} = \sigma_{12} N_t \frac{W_g}{2W_g + \gamma_g} \tag{3.26}$$

where α_{ATX} is the ground state absorption for the ATX model. The mean fluorescence energy $\hbar\omega_{f,ATX}$ for ATX is given by

$$\hbar\omega_{f,ATX} = \hbar\omega + \frac{\delta E_g}{2} + \frac{\delta E_e}{2 + (R + \gamma_e)/W_e} \tag{3.27}$$

Likewise, the efficiency can be defined in the same way as Eq. 3.18:

$$\eta_{ATX} = \eta_q \frac{\hbar\omega_{f,ATX}}{\hbar\omega} - 1 \tag{3.28}$$

with the mean fluorescence energy defined in Eq. 3.27 above.

In addition, we can quantify the potential for ATX for temperature sensing applications through the upconverted output power like Eq. 3.19 in LCS as follows:

$$P_{upconvert,ATX} = \eta_q \alpha I(\frac{h\nu_{u,ATX}}{h\nu}) \tag{3.29}$$

where the corresponding up-converted mean photo-luminescence $h\nu_{u,ATX}$ is

$$h\nu_{u,ATX} = \frac{h\nu}{2}(1 + \frac{1}{2 + (R + \gamma_e)/W_e}) + \frac{\delta E_g}{2} + \frac{\delta E_e}{2 + (R + \gamma_e)/W_e} \tag{3.30}$$

The ability for ATX to sense temperature changes is denoted by its sensitivity to temperature change $dP_{upconvert,ATX}/dT$ which will be discussed in the subsequent

sections.

Comparision of ATX and LCS

With the theory for a generalized LCS system and a generalized ATX system established in Sections 3.4 and 3.4, we now explore the relationship between the two schemes. Intuitively, a close correspondence should exist between LCS and ATX because the fluorescence up-conversion process in the two schemes is identical. The key difference between the two schemes is the energy of the extracted particle and the nature of the coupling between the electrons and the emitters. In LCS, phonons with relatively small energies on the order of meV ($\sim$10 meV) are extracted and the quasi-thermal equilibrium electron-phonon coupling constants between states $|0\rangle$-$|1\rangle$ in the ground state and $|2\rangle$-$|3\rangle$ in the excited state manifold are the relevant parameters. In ATX, the extracted particles are surface phonon-polaritons with energies on the order of hundreds of meV, and the coupling constants are the radiative spontaneous and stimulated decay rates of the energy levels of the emitters due to the emission of photons.

We now examine the comparison in more details. If we neglect the excited state manifold and just focus on the ground state manifold $|0\rangle$ and $|1\rangle$ in Fig. 3.5(b), we can write a rate equation for the two-level case for LCS as:

$$\frac{dN_1}{dt} = -\varepsilon_g(N_1 - N_0 \exp(-\delta E_g/kT)) \tag{3.31}$$

Similarly, isolating the ground state manifold in the ATX case in Fig. 3.5(d), we have a two-level system $|0\rangle$ and $|1\rangle$ coupled to thermal radiation with the rate equation for state $|1\rangle$ as:

$$\frac{dN_1}{dt} = N_0 W_g - N_1(W_g + \gamma_{10}) \tag{3.32}$$

Examining Eqs. 3.31 and Eq. 3.32, we find that they can be made identical with the following substitutions:

$$\varepsilon_g = W_g + \gamma_g \tag{3.33}$$

$$\frac{\varepsilon_g}{W_g} = \exp(\frac{\delta E_g}{kT}) \tag{3.34}$$

Therefore, the electron-phonon coupling rate ε_g in LCS takes the role of the spontaneous and stimulated rates γ_g and W_g for electron-photon coupling with thermal radiation in ATX.

Examining Eqs. 3.33 and 3.34, we can relate spontaneous and stimulated rates γ_g and W_g using the Boltzmann factor as:

$$\frac{\gamma_g}{W_g} = \exp(\frac{\delta E_g}{kT}) - 1 \tag{3.35}$$

On the other hand, if for ATX we assume that the ground state is in quasi-thermal equilibrium with the thermal radiation such that

$$\frac{N_1}{N_0} = \exp(\frac{-\hbar\omega_g}{kT}) = \exp(\frac{-\delta E_g}{kT}) \tag{3.36}$$

we can also obtain Eq. 3.35 from substituting Eq. 3.36 into Eq. 3.32. Thus, quasi-thermal equilibrium is automatically guaranteed in the mathematical equivalence in Eqs. 3.33 and 3.34. Also, Eq. 3.35 is identical to the classical result for a two-level system interacting with thermal radiation [132]. In Einstein's work [132], only the far-field form of thermal radiation described by Planck's law was considered, but the formulation depends only on the photonic density of states and thus is applicable in the near-field as well. Here in ATX, radiative thermal equilibrium is assumed between thermal radiation of the substrate and the emitters of the gain medium.

Although there are many similarities between LCS and ATX, there is one important difference. In LCS, the relevant temperature for the extracted thermal phonons is that of the gain medium itself. In ATX, the relevant temperature is that of thermal radiation emitted from substrate, which may be very different from that of gain medium if, for instance, the medium is maintained at a given temperature by a

separate thermal reservoir. This difference in temperature can have important implications, particularly for the strength of non-radiative processes that depend on the temperature of the gain medium.

3.5 Results

Ideal efficiency and extracted power

We now compare the ideal efficiency and net extraction power that can be achieved with LCS and ATX using the mathematical formalism derived in the previous section, neglecting the influence of parasitic processes. These processes will examined in Section 3.7. To perform this comparison, we need to choose realistic parameters for the gain media for both LCS and ATX. Due to the considerable differences in requirements of the gain media for LCS and ATX, it is not possible to directly compare LCS and ATX based on the same gain medium. For instance, the host material for the gain medium for LCS does not have to be transparent in the mid infrared (MIR) but for the host material of the gain medium in ATX, it is desirable for the host material to be transparent in the MIR. This ensures that the near-field thermal radiation can interact directly with the emitters rather than be absorbed by the host material.

First, we estimate the energy δE_g and δE_e for the ground and excited state manifolds assuming that they are approximately equal. For LCS, typical phonon energy of rare earth materials such as doped fluorozirconate glass (ZBLAN:Yb^{3+}) [119] is around a few percent of the pump photon energy. Here, we assume a typical value of $\delta E_g \approx \delta E_e \sim 0.01\hbar\omega$ for LCS.

For ATX, typical thermal photon energy is higher than phonon energy and ideally has a value that is close to the energy corresponding to the energy corresponding to the peak of the blackbody spectrum [93] so as to maximize its near-field energy density. If we consider the temperature of the substrate to be 300 K and choose a rare-earth emitter with transitions that matches the peak of the blackbody spectrum peaks around 10 μm, the corresponding manifold energy separation $\delta E_g \approx \delta E_e \approx 0.1\hbar\omega$

assuming a pump wavelength of 1 μm. Thus, we observe that the energy gaps in ATX are at least a few times larger than energy gap of those in LCS due to the larger energy of surface phonon polaritons compared to those of phonons.

To estimate the decay rates for LCS and ATX, we have to examine each coupling mechanism. Having established mathematical equivalence of LCS and ATX, Eq. 3.16 only requires us to estimate the values of the spontaneous decay rate R and the decay rate ε for external coupling within the manifold (assuming $\varepsilon_g = \varepsilon_e = \varepsilon$). For LCS, this coupling is provided by electron-phonon interaction. Here, ε follows the energy gap law [133] given by

$$\varepsilon = b \exp(\frac{-a\delta E}{\hbar\omega_{max}}) \tag{3.37}$$

where a and b are constants and $\hbar\omega_{max}$ is the maximum phonon energy of the host material. Typical values of a and b are on the order of 3.5 and 10^{12} [134], $\omega_{max} \approx \omega/10$ [135] and $\delta E \approx 0.01\hbar\omega$. Using these parameters, we estimate the electron-phonon coupling to be $\varepsilon \approx 7 \times 10^{11}$ s^{-1} which is within the range of values for known host materials [134]. Considering typical γ_r to be on the order of 100 s^{-1} [135] and assuming a unity quantum efficiency, the overall decay rate $R = 2\gamma_r = 200$ s^{-1} which is much smaller than ε. Thus, the mean fluorescence efficiency in Eq. 3.16 can be approximated as:

$$\hbar\omega_f \approx \hbar\omega + \frac{\delta E_g}{2} + \frac{\delta E_e}{1 + \exp(\delta E_e/kT)} \tag{3.38}$$

For ATX, the coupling rate ε within each manifold is the sum of the spontaneous and stimulated rates (γ and W) according to Eq. 3.33. Like Ref. [93], we assume the surface resonance of the substrate in Fig. 3.5(c) matches the energy separation $\delta E_g \approx \delta E_e$ of each manifold. As a result, the enhanced density of states in the near-field will both increase γ and W by orders of magnitude [93]. Using Eq. 3.33, the coupling ε within each manifold for our scheme will also be orders of magnitude larger compared to the overall decay rate R if we again assume R to be around 200 s^{-1}. Thus, we can define the mean fluorescence frequency in the same way as was done for LCS in Eq. 3.38 as:

$$\eta_{LCS,ATX} \approx \frac{\delta E_{LCS,ATX}}{\hbar\omega}\left(\frac{1}{2}+\frac{1}{1+\exp(\frac{\delta E_{LCS,ATX}}{kT})}\right) \tag{3.39}$$

and likewise express net extracted power normalized with respect to incident absorbed power as

$$\left|\frac{P_{net,(LCS,ATX)}}{I\sigma_{12}N_t}\right| \approx \frac{\delta E_{LCS,ATX}}{\hbar\omega\left(1+\exp(\frac{\delta E_{LCS,ATX}}{kT})\right)}\left(\frac{1}{2}+\frac{1}{1+\exp(\frac{\delta E_{LCS,ATX}}{kT})}\right) \tag{3.40}$$

assuming the quantum efficiency $\eta_q = 1$.

Figure 3.6(a) shows the comparison of the ideal efficiency, without consideration of parasitics, versus temperature for ATX and LCS using Eq. 3.39 with pump energy $\hbar\omega = 1.24$ eV for both schemes. The overall higher ideal efficiency for ATX is due to higher energy of the extracted phonon polariton compared to that of typical phonons. In the limit of large temperature, the ideal efficiency for both LCS and ATX tends to $\delta E/(\hbar\omega)$ according to Eq. 3.39 which is 10% for ATX and 1% for LCS as shown in Fig. 3.6(a). In the limit of low temperatures, the ideal efficiency tends to $\delta E/(2\hbar\omega)$ according to Eq. 3.39. This limit is also obeyed as shown in Fig. 3.6(a) which is 5% for ATX and 0.5% for LCS.

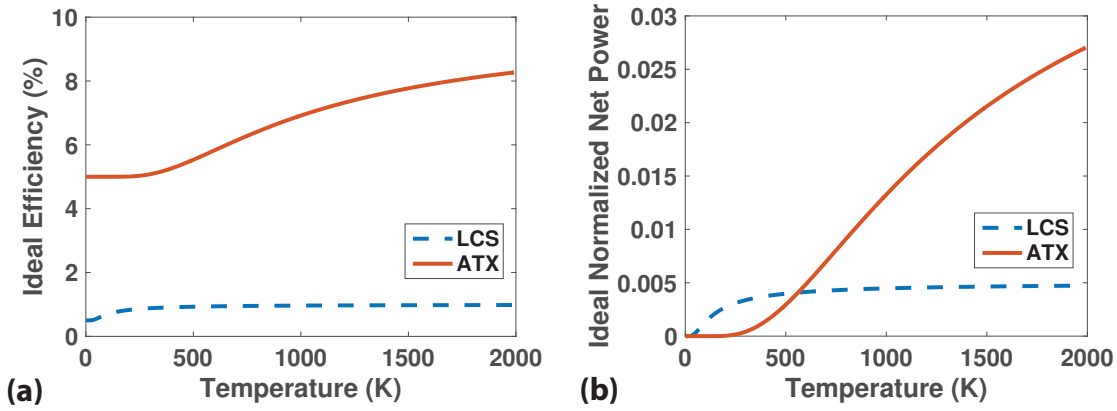

Figure 3.6: (a) Ideal efficiency versus temperature for LCS (dashed line) and ATX (solid line) from Eq. 3.39. (b) normalized extracted ideal net power versus medium temperature of LCS (dashed line) and ATX (solid line) from the absolute value of Eq. 3.40. ATX has a higher ideal efficiency than LCS but LCS outperforms ATX for extracted power at lower temperatures.

To compare the ideal net power, we use the form of normalized power with respect to incident absorbed pump power as defined in Eq. 3.40 and plot the extracted ideal net power $|P_{net}/(I\sigma_{12}N_t)|$ as shown in Fig. 3.6(b). Figure 3.6(b) shows that at higher temperatures more power can be extracted using our ATX scheme compared to that with the LCS scheme. However, at lower temperatures then LCS extracts more power than does ATX. These results are expected since if when $kT \ll \delta E_g$ the excited state of the manifold will be depopulated as discussed in Ref. [103] and in Section 3.4. The higher energy gap δE in ATX means that this depopulation occurs at higher temperatures compared to the relevant depopulation temperature for LCS.

Parasitic losses

Thus far, we have neglected non-idealities such as parasitic pump absorption and non-unity quantum efficiency. In reality, these process will degrade the performance of both LCS [103] and ATX for cooling and temperature sensing applications. We now examine these effects.

The key parasitic losses in LCS are parasitic pump absorption and non-radiative recombination of upconverted photons (manifested by a non-unity quantum efficiency), and both of these processes will occur in ATX as well. We first consider parasitic absorption of the pump. Here, the pump wavelength here is chosen to be 1 μm (1.24 eV) and most host materials such as ZBLANP or YLF [103] are transparent at this wavelength in LCS. In ATX, the requirement for the host materials to be transparent up to MIR limits host materials to those that are 100% transparent at 1 μm such as calcium fluoride. In ATX, however, there is also the possibility of pump absorption by the substrate in a simple geometry such as in Fig. 3.5(c). The details of how much pump absorption occurs depends strongly on the material properties and system design. However, it is clear that cooling applications using ATX will require thin substrates that do not absorb light in the visible or near-infrared wavelengths used for the pump.

Next, we consider non-radiative recombination of upconverted photons. These

non-radiative channels are represented by γ_{nr} for the all transitions in Figs. 3.5(b) and (d) and are caused by multi-phonon decay processes governed by Eq. 3.37. Upconverted photons require at least 97% internal quantum efficiency (assuming unity absorption efficiency and fluorescence escape efficiency) in order for any cooling to occur in LCS [103]. Thus, host materials in LCS often have low maximum phonon energy to reduce the probability of multi-phonon processes [135]. In ATX, the mean fluorescence energy is larger than in LCS due to a larger energy gap δE, which should result in a reduction in parasitic multi-phonon decay processes.

However, the elevated temperatures required for optimal performance of ATX could lead to a dramatic increase in non-radiative recombination. This challenge may be avoided by recognizing that the temperature of the host medium need not equal that of the thermal radiation emitted by the substrate. In ATX, the substrate determined the thermal photon population, unlike LCS where the physical temperature of the host material of the gain medium that determines the phonon population. Thus, the host material in ATX can be maintained at a lower temperature compared to that of the substrate by contact with a thermal reservoir. As a result, non-radiative recombination may be significantly smaller than anticipated despite the elevated temperature of the substrate.

Overall, parasitic losses should affect LCS and ATX to a similar extent and it is possible that radiative cooling could be achieved with ATX. Nevertheless, specialized experimental design plays a key role in achieving cooling in LCS [100–102, 119–122] and similar careful design will be required for achieving cooling using ATX.

3.6 Discussion

With the mathematical formalism in place and the parasitic processes in mind, we now examine the applications of ATX for temperature sensing. The key quantities are the upconverted power reaching the detector and the sensitivity of the upconverted power to variations in temperature. Using the same assumptions in Section 3.5, we simplify Eqs. 3.19 and 3.29 to obtain the upconverted power normalized to absorbed

input power as

$$\frac{P_{upconvert}}{I\sigma_{12}N_t} \approx \left(\frac{1}{1+\exp(\frac{\delta E_{LCS,ATX}}{kT})}\right)(\frac{\delta E_{LCS,ATX}}{\hbar\omega}(\frac{1}{2}+\frac{1}{1+\exp(\frac{\delta E_{LCS,ATX}}{kT})}) + \frac{1}{2}(1+\frac{1}{1+\exp(\frac{\delta E_{LCS,ATX}}{kT})})) \quad (3.41)$$

The sensitivity of upconverted power to variations in temperature defined as $dP_{upconvert}/dT$ is then

$$\frac{dP_{upconvert}}{dT} = \frac{\exp(\frac{\delta E_{LCS,ATX}}{k_bT})\delta E_{LCS,ATX}\left(5\delta E_{LCS,ATX}+3\hbar\omega+\exp(\frac{\delta E_{LCS,ATX}}{k_bT})(\delta E_{LCS,ATX}+\hbar\omega)\right)}{2\left(1+\exp(\frac{\delta E_{LCS,ATX}}{k_bT})\right)^3 k_bT^2\hbar\omega} \quad (3.42)$$

Figure 3.7(a) shows the comparison of the normalized upconverted power and radiation temperature for ATX versus LCS using Eq. **??** with pump energy $\hbar\omega = 1.24$ eV for both schemes. The higher power output for LCS is due to the smaller energy of the manifold that allows a higher thermal population of the excited state. In Fig. 3.7(b), the sensitivity of LCS is lower than ATX at higher temperatures although it is much higher below 500 K.

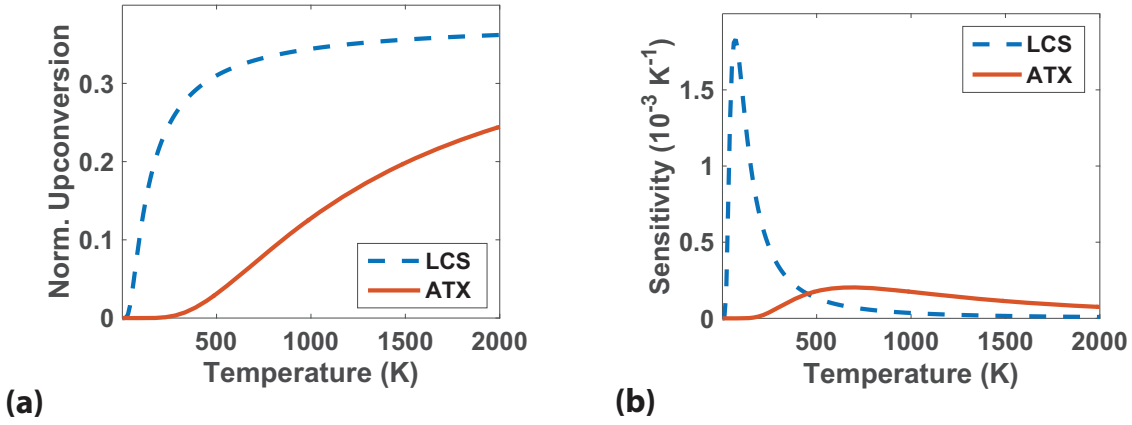

Figure 3.7: (a) Normalized upconverted power versus temperature for LCS (dashed line) and ATX (solid line) from Eq. 3.39. (b) Sensitivity of upconverted fluorescence versus sensing temperature of LCS (dashed line) and ATX (solid line) from the absolute value of Eq. 3.40. ATX has a higher sensitivity than LCS at higher temperatures but LCS outperforms ATX for extracted power for the temperature range considered.

Overall, the comparison here shows that LCS is better for temperature sensing for

the temperature range considered as $\delta E \ll k_b T$. If contact between the fluorescence medium and the sample is acceptable, LCS based temperature sensing has the advantages of good spatial resolution to local temperature and convenient optical detection in the visible to near infrared wavelength range [123–130].

On the other hand, ATX enables temperature measurement by sampling the near- or far-field radiation of the substrate without requiring any physical contact. Such non-contact temperature sensing is important for a wide range of applications from medical to industrial domains. Current techniques often employ semiconductor based infrared photon detectors or bolometer based detectors [136, 137]. The limited detection range of various semiconductor materials and the slow response of bolometers restricts the application of these techniques [136, 137]. Temperature sensing using ATX allows the use of visible to near infrared photo detectors to detect the upconverted fluorescence which are fast and widely available. Thus, ATX may enable temperature sensing with high spatial accuracy when combined with existing near-field scanning techniques [138,139] by upconverting thermal radiation to near infrared or visible wavelengths for detection without requiring any physical contact with the sample.

3.7 Discussion

Our work shares some similarities with laser cooling of solids [100–102,140] and active schemes in plasmonics [115,116,141], photonic crystals [142], and metamaterials [143, 144] but differs in a number of important ways. First, laser cooling directly extracts phonons, while our scheme extracts surface phonon polaritons. Therefore, our scheme has potential to be much more efficient than laser cooling because of the significantly higher energy of surface phonon polaritons than phonons. For instance, the ideal efficiency of laser cooling of solids is typically a few percent [100–102], while our ideal efficiency is 50% for the chosen wavelengths if the 2-0 transition has unity quantum efficiency. Further reduction in the pump fluence can be made by optimizing pump recycling. Also, laser cooling requires the medium to be cooled to possess very specific

energy levels, whereas our scheme only requires that the medium possess a surface resonance.

The most important difference between this work and prior works on near-field coupling and gain media [115–117, 141] is that in the present work, the atomic transition is pumped by a near-field thermal radiative source rather than a coherent pump. Unlike typical broadband radiation in the far-field, the nearly monochromatic nature of near-field thermal radiation allows atomic transitions to be efficiently driven, a concept that could be used for other photonics applications. However, although the near-field energy density is high compared to that in the far-field, it is not sufficient to cause the imaginary part of permittivity of the gain medium to become positive; our medium is actually absorptive under all conditions. Our approach does not lead to any form of stimulated emission or coherent single mode emission and thus is distinctly different from active schemes in plasmonics used to realize spasers [115–117, 141] or to compensate loss [143, 144].

3.8 Conclusion

In conclusion, we have numerically demonstrated an active thermal extraction scheme that allows bound surface waves to be converted from evanescent to propagating waves. Our laser-based cooling approach exploits the monochromatic nature of near-field radiation to drive a transition in a gain medium simultaneously with an external pump, thereby extracting near-field energy to the far-field. We have also outlined the generalized theory of ARC and demonstrates a mathematical equivalence between LCS and ARC by replacing the electron-phonon coupling parameter in LCS with the electron-photon coupling parameter in ARC. With this equivalence, we compare LCS with ARC using realistic parameters. Overall, ARC outperforms LCS in both efficiency and extracted power. We find ATX potentially advantageous at higher temperatures for which the energy gap $\delta E \sim k_b T$. The generalized model for ATX presented here will thus advance the understanding and application of utilizing active processes to manipulate near-field thermal radiation for thermal management.

Chapter 4

Understanding Quasiballistic Transport Using Monte-Carlo Technique

Contents of this chapter can also be found in Ref. [145].

4.1 Introduction

Thermal transport at the nanoscale has attracted substantial interest in recent years [3, 37–40]. In many solids, phonons are the main heat carrier and mean free paths (MFPs) are comparable to the dimensions of micro to nano-size devices [146]. Reduced thermal conductivity due to phonon scattering at boundaries and interfaces has been demonstrated in numerous material systems, and many of these nanostructured materials are under investigation as thermoelectrics [46–48, 51–53].

Engineering thermal conductivity using classical size effects requires knowledge of phonon MFPs [54]. Recently, there have been various efforts to measure MFP spectra experimentally using observations of quasiballistic heat conduction [8, 43, 55–57]. In these methods, the MFP distribution is obtained by analyzing the change in measured thermal conductivity as a thermal length scale is systematically varied. This thermal length has been defined using lithographically patterned heaters [56], the cross-plane thermal penetration length [55, 57], and the pump beam size in time-domain thermal reflectance (TDTR) [8]. The MFP distribution can be reconstructed

from these measurements using a method introduced by Minnich provided that the quasiballistic transport in the experiment can be accurately simulated [61].

Quasiballistic transport has been studied using simulation with a variety of techniques [7, 147–151]. Ezzahri et al. used a Green's function formulation to examine electronic ballistic transport [148]. Cruz et al. used ab-inito calculations in an attempt to explain a modulation frequency dependence of thermal conductivity in TDTR [150]. Heat transport in the cross-plane direction in TDTR experiments have been studied by numerically solving the 1D Boltzmann Transport equation (BTE) [149] and by using a two-channel model of the BTE [151]. While radial quasiballistic transport due to variation of the pump size in TDTR experiment has been studied as an example of the Monte-Carlo method [7,152], there has been no systematic investigation of radial quasiballistic transport in TDTR.

In this chapter, we present a numerical study of the heat conduction that occurs in the full 3D geometry of a TDTR experiment, including an interface, using the BTE. We identify a radial suppression function that describes the suppression of heat flux, compared to the Fourier's law prediction, when length scales are comparable to MFPs. The prediction of our radial suppression function is in good agreement with the reduction in thermal conductivity observed with TDTR at room temperature. We also discuss discrepancies at cryogenic temperatures that are important for future study.

4.2 Theory

4.2.1 Boltzmann Transport Equation and Monte-Carlo Method

Here we describe our numerical method to solving the transient, one-dimensional, frequency dependent phonon BTE. We first describe our solution of the BTE. The BTE is given by [153]:

$$\frac{\partial e_\omega}{\partial t} + \mathbf{v} \cdot \bigtriangledown e_\omega = -\frac{e_\omega - e_\omega^0}{\tau_\omega} \tag{4.1}$$

where e_ω is the phonon energy distribution function, ω is the angular frequency, e_ω^0 is the equilibrium energy distribution function, $\mathbf{v}$ is the group velocity, and τ_ω is the phonon frequency dependent relaxation time.

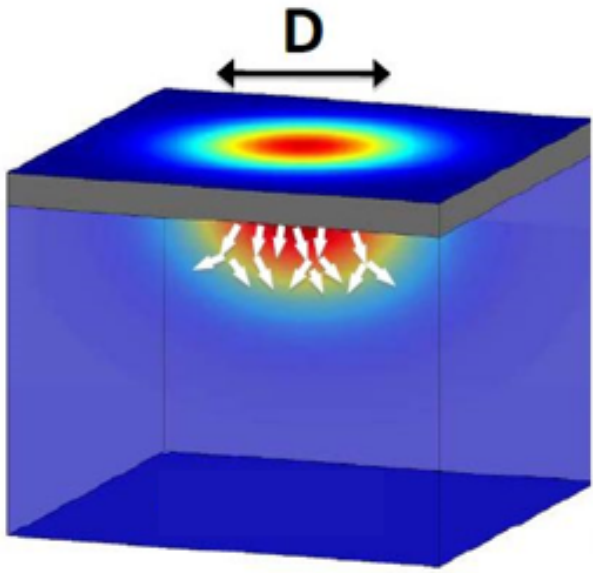

Figure 4.1: 3D sample geometry used in time-domain thermal reflectance (TDTR) experiments. The top layer is a metal transducer that absorbs the pump energy and generates thermal phonons. The phonons then propagate through the interface into the substrate.

This equation must be solved in the 3D geometry of a sample in a TDTR experiment as shown in Fig. 4.2.1, which consists of a thin metal transducer on a substrate with a Gaussian initial temperature distribution in the metal transducer [80, 154]. Solving the BTE in this domain is challenging due to its large spatial extent and the 3D geometry. Rather than using deterministic methods which require substantial amounts of memory, we use the Monte Carlo (MC) method [7]. Figure 4.2.1 illustrates the principle of MC method. Particles or phonon bundles represent a collection of phonons with the same parameters (frequency, velocity, etc.) and each particle traverses the simulation domain with some or all of its parameters resampled after each scattering or collision with a boundary.

The MC method for phonon transport was first used by Peterson [155] and improved by Mazumdar and Majumdar [156]. While there were various improvements

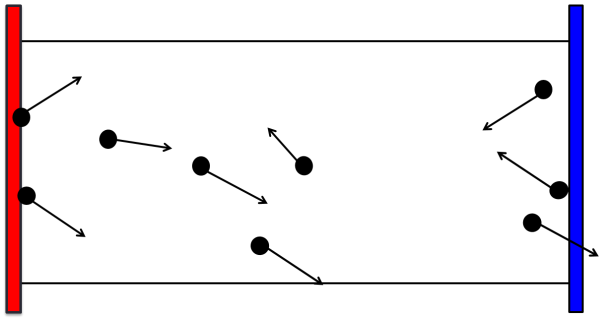

Figure 4.2: Schematic of Monte Carlo (MC) techniques in a simple geometry with two boundaries of different temperatures. The "particles" represent collections of phonons with the same frequency, velocity, etc. traveling in the domain of the simulated region. The parameters (frequency, velocity, etc.) at each boundary are sampled randomly based on material parameters and boundary conditions.

over the years [157–159], it still takes a long time to run these MC algorithms. Recently, Homolle et al. developed a variance reduced method first used for MC solutions of the BTE in dilute gases [160]. The basic concept of this method is illustrated in Fig. 4.3. Instead of sampling the whole distribution, the variance reduction in deviational MC methods calculates the deviation from a known Bose-Einstein distribution, which is a lot smaller, leading to significant computational savings [7]. Further computational efficiency can be obtained by linearizing the equilibrium distribution, eliminating the need for spatial and temporal discretization [152]. The energy assigned to particles in this approach is the deviational energy from a known equilibrium function.

4.2.2 Details of Simulation

We use the algorithm exactly as described in Ref. [152]. We note that an actual TDTR experiment measures the response to a modulated pulse train rather than the impulse response from a single pulse [149]. Because radial effects are expected to be the same for the impulse and multi-pulse response, for simplicity we only consider a single pulse in our study.

The MC simulation is divided into three main stages, namely initialization, advection and scattering, and data collection and post processing. During the initialization

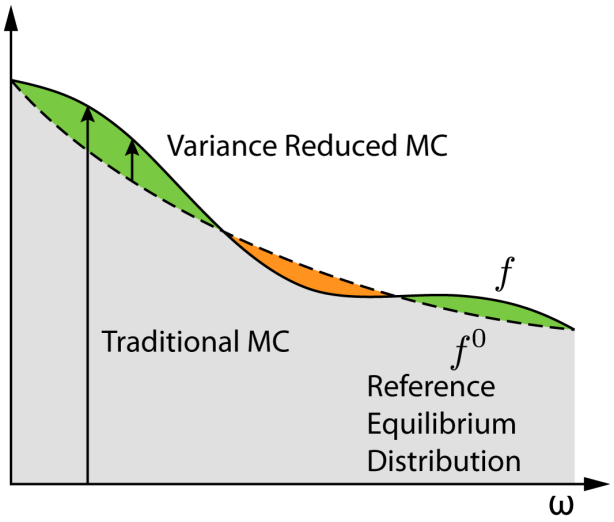

Figure 4.3: Schematic of principle underlying the variance-reduced technique. Instead of sampling the whole distribution in tranditional MC technique, the variance reduction in deviational MC methods calculates the deviation from a known Bose-Einstein distribution, which is a lot smaller, leading to significant computational savings [7].

stage, all constants and variables are defined. These include cumulative distributions upon which parameters will be sampled from as well as parameters for all particles at the start of the simulation. The advection step follows from the BTE (Eq. 4.1) which amounts to moving each particle by a vector $\mathbf{v}\Delta t$, where Δt is the traveling time step of the particle inside the simulation domain without scattering and $\mathbf{v}$ is the group velocity. The traveling time is sampled from the scattering time τ. The particle is then scattered at the new location and its parameters are re-sampled upon scattering. This scattering for-loop continues until the total travel time of the particle exceeds the maximum time allocated for the simulation. The data for the location of each particle are recorded at specific time of interest which are then post-processed to obtain the temperature versus time plot like that shown in Fig. 4.4(a). The details of each stage are described below.

4.2.3 Initialization

During the initialization stage, the initial temperature distribution is used to distribute the computational domain with particles in order to account for this temper-

ature distribution.

4.2.3.1 Initial Position and Time

We consider a simulation geometry similar to the typical TDTR samples as shown in the inset in Fig. 4.4. Here, the top layer is an Al film and the bottom layer is a layer of semi-infinite Si. We simulate the probing process of surface temperature in a TDTR measurement by averaging the surface energy distribution with a Gaussian function. The probe is assumed to be of the same size as that of the pump. The transducer thickness is set to 10 nm to reduce its thermal resistance.

The computational domain is divided into around N_r cells radially according to $r_m = \sqrt{j/N_r}2R$ for the mth cell up to $2R$. This ensures that each volume element is the same size. The thickness of the nth cell along the cross-plane direction has $\Delta z_n = \Delta z = 5$nm. The volume of each cell is thus $\Delta V_{m,n} = \pi(r_0^2)\Delta z_n$.

To approximate a two-dimensional temperature profile, we initialize all particles inside a 5 nm thick Al region. The deviational energy carried by each particle is computationally calculated based on the total deviational energy for all particles divided by number of particles N_{eff} according to [152]

$$e_i \approx \frac{1}{N_{eff}} \sum_m \sum_n \sum_p \sum_q D(\omega_q, p) \frac{de^{eq}(\omega_q, p, T_{eq})}{dT} \Delta\omega_q \Delta T_{n,m} \Delta V_{m,n} \tag{4.2}$$

by summing along the radial and cross-plane direction. $\Delta T_{n,m}$ and $\Delta V_{m,n}$ are the temperature and volume of each spatial unit cell. $\Delta\omega_q$ is the frequency of each discretized phonon mode for each polarization p. $D(\omega_q, p)$ is the density of states and $\tau(\omega_q, p)$ is the scattering time. $de^{eq}(\omega_q, p, T_{eq})/dT$ represents the linearized form of the known energy distribution function using Bose-Einstein statistics

$$\frac{de^{eq}(\omega_q, p, T)}{dT} = \frac{d}{dT}\left(\frac{\hbar\omega_q}{\exp\left(\frac{\hbar\omega_p}{k_b T}\right) - 1}\right) \tag{4.3}$$

where k_b is the Boltzmann factor. The equilibrium temperature $T_{eq} = 300$ K in Eq.

4.2.

Note that N_{eff} is not the actual number of phonons in the domain. This was discussed in Ref. [7] and the value of N_{eff} depends on the balance of computational cost versus having a sufficiently large number of particles for significant level of sampling. Typically, $\sim 10^6$ particles is sufficient for this simulation.

The temperature $\Delta T_{n,m}$ of each cell is given according to the initial Gaussian temperature distribution described as

$$\Delta T_{n,m} = \begin{cases} T_0 \exp(-2\frac{r_m^2}{R^2}) & : z \in [0, \Delta z_n] \\ 0 & z > \Delta z_n \end{cases} \tag{4.4}$$

where $T_0 = 2Q_0/(\pi R^2 \Delta z_n C_{Al})$. The energy of a pulse is assumed to be $Q_0 = 0.01$J and C_{Al} is the volumetric specific heat capacity of Al in units of J/m^3K. Q_0 is kept constant for different value of radius R in our calculations, representing the same pulse energy for different beam diameters. In Ref. [7], depending on the choice of equilibrium temperature T_{eq}, there are many cases in which the sign of the particle is important if initial temperature is below T_{eq} such that $\Delta T < 0$ in Eq. 4.2. However, this is not a concern for us, as the temperature in the domain is always bigger than the initial temperature, as in Eq. 4.4.

The initial time of each particle is $t = 0$.

4.2.3.2 Frequency Distribution

We first discretize the phonon dispersion into 1000 bins; the phonon dispersion is taken to be that of Si along the [100] direction as described in Ref. [149] and only acoustic phonons are considered. We take the metal transducer to have the same dispersion as the experimental dispersion of Al in the [100] direction and neglect heat conduction by electrons, instead considering phonons as the sole heat carrier. In reality, electrons conduct a majority of the heat in metals. However, it has been demonstrated that there exists thermal resistance due to electron-phonon coupling which modifies the effective interface conductance value [161]. As we would like to

isolate changes in thermal properties due to quasi-ballistic transport only, we do not take electron heat conduction into consideration. Following Ref. [149], we assign a phonon to have a constant relaxation time of 1 ps, yielding a low thermal conductivity of around 3 W $m^{-1}K^{-1}$. This change eliminates any possible artificial quasiballistic effects in the metal transducer, attributing all quasiballistic effects to the Si substrate. For $t = 0$, all particles will be in Al.

Using the dispersion for Al and Eq. 4.3, we construct the cumulative distribution for sampling frequency according to [7]

$$F(q) = \frac{1}{N_p} \sum_{q=0}^{q} \sum_{p} D(\omega_q, p) \frac{de^{eq}(\omega_q, p, T_{eq})}{dT} \Delta\omega_q \tag{4.5}$$

where N_p is the normalization factor. ω_q represent qth phonon frequency in 1000 bins. Thus, the probability of the selecting the qth frequency for each particle is given by $F(q)$ in Eq. 4.5.

Choosing the polarization depends on the frequency that has been selected such that the probability for a particular polarization p after the frequency of the particle is determined by ratio of density of states $D(\omega, p)/\sum_p D(\omega, p)$.

4.2.3.3 Velocity Distribution

The absolute value of the group velocity $\mathbf{v}$ of a particle can be obtained from the phonon dispersion after choosing its frequency ω and polarization p. The direction of group velocity $\mathbf{v}$ is sampled with two uniformly distributed random numbers [156] in $R \in [0, 1]$ and $\phi \in [0, 2\pi]$. From these two numbers, the direction in x, y, z is then given by

$$\mathbf{v} = \begin{pmatrix} v_x \\ v_y \\ v_z \end{pmatrix} = v(\omega, p) \begin{pmatrix} \sqrt{1 - R^2} \cos\phi \\ \sqrt{1 - R^2} \sin(\phi) \\ R \end{pmatrix} \tag{4.6}$$

where $v(\omega, p)$ is the magnitude of the group velocity. Equation 4.6 is both used to generate directions at time $t = 0$ and after each scattering event during the simulation. However, reflections at interfaces does not follow Eq. 4.6 due to the difference in the available range of solid angle.

4.2.4 Advection and Scattering

4.2.4.1 Advection Time Step

Once the simulation starts, each loop begins begins by moving each particle by a time step Δt. This time step represents the amount of time the particle can travel without being scattered. Therefore, time step Δt is sampled according to scattering times of Al or Si depending on the location of the particle before advection. The procedure to sample a time step Δt for each particle uses the following relationship

$$\Delta t = \tau_{eff} \ln (1 - P_i) \tag{4.7}$$

where P_i is a uniformly distributed random number between zero and one. τ_{eff} is the effective scattering time that depends on the material properties according to

$$\frac{1}{\tau_{eff}} = \frac{1}{\sum_p \tau(\omega, p, T_e ff)} \tag{4.8}$$

where $\tau(\omega, p, T_e ff)$ are polarization, frequency, and temperature dependent relaxation times also taken from Ref. [149].

4.2.4.2 Interface and Boundary Conditions

At the interface, phonons have a probability to be transmitted or reflected diffusely according to the model of Ref. [149]. The top surface of the metal transducer is taken to be a diffuse mirror, and all other boundaries are semi-infinite with no condition enforced. Upon advecting a particle with sampled group velocity $\mathbf{v}$ and time step Δt, one of the following cases can occur:

- The particle collides with the $z = 0$ diffuse boundary in Al before the end of its sampled time step. In this case, the particle will be diffusely reflected, which means that the direction of the particle is randomized with no change to other parameters. The time step that the particle traverses will also be shortened to the time it takes for the particle to reach the boundary. In this case, the new velocity upon reflection is sampled in a slightly different manner compared to Eq. 4.6 using

$$\mathbf{v} = \begin{pmatrix} v_x \\ v_y \\ v_z \end{pmatrix} = v(\omega, p) \begin{pmatrix} \sqrt{1-R}\cos\phi \\ \sqrt{1-R}\sin\phi \\ \sqrt{R} \end{pmatrix} \tag{4.9}$$

  The difference is due to directional averaging of $\mathbf{v}$ with the normal vector of the boundary [156].

- The particle collides with the interface going from Al to Si or from Si to Al before it can scatter according to the model of Ref. [149]. In this model, we set $P_{Al\to Si}$ to be a frequency-independent probability of transmission crossing the interface from Al to Si. $P_{Al\to Si}$ can be obtained using Eq. (16) of Ref. [149] which depends on the material properties of each and the interface conductance G. $P_{Si\to Al}$ is obtained using the principle of detailed balance for each frequency and polarization.

  Due to mismatch in the cut-off frequency for each branch of the dispersion between Al and Si, some high frequency phonons in one material do not have a corresponding state at the same frequency in the other material. Under the assumption of elastic scattering and a neglect of mode conversion, these phonons will have zero probability of transmission and will be diffusely reflected according to Eq. 4.9. For particles with non-zero transmission probability, a random number will be drawn and compared to the probability of transmission to determine if it will transmit or be diffusely reflected. If the particle does get transmitted to the other side of the interface, it will retain its frequency and

polarization but will have its direction redrawn also according to Eq. 4.9.

- If the particle does not encounter any boundary, it will be scattered upon reaching its new location after a time step of Δt. A new set of parameters will be redrawn upon scattering. Sampling of frequency will be according to [152]

$$F(q) = \frac{1}{N_p} \sum_{q=0}^{q} \sum_{p} \frac{D(\omega_q, p)}{\tau(\omega_q, p, T_{eq})} \frac{de^{eq}(\omega_q, p, T_{eq})}{dT} \Delta\omega_q \tag{4.10}$$

  instead of Eq. 4.5 with an additional dependence on scattering time τ. Likewise, the polarization can be redrawn from $D(\omega, p)/\tau(\omega_q, p, T_{eq})/\left(\sum_p D(\omega, p)/\tau(\omega_q, p, T_{eq})\right)$ with a dependence on scattering time τ as well. The direction of velocity $\mathbf{v}$ will be redrawn, according to Eq. 4.6.

4.2.5 Data Collection and Post-Processing

Data collection is challenging in MC simulations as each particle has so many variables to keep track of. Also, each time step is randomly chosen such that the collected data cannot be binned in regular time intervals. Collecting all data for every particle is theoretically possible but very costly with the large particle numbers used in this simulation. We devised a strategy to overcome this issue by only keeping the necessary data of interest to us. Our method is as follows:

- We prepare a time grid that consists of a logarithmic interval of time steps markers.

- After each advection loop, we check the total time traversed by each particle to see if it exceeds any of the time steps in the grid. Only if the particle exceeds a time step, we record the time step and all relevant data before and after the advection step. If any advection step jumped more than one marker on the grid, we record the same time before and after advection only at the last marker.

- If the total time traversed by the particle reaches the maximum simulation time allocated, then data for the last time marker will be recorded and the particle

will be removed from the next loop.

In TDTR experiments, the probe beam measures the surface temperature averaged over its Gaussian beam spot with respect to time. Here, we mimic the measurement of a probe beam by gathering the average temperature at the surface with Gaussian distributed weighting. To do so, we gather the temperature of each point at the surface (also within 5 nm from $z = 0$) at each time marker. The temperature at each point is proportional to the number of particles at each point divided by the total volume of the region of interest and the volumetric specific heat of Al (C_{Al}). The discretization of the spatial domain into unit cells of equal volume in Section 4.2.3.1 allows one to assign particles to individual unit cells according to its location. The location at a particular time can be interpolated from the recorded spatial data for each time marker.

Upon obtaining the temperature in each cell, we assign a Gaussian weight of $\rho(r_m)$ to the mth cell multiplied by the number of particles $N(m)$ inside each unit cell. The averaged temperature sampled by the probe is thus proportional to $\sum_m N(m)\rho(r_m)$. Averaging of the probe is equivalent to convolution of the Gaussian weighting of the probe to a Gaussian temperature of the pump in Eq. 4.4 [154]. Mathematically, our numerical averaging should yield the same result as a convolution. Thus, we have the following relation:

$$\sum_m N(m)\rho(r_m) \sim \int_0^\infty \exp(-2\frac{r^2}{R^2})A_0 \exp(-2\frac{r}{R})2\pi r dr \tag{4.11}$$

where A_0 is the normalization for the weight function of the probe. From this relation, we obtain the weight function as

$$\rho(r) = \frac{2}{\pi R^2}\exp(-2\frac{r}{R}) \tag{4.12}$$

Using this relation, we can find the average temperature computationally with

$$\langle \Delta T \rangle = \frac{e_j \sum_m N(m)\rho(r_m)}{C_{Al}\Delta z} \tag{4.13}$$

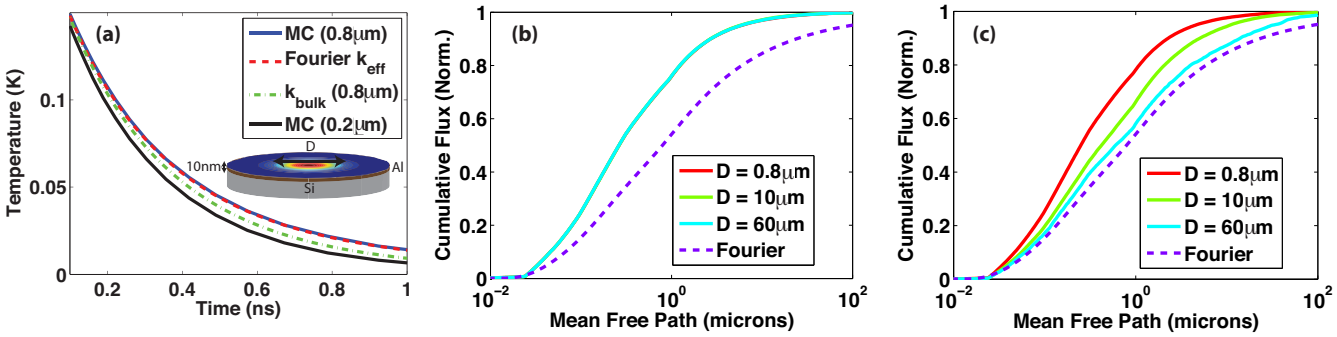

Figure 4.4: (a) The MC simulation (blue line) for a pump beam of $D = 0.8$ μm is fitted to Fourier's law (red dashed line) with an effective thermal conductivity $k_{eff} = 65$ W/mK at 300 K. Fourier's law with $k_{bulk} = 148.2$ W/mK (green dot dashed line) shows a faster decay. The MC simulation (black line) for pump beam of $D = 0.2$ μm is also shown for comparison. All MC simulations and Fourier's law fits use the specified interfacial conductance $G = 110$ MW/m^{2}K. The inset in (a) shows the simulated sample geometry of a Al film of thickness 10 nm on a semi-infinite Si substrate, illuminated with a Gaussian pump beam of diameter D. (b,c) Normalized cumulative heat flux in the (b) cross-plane or (c) radial direction for different pump diameters at 300 K (solid line). The purple dashed line is the expected normalized cumulative heat flux based on Fourier's law. The cross-plane heat flux in (b) does not depend on pump diameter.

4.3 Results

4.3.1 Temperature versus Time and Heat Flux

We can gain more insight into the thermal transport by examining the pump diameter dependence of the effective thermal conductivities, which are obtained by fitting the BTE decay curve with a Fourier's law model [61]. Though the heat flux is anisotropic, we fit the decay with an isotropic model for two reasons. First, most TDTR measurements are taken using concentric pump and probe, for which extracting anisotropic thermal conductivity is not always possible. Second, the sensitivity of the decay to radial thermal conductivity k_r decreases with increasing pump beam size, leading to large uncertainties in the fitted k_r. For these reasons, we fit the decay curves using an isotropic effective thermal conductivity, which is a measure of the net heat flux away from the heated region, and account for the additional cross-plane suppression separately.

For each value of pump diameter, we use a standard Fourier model for Gaussian heating in a layered structure [154] to fit an effective thermal conductivity to the MC temperature data. Fitting to Fourier model requires solving the spatial Hankel-transformed second order differential equation with a standard Crank-Nicolson Finite Difference technique [162]. The boundary and interface conditions follows the matrix method for multiple layers [154]. The fitted value is obtained by minimizing the norm of the difference between the MC and Fourier decay curves. We take the interface conductance G to be the value used to calculate the transmissivity $P_{Al\rightarrow Si}$ for the BTE calculation.

An example transient decay curve for $D = 0.8$ μm and $D = 0.2$ μm along with the corresponding Fourier law prediction using the bulk thermal conductivity is shown in Fig. 4.4(a). As in prior works [7, 149], the thermal decay predicted by the BTE is slower than Fourier's law predicts. To understand the origin of this slow thermal decay, we calculate the heat flux in the radial and cross-plane directions. The cumulative heat flux is proportional to $\sum_j s_j L_j$, where L_j is the algebraic distance traveled in a specified direction by the jth particle between two consecutive scattering events and s_j is the sign of the deviational phonon [152]. In the simulation, the distance traveled L_j in plane or cross plane by the jth particle is added to the total heat flux for each loop regardless of any markers in the time grid. The summed distance for each particle is then be binned according to its frequency, polarization, and direction and added to the total sum for each bin. We only start recording after the particle first passed the interface from Al to Si. To index heat flux as a function of MFP, we have to perform a numerical change of variables from frequency and polarization to MFP. This change is done by first obtaining the corresponding MFP at each frequency and polarization and plotting flux as a function of MFP for each polarization. Then we make a common grid for MFP which is used to interpolate the flux from each polarization. These fluxes are the summed over all polarization based on the same MFP to obtain the overall flux as a function of MFP. Lastly, we normalize the total cumulative heat flux with respect to its maximum value.

The calculated normalized cumulative heat flux in the cross-plane and radial di-

rections for several pump beam sizes are shown in Figs. 4.4(b) and (c), respectively. Note that the BTE cumulative heat flux is restricted to smaller MFPs than those for Fourier's law in Figs. 4.4(b) and (c). Therefore, the cumulative heat flux in both directions is less than what Fourier's law predicts for long MFP phonons. Figs. 4.4(b) and (c). However, we observe that the suppression of long MFP phonons in the cross-plane direction is independent of the pump diameter D, while in the radial direction the suppression depends on D, with the actual heat flux approaching the Fourier law heat flux for larger values of D. The heat flux is therefore anisotropic when considering the degree of deviation from Fourier's Law along each transport direction. The diameter dependence of the radial heat flux demonstrates that the pump size is a key variable that sets the thermal length scale for radial transport, confirming previous explanations for observations of a pump-beam size dependent thermal conductivity [8]. The physical reason for this radial suppression is because Fourier's law assumes the existence of scattering events that are not actually taking place [41].

The fitted thermal conductivities versus pump diameter are shown in Fig. 4.5(a). The results show the experimentally observed trend of decreasing effective thermal conductivity with decreasing pump beam size [8]. However, Figure 4.5(a) also shows an unexpected result: the thermal conductivity does not approach the bulk value k_{bulk} of 148.2 W/mK at 300 K for Si for large values of pump diameter where radial suppression is minimal. This observation is puzzling because TDTR routinely measures the correct thermal conductivity for Si at room temperature with similar pump sizes. The reduction in thermal conductivity is due to the suppressed cross-plane heat flux in Fig.4.4(b), which apparently does not occur in the actual experiment but is consistent with earlier simulations [7,149]. The origin of this discrepancy has been resolved and is due to the an assumption of constant transmissivity at the interface [163], and further investigation is ongoing. However, our analysis remains valid because we are able to decouple the radial and cross-plane directions.

We also checked whether the interface or transducer properties affect radial quasi-ballistic transport by performing additional simulations with different values of interface conductance G, and hence transmissivity in the BTE simulation, and transducer

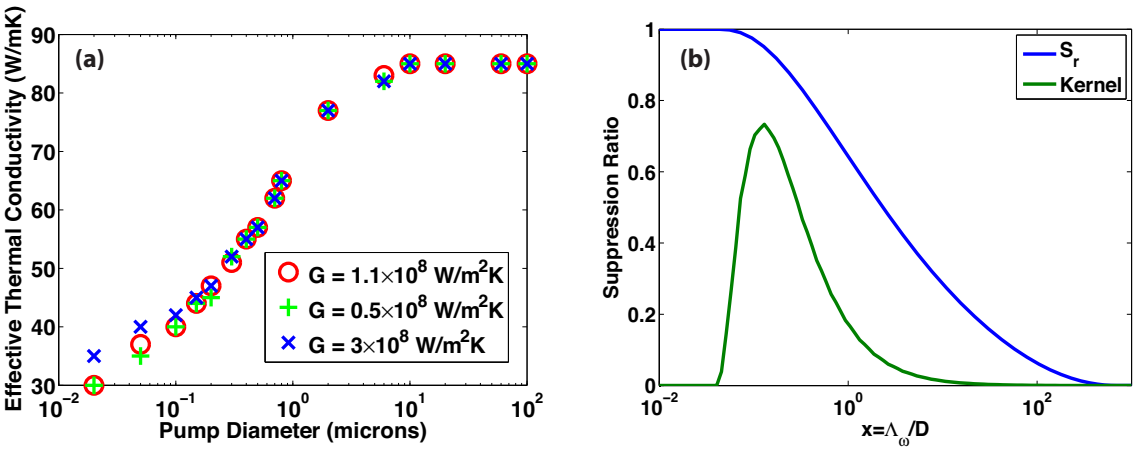

Figure 4.5: (a) Fitted effective thermal conductivity for different values of pump diameter at 300 K for several specified values of interface conductance G, with each G corresponding to a different transmissivity in the BTE model. There is no appreciable dependence of thermal conductivity on the specified interface conductance. (b) Radial suppression function S_r and the kernel K obtained from the data at 300 K. The kernel K is obtained based on the numerical differentiation of S_r.

thickness. The thermal conductivities are essentially unaffected by specified interface conductance G as shown in Fig. 4.5(a), and we also find that the thermal conductivities are not affected by transducer thickness. We therefore conclude that the pump beam size is the primary parameter that governs radial quasiballistic transport.

4.3.2 Enabling MFP Measurements

We now demonstrate how our calculations can be used to enable MFP measurements using TDTR. Minnich recently introduced a framework in which the MFP distribution of the substrate can be reconstructed from the effective thermal conductivities, as shown in Fig. 4.5(a), and a suppression function that describes the difference in heat flux between the quasiballistic and Fourier predictions [61]. This function depends on the experimental geometry and mathematically describes how the heat flux curves in Fig. 4.4(c) differ from the Fourier's law curve. The equation relating the thermal conductivity and the suppression function to the MFP distribution is given by:

$$k_i = \int_0^\infty S(x) f(xD_i) D_i dx \tag{4.14}$$

where $f(\Lambda_\omega) = \frac{1}{3}C_\omega v_\omega \Lambda_\omega$ is differential MFP distribution in the Fourier limit, D_i is the variable pump diameter, and $x = \Lambda_\omega/D$. C_ω is the volumetric specific heat and v_ω is the group velocity at phonon frequency ω. S describes how each phonon mode is suppressed as a function of MFP Λ_ω and pump diameter D_i. Previously, this equation was used to find the MFP distribution [61]. However, because here f and k_i are known, this equation can also be solved for S to find the suppression function.

A challenge is that our simulations contain both radial and cross plane suppression. To isolate only the radial suppression, we write the heat flux suppression $S(x)$ as the product of the cross-plane suppression function $S_z(\Lambda_\omega)$ and the radial suppression function $S_r(x)$. For each measurement of k_i, we now further expand Eq. 4.14 to obtain

$$k_i = \int_0^\infty S_r(x) S_z(xD_i) f(xD_i) D_i dx \tag{4.15}$$

where $x = \Lambda_\omega/D_i$ and $\int_0^\infty f(\Lambda_\omega) d\Lambda_\omega = k_{bulk}$ is the bulk value of thermal conductivity of crystalline silicon. Equation (4.15) is an homogeneous Fredholm integral equation and the desired S_r is a solution to the ill-posed problem of Equation (4.14). We solve the equation using the convex optimization method of Ref. [61]. First, we discretize the integral in Eq. 4.15 using Gaussian quadrature and obtain a linear system of equations form unknown radial suppression function $S_r(x_j)_i$ as

$$\sum_{j=1}^{N} S_z(D_i x_j) f(D_i x_j) D_i \Delta x_j S_r(x_j) = k_i \tag{4.16}$$

where N is the number of integration points and $\sum_{j=1}^{N} f(D_i x_j) D_i \Delta x_j = k_{bulk}$ with $D_i \Delta x_j$ being the discretized points for the MFP. The cross-plane suppression function $S_z(D_i x_j)$ can obtained directly by interpolating from the cross-plane heat flux data (like one in Fig. 4.4(c)).

Equation (4.16) would be impossible to solve unless some information is given about S_r. However, S_r is subjected to the following restrictions: (i) $S_r(0) = 1$, (ii) $S_r(\infty) = 0$, (iii) S_r is non-negative and monotonically increasing and (iv) S_r is also expected to be a smooth function. Therefore, we reformulated the problem as a

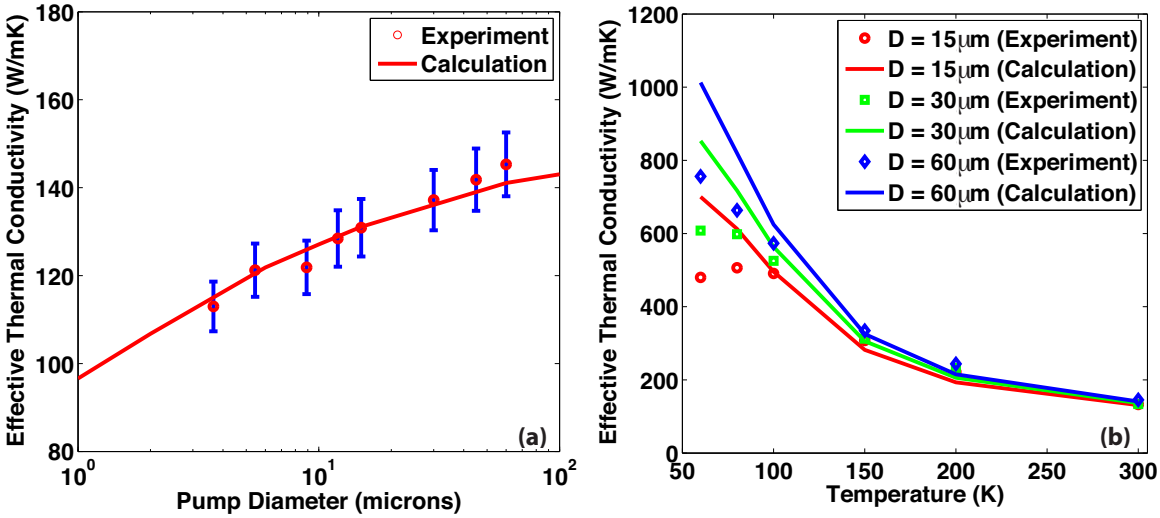

Figure 4.6: (a) Comparison of our experimental data and expected effective thermal conductivity obtained from the kernel K in Fig. 4.5(b) versus pump diameters D at 300 K. The blue errorbars indicate 10% uncertainty of our measurements. (b) Experimental (symbols, Ref. [8]) and calculated (lines) thermal conductivity as a function of temperature for different pump diameters. The calculation predicts the same trend but with a larger thermal conductivity than the experimental results.

convex optimization to minimize the penalty function P defined as

$$P = \|(S_z f \Delta\Lambda) S_r - k\|_2^2 + \eta \|\Delta^2 S_r\|_2^2 \tag{4.17}$$

where $\Delta^2 S_r = (S_r)_{j+1} - 2(S_r)_j + (S_r)_{j-1}$ and $\|.\|$ is the second-norm and η controls the smoothness of the penalty function P. To solve the penalty function in Eq. 4.14 subjected to constraints (i)-(iii), we use the CVX package [164] compatible with Matlab.

To obtain S_z and f numerically, we must index f and the cross-plane suppression function S_z with respect to MFP. S_z is independent of D_i and does not affect the radial suppression function. It can be obtained directly by interpolating the cross-plane heat flux in Fig. 4.4(c). In fact, the heat flux in Fig. 4.4 is essentially the integral $\int_0^\omega S_z(\Lambda) f(\Lambda) d\Lambda$. Thus, we obtain $S_z(\Lambda) f(\Lambda)$ together by differentiating the interpolated flux from Fig. 4.4(b).

The resulting S_r obtained from effective thermal conductivities at 300 K is shown

in Fig. 4.5(b). We verified the robustness of the solution by adding artificial noise to k_i and by removing different constraints in the convex optimization. In all cases, we recovered the same function to within 5%. We further verified our solution by confirming that our suppression function accurately predicts the heat fluxes in Fig. 4.4(c) that are calculated directly from our simulation. The derivative of S_r, denoted the kernel, is also shown in Fig. 4.5(b) and can directly be used to obtain cumulative MFP distribution of an unknown material from experimental measurements of thermal conductivity for different pump sizes with TDTR [61].

We compare the predictions of our radial suppression function with previously reported TDTR data for Si [8] and new experimental data at 300 K. To calculate the reduction in thermal conductivity due to radial suppression, we use the kernel in Fig. 4.5(b) and the cumulative MFP distribution for Si from Density Functional Theory (DFT) calculations [165]. Because the DFT calculations do not incorporate isotope scattering, we approximately account for this mechanism by scaling the MFP distribution from DFT by the ratio of natural Si's bulk thermal conductivity [166] to the DFT thermal conductivity. To compare to experiment, we use previously reported measurements on Si at cryogenic temperatures as well as new TDTR measurements of thermal conductivity versus pump size at room temperature using a standard two-tint TDTR setup [167]. The sample consists of a high-purity Si(resistivity $>$ 20000 Ω-cm) substrate coated with 70 nm Al transducer using electron-beam evaporation. The pump $1/e^2$ diameter is varied from 60 μm to 3.7 μm, while the probe $1/e^2$ diameter is kept constant at 9.5 μm for pump diameters greater than 15 μm and 2.7 μm otherwise. The spot sizes are measured using a home-built two-axis knife-edge beam profiler.

The calculated and experimental thermal conductivity versus pump size at room temperature plotted in Fig. 4.6(a). The reconstructed effective thermal conductivity from our radial suppression function agrees well with our measured TDTR data in the absence of a cross-plane suppression. We also compare the predictions of our suppression function with previously reported TDTR measurements at cryogenic temperatures down to 60 K [8], the lowest temperature available from DFT calculations [165], in Fig. 4.6(b). At these temperatures, our result predicts a similar trend

in thermal conductivity versus pump size, but our calculation overpredicts the effective thermal conductivity for all pump diameters below $T = 150$ K. This observation could be partially due to differences in isotope and defect concentration between the samples used in different measurements [149, 166]; however, the incorrect model of transmissivity may play a role. This discrepancy is an important topic for further study.

4.4 Conclusion

In conclusion, we have studied radial quasiballistic heat conduction in TDTR using the BTE. We confirm that a quasiballistic effect is responsible for thermal conductivity variations with pump size, and further identify the radial suppression function that describes the discrepancy in heat flux compared to the Fourier's law prediction. This function allows MFPs to be reconstructed variable from pump size TDTR measurements in the absence of a cross-plane suppression. The properties of the transducer and the interface do not appear to affect radial quasiballistic transport. Our work has provided insights into transport in the radial direction and recent progress in understanding the effect of the interface has solved another discrepancy in the cross-plane suppression [163].

Chapter 5

Ultrafast Transient Grating Technique

5.1 Introduction

Advancement in material development is increasingly driving the need to understand and characterize these materials. Many conventional spectroscopic and scanning probe methods are available; however, they can be difficult to implement and typically only determine chemical and electric properties rather than mechanical proprieties. This is particularly because the films can easily be damaged by any physical contact. Scaled-down or modified versions of bulk testing techniques are currently the most common methods of examining the mechanical behavior [168–170]. Thus, laser-based techniques offer attractive alternatives because they are fast and contact-free and have high spatial resolution.

From a thermal perspective, we have introduced in Chapter 1 the importance of obtaining phonon mean-free-path (MFP) information for different materials. In Chapter 4, we looked at a numerical study of examining quasiballistic transport by varying heating length scales in TDTR [8]. While time-domain thermal reflectance (TDTR) experiment is widely used to characterize thermal transport, it is not ideal for in-plane thermal measurements and the transient grating (TG) techniques are better suited for in-plane measurements. The TG technique is capable of creating thermal gradients over micron length scales that are comparable to phonon MFPs [43]. The

TG is formed by interfering short optical pulses to form a sinusoidal heating profile. The TG technique has been used as an accurate tool for determining the thermal conductivity of materials [43, 62, 171, 172] and liquids [173].

Here, we present an experimental effort to construct an ultra-fast transient grating (UTG) experiment similar to Ref. [173] to characterize thermal and mechanical properties of molybdenum disulfide. We will first briefly outline the theory of TG and then go on to discuss experimental details. Following that, we will highlight results from experimental characterization of the UTG using Si membrane and water. The discussion of measurements from molybdenum disulfide will be the topic of the following chapter.

5.2 Principle of Transient Grating

Figure 5.1 shows a simple schematic illustrating the concept of a transient grating experiment. A phase mask diffracts the pump beam which are then combined onto the sample to form a transient grating (TG) on the sample [174]. The TG is a result of interference of the two beams, causing periodic variation in intensity, which in turn causes periodic variation in the refractive index as a result of changes in electronic, thermal, or mechanical properties of the sample [175–178]. As the name suggests, the TG signal is a function of time, as the disturbance caused by the pump on the samples equilibrates with the surrounding. A probe beam through the glass window is diffracted by the presence of the TG on the sample. The signal is amplified by the other attenuated probe beam path for detection.

The theory of TG is closely related to four-wave mixing and non-linear optics. TG experiments have been conducted on many different samples in transmission and reflection geometries [176], but we will focus on the transmission geometry used for this chapter, as illustrated in Fig. 5.1.

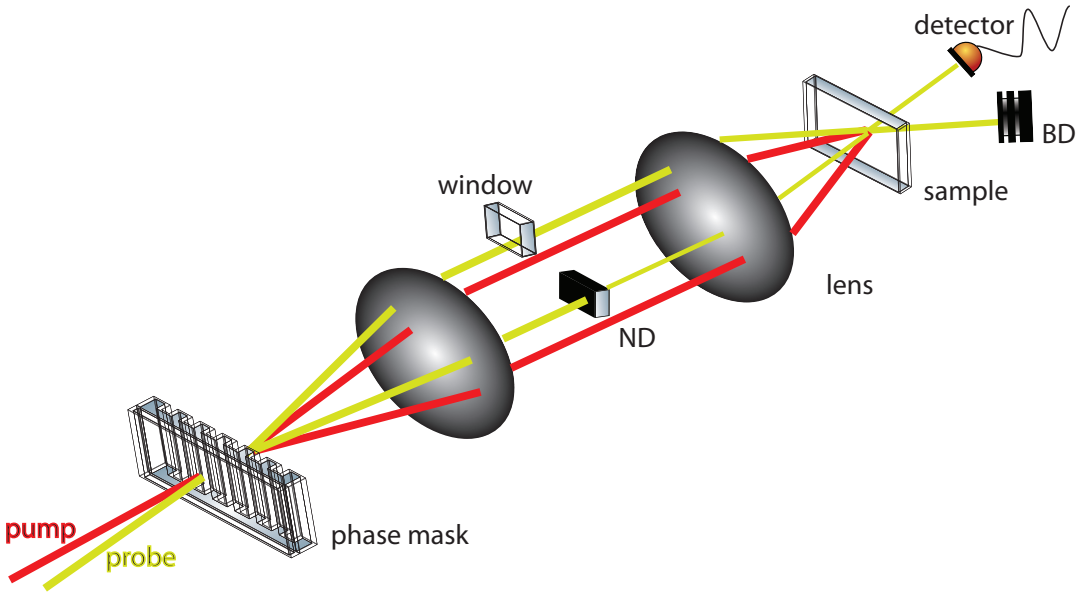

Figure 5.1: A simple schematic representing the concept of a transient grating (TG) experiment. A pump beam first arrives on the sample followed by a probe beam. A phase mask diffracts both the pump and probe beams, which are then combined onto the sample to form a transient grating (TG) on the sample. The grating pattern on the sample caused by the pump diffracts the probe beam preferentially into the photodiode. The other probe beam passing through a Neutral Density (ND) filter allows for amplification of the signal through a process of heterodyning. Figure made using drawings from Component library [9].

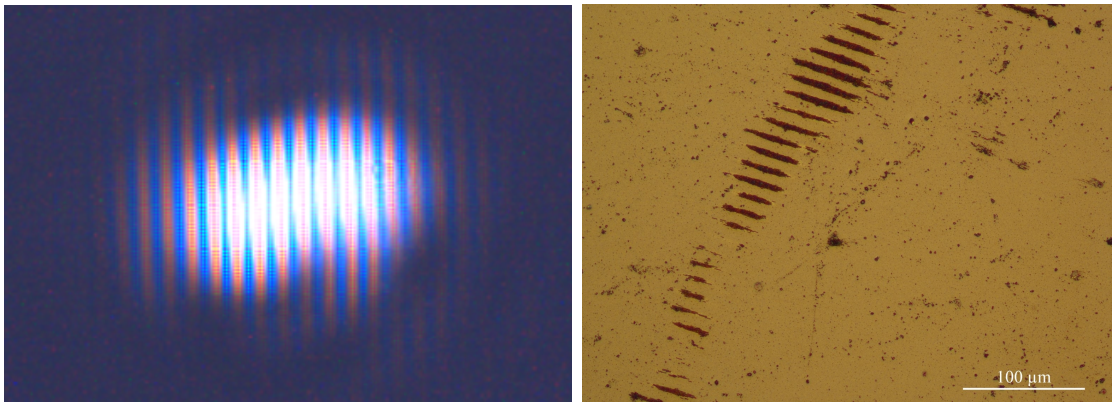

(a) (b)

Figure 5.2: (a) CCD image of an interference pattern formed due to interference of two beams. (b) Burnt grating patterns on a gold film in our experimental setup.

5.2.1 Beam Interference

Constructive and destructive interference occurs when two plane waves are crossed at an angle. For beams of the same polarization and wavelength, this interference leads to a periodic intensity profile. Figure 5.2(a) shows the image of crossing two optical beams directly overlapping on a CCD. The periodic pattern disappears when one of the beams is blocked. Figure 5.2(b) shows burned 13 μm grating on a gold film. The period of this TG is given by

$$L = \frac{2\pi}{q} = \frac{\lambda_{air}}{2\sin\frac{\theta_{air}}{2}} \tag{5.1}$$

where λ_{air} is the wavelength in air, θ_{air} is the beam crossing half-angle and q is the grating wavevector magnitude. In this work, we do not consider crossed polarized gratings and our gratings will be vertically (VV) polarized.

5.2.2 Excitation process

5.2.2.1 Impulsive stimulated thermal scattering

Upon absorbing the pump energy, periodic heating and fast thermal expansion result in a transient thermal grating. The absorption leads to temperature changes proportional to the light intensity I such that

$$\Delta T(x) \propto I_0 \cos^2\left(\frac{qx}{2}\right) = I_0\left(1+\cos(qx)\right) \tag{5.2}$$

The periodic temperature profile induces thermal stress according to [179, 180]

$$\sigma_{ij}(x) = c_{ijkl}\alpha_{kl}\Delta T(x) \propto c_{ijkl}\alpha_{kl}\cos(qx) \tag{5.3}$$

where α_{kl} is the thermal expansion tensor, c_{ijkl} is the elastic stiffness tensor, and q is the grating wavevector defined in Eq. 5.1.

The induced transient thermal stress can sometimes lead to launching of counter-propagating surface acoustic waves (SAW) and a periodic thermal grating profile that

will remain for the time heat diffuses from the grating peaks to the troughs. Strain and thermally induced changes in the refractive index will lead to diffraction of a probe beam with respect to time. This process is called impulsive stimulated thermal scattering (ISTS) [178, 181]. Oscillations in the signal are generally attributed to thermally induced strain while a slower exponentially decay is generally a result of thermal diffusion in ISTS [182]. However, not all ISTS signals have oscillations due to thermally generated strain waves, laser-induced stress due to electrostriction can also generate SAW but is not relevance to this work. One characteristic of SAW signal from ISTS is that the signal fits a sine function with integer π initial phase due to a step function nature of thermal stresses in ISTS [183].

5.2.3 Probing process and heterodyne detection

In the previous section, we described the excitation process and the subsequent material response lead to spatial and time dependence in the optical properties of the material which can be observed by a probe beam [184]. ISTS and ISBS will both excite acoustic waves due to strain and ISTS heating will lead to changes in temperature, both of which will couple to the index of refraction. In the linear regime, perturbations to the index of fraction $n + ik$ is given by [176]

$$\Delta n = \frac{\partial}{\partial X} n \Delta X \tag{5.4}$$

$$\Delta k = \frac{\partial}{\partial X} k \Delta X \tag{5.5}$$

where X can be strain or temperature. Time-dependent changes in n and k will lead respective to phase and amplitude TG signal.

The heterodyne technique shown in Fig. 5.1 allows for controlling of relative phase between two probe beams using the relative difference in tilt between the window and the ND filter on each of the probe path [185]. The word "heterodyning" refers to a radio signal processing technique invented in 1901 by Canadian inventor-engineer Reginald Fessenden, in which new frequencies are created by combining or mixing two

frequencies [186]. This process has been used to modulate and demodulate signals forming the basis of frequency division multiplexing in telecommunications. In this experiment, we use the same concept by interfering an attenuated reference beam to the diffracted signal beam and amplify the signal.

Let us consider the example in Fig. 5.1 for a transmission setup. A probe beam of wavelength λ_p is incident at the sample on the TG, and a reference beam from the same source will have the following equations for their electric fields

$$E_p = E_{0p} \exp\left(i(k_p^2 - q^2/4)^{1/2} z - i(q/2)x - i\omega_p t + i\phi_p\right) \tag{5.6}$$

$$E_R = t_r E_{0p} \exp\left(i(k_p^2 - q^2/4)^{1/2} z + i(q/2)x - i\omega_p t + i\phi_R)\right) \tag{5.7}$$

where E_{0p} is the incident probe beam amplitude, k_p is the optical wavevector, q is the TG wavevector defined in Eq. 5.1, ω_p is the optical frequency, and ϕ_p and ϕ_R are the phases of the probe and the reference beams, respectively, and t_r is the attenuation factor of the reference beam caused by the ND filter in Fig. 5.1.

For a thin, time-dependent TG, and assuming that the grating is a small perturbation to the refractive index, we can define a complex transfer function as [187]

$$\tau(t) = \tau_0 \left(1 + \cos(qx)(\Delta k(t) + i\Delta n(t))\right) \tag{5.8}$$

where τ_0 is the transfer factor of the sample in the absence of any excitation.

Assuming that the sample is located in the plane $z = 0$ and that the TG is the small perturbation to τ_0, we obtains the following expression for the (+1) diffraction order of the probe beam by grating excitation in the material described by transfer function in Eq. 5.8

$$E_{p,+1} = a_p \tau_0 E_{0p} (\Delta k(t) + i\Delta n(t)) \exp\left(i(k_p^2 - q^2/4)^{1/2} z + i(q/2)x - i\omega_p t + i\phi_p\right) \tag{5.9}$$

and the transmitted reference beam (zero order) is given by

$$E_{R,0} = a_p t_r \tau_0 E_{0p} \exp\left(i(k_p^2 - q^2/4)^{1/2} z + i(q/2)x - i\omega_p t + i\phi_R)\right) \tag{5.10}$$

Since the two beams are co-linear, their interference signal interference intensity is given by the square of the sum of their electric fields in Eqs. 5.10 and 5.9

$$I_s = I_{0p}A_pT_0\left(t_r^2 + (\Delta k(t)^2 + \Delta n(t)^2) + 2t_r(\Delta k(t)\cos\phi - \Delta n(t)\sin\phi)\right) \tag{5.11}$$

where I_{0p} is the intensity of the probe beam at the input of the setup, $A_p = |a_p|^2$ is the diffraction efficiency of the mask and $T_0 = |\tau_0|^2$ is the optical transmission of the sample at the probe wavelength and $\phi = \phi_p - \phi_R$.

This interference leads to heterodyning, with the term $2t_r(\Delta k(t)\cos\phi - \Delta n(t)\sin\phi)$ dominating the signal if $\Delta k(t), \Delta n(t) \ll t_r$ such that I_s becomes

$$\frac{I_{het}}{I_{0p}} = 2A_pT_0t_r(\Delta k(t)\cos\phi - \Delta n(t)\sin\phi) \tag{5.12}$$

Thus, the signal will purely be amplitude grating or the imaginary part if $\phi = 0, \pi$ and pure phase grating or real part if $\phi = \pm\pi/2$. Experimentally, the phase ϕ can be adjusted by tilting the glass window relative to the ND filter in Fig. 5.1.

5.3 Experimental System

5.3.1 Laser

Figure 5.3 shows the schematic setup of the UTG setup. The laser source is a Coherent Libra Ti:sapphire amplifier system capable of generating 0.4 mJ of energy at a repetition rate of 10 kHz as in Fig. 5.4. The pulse width is approximately 100 fs at 800 nm of wavelength. This laser uses an integrated Coherent Vitesse Ti:Sapphire seed laser mode-locked at 80 MHz and a Coherent Evolution mode-locked pump laser at 532 nm to feed a regenerative amplifier and a compact stretcher/compressor system all in one unit [188]. The output of the Libra has a $1/e^2$ beam diameter of about 8 mm.

The high energy of this beam is able to burn many objects put in the beam path, and care must be taken to attenuate the beam very early on in the setup. We

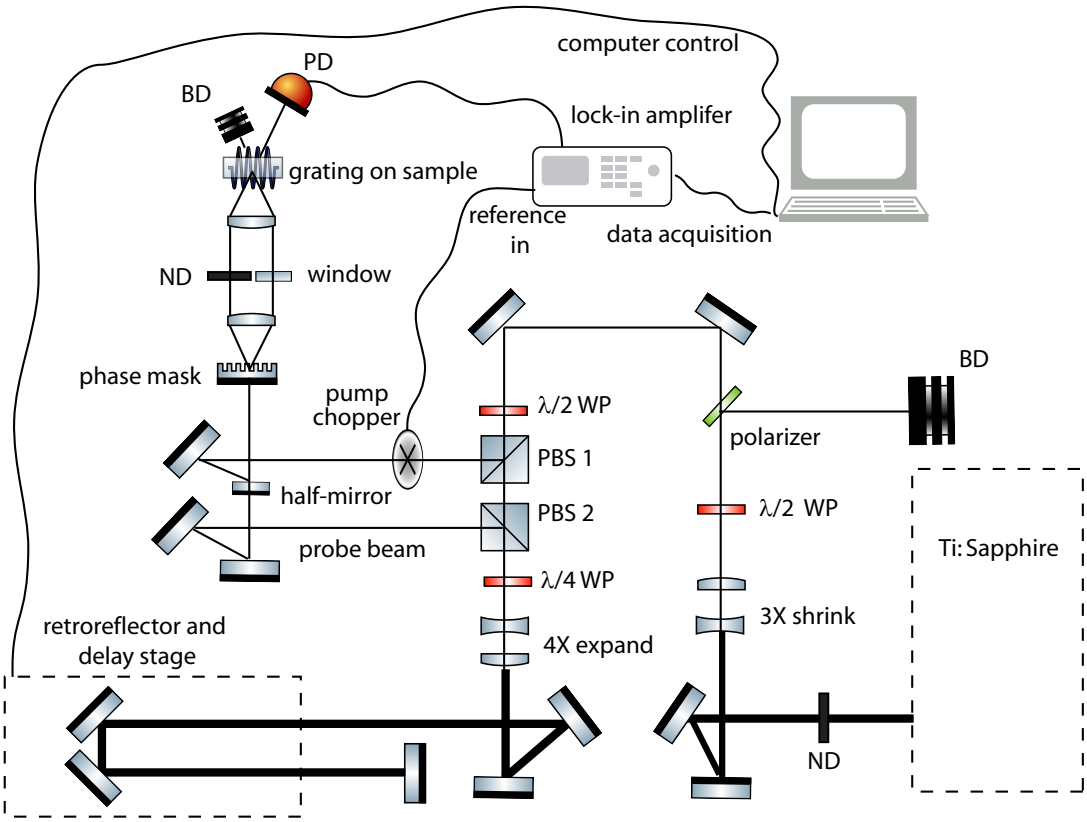

Figure 5.3: Schematic of the transient grating setup. A Ti:Sapphire amplifier generates ultra short pulses which are attenuated by neutral density (ND) filters, waveplates (WP), and polarizing beam splitters (PBS). The unwanted power is sent into a beam dump (BD) and the rest is then split into pump and probe pulses using WP and PBS. The probe pulse is delayed and then combined with the pump onto the phase mask. The phase mask diffracts both the pump and probe beams which are then combined onto the sample to form a transient grating (TG) on the sample. The grating pattern on the sample diffracts the probe beam preferentially into the photodiode if a TG is present. The signal into the photodiode (PD) is then picked up by the lock-in and acquired by the computer as a function of the probe delay. Figure made using drawings from Component library [9].

Figure 5.4: Picture of the Coherent Libra Ti:sapphire amplifier system capable of generating 0.4 mJ of energy at a repetition rate of 10 kHz at a wavelength of 800 nm.

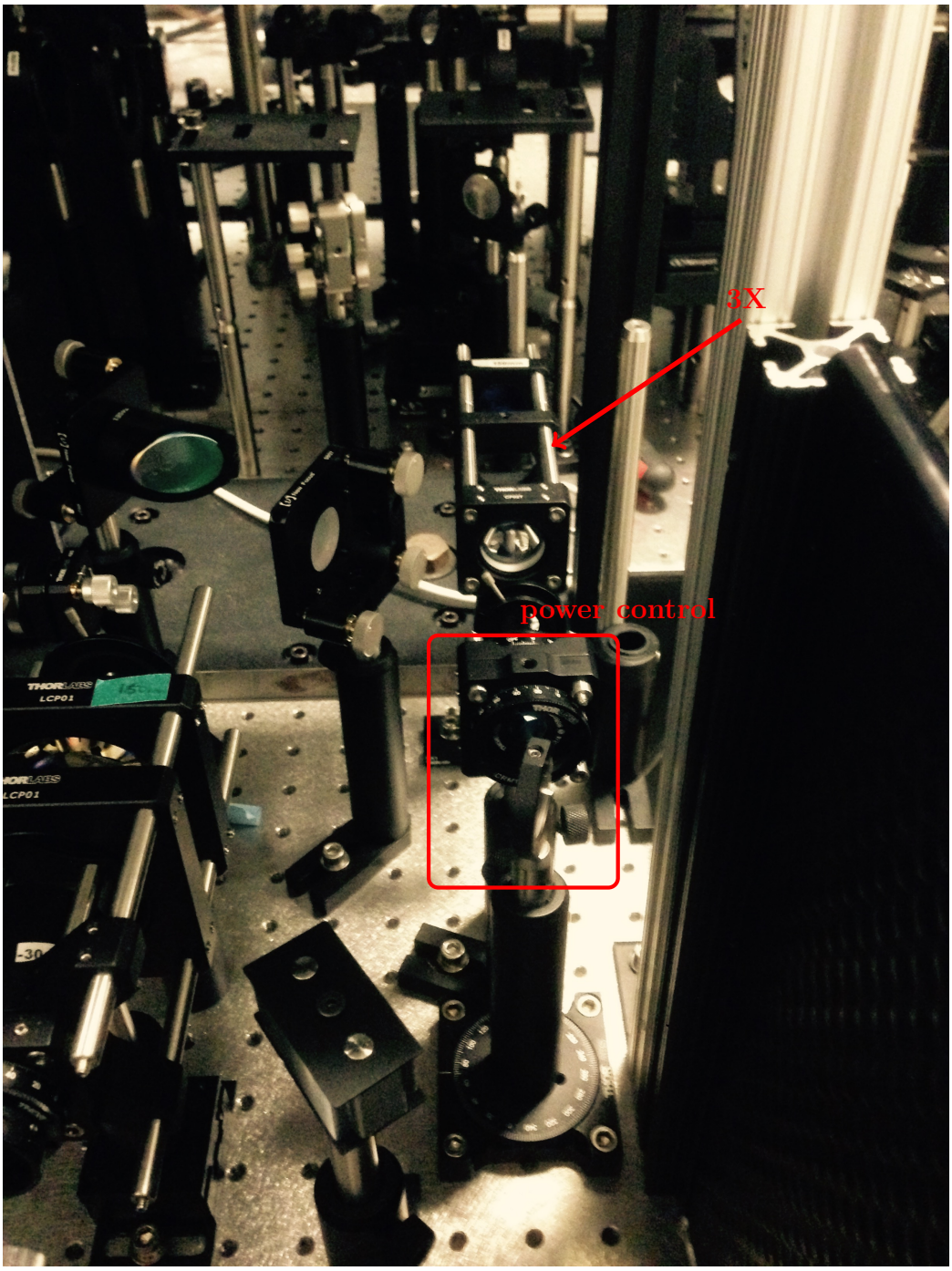

Figure 5.5: Picture of optical setup for power control. The 3X shrink telescope shown in Fig. 5.3 is also shown in this picture. The power control optics consist of a half-wave plate and a plate polarizer. The plate polarizer is used like a polarizing beam splitter with the ability to withstand high laser power.

employed attenuation at two stages of the beam path for safety and tunability of the overall power going into our setup, as shown in Fig. 5.3. First, we use a beam splitter to attenuate the laser power. The use of ND filters have led to thermal lensing effects which distorts our beam quality. However, extreme care must still be taken to dump any reflection from the reflective ND safely. In addition, we added a plate-polarizer and a half waveplate to further fine-tune the power of the incoming beam after the ND filter. The 3:1 shrink telescope ensures that the beam can passes through half-inch beam splitters and wave plates used along the beam path.

5.3.1.1 Beam path

After the polarizer in Fig. 5.3, there is a polarizing beam splitter (PBS1) and half waveplate (WP) along the path to control the relative power entering the pump and the probe paths, as shown in Fig. 5.6.

The probe enters a separate beam path which is to be mechanically delayed relative to the pump. To reduce divergence of the probe beam, there is an expanding telescope before the beam enters the delay stage as shown in Fig. 5.3 [189]. To understand why expanding a beam helps to reduce divergence, we need to understand how a perfectly collimated Gaussian beam with radius w_0 diverges. The width of a perfectly Gaussian beam diverges as

$$w = w_0\sqrt{1 + \left(\frac{\lambda z}{\pi w_0^2}\right)^2} \tag{5.13}$$

where w is the $1/e^2$ beam diameter, λ is the wavelength and z is the propagation distance [190]. Given the wavelength λ to be 800 nm and that the distance z traversed by the beam is 4 m at the maximum delay, by expanding the beam diameter from 2 mm to 8 mm we lower the divergence from 3% to 0.01%.

To create a time delay between the arrival of the probe relative to the pump pulse, we have to introduce a mechanical delay that increases the optical path of the probe relative to the pump. The mechanical delay stage in this setup is an Aerotech ACT115DL linear-servomotor-driven actuator with a resolution of 5 nm and travel range of 1000 mm. We place an aluminum retro-reflector on the delay stage and

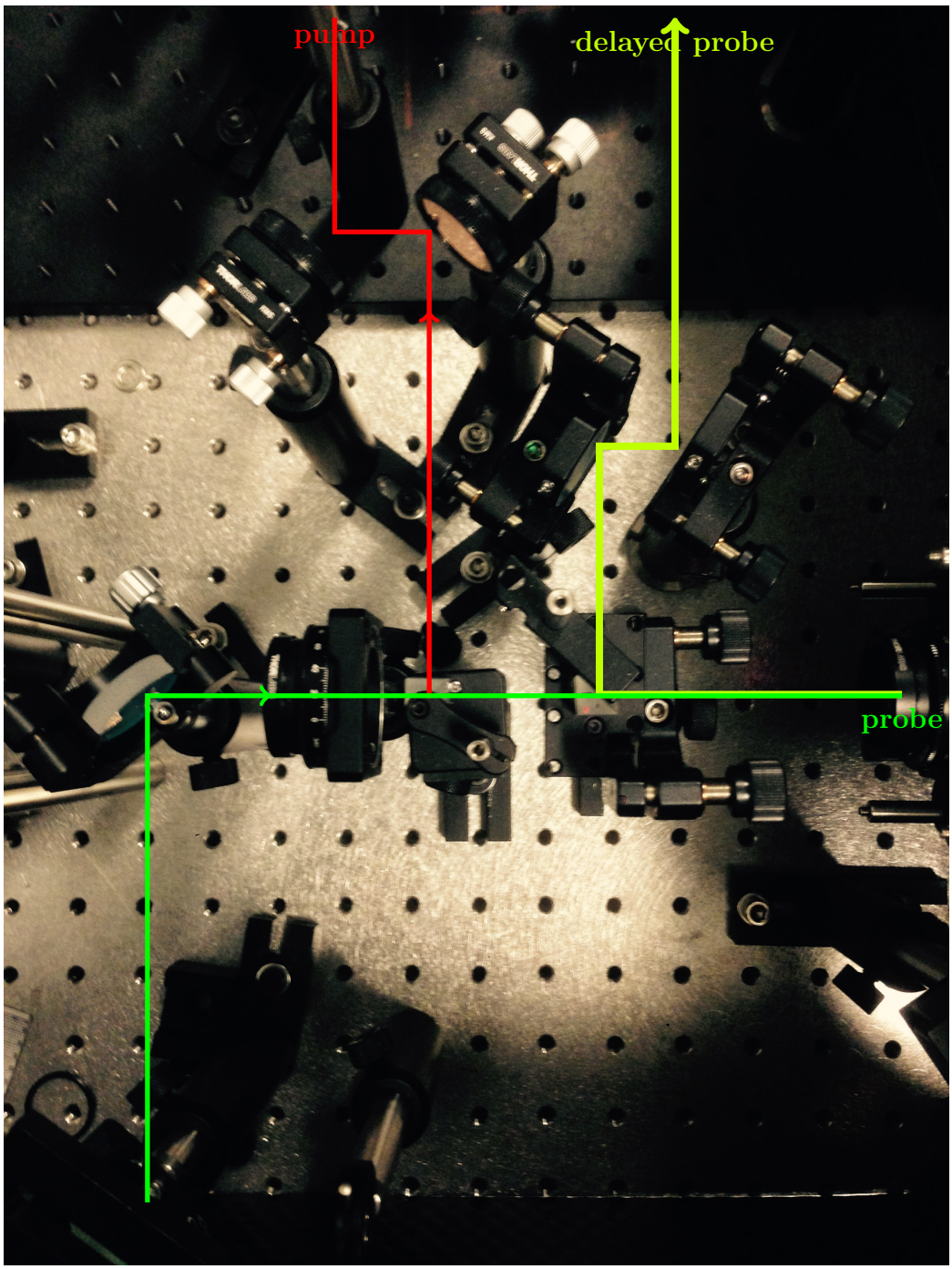

Figure 5.6: Picture of optical beam path for splitting pump and probe path. The incident beam that is reflected off from a polarizing beam splitter (PBS) after a half wave plate, is shown in red. The transmitted beam is the probe beam shown in green, which gets delayed by the mechanical delay stage. The delayed probe beam will be reflected by the PBS after passing through a quarter wave plate twice, and go to the path in lime green.

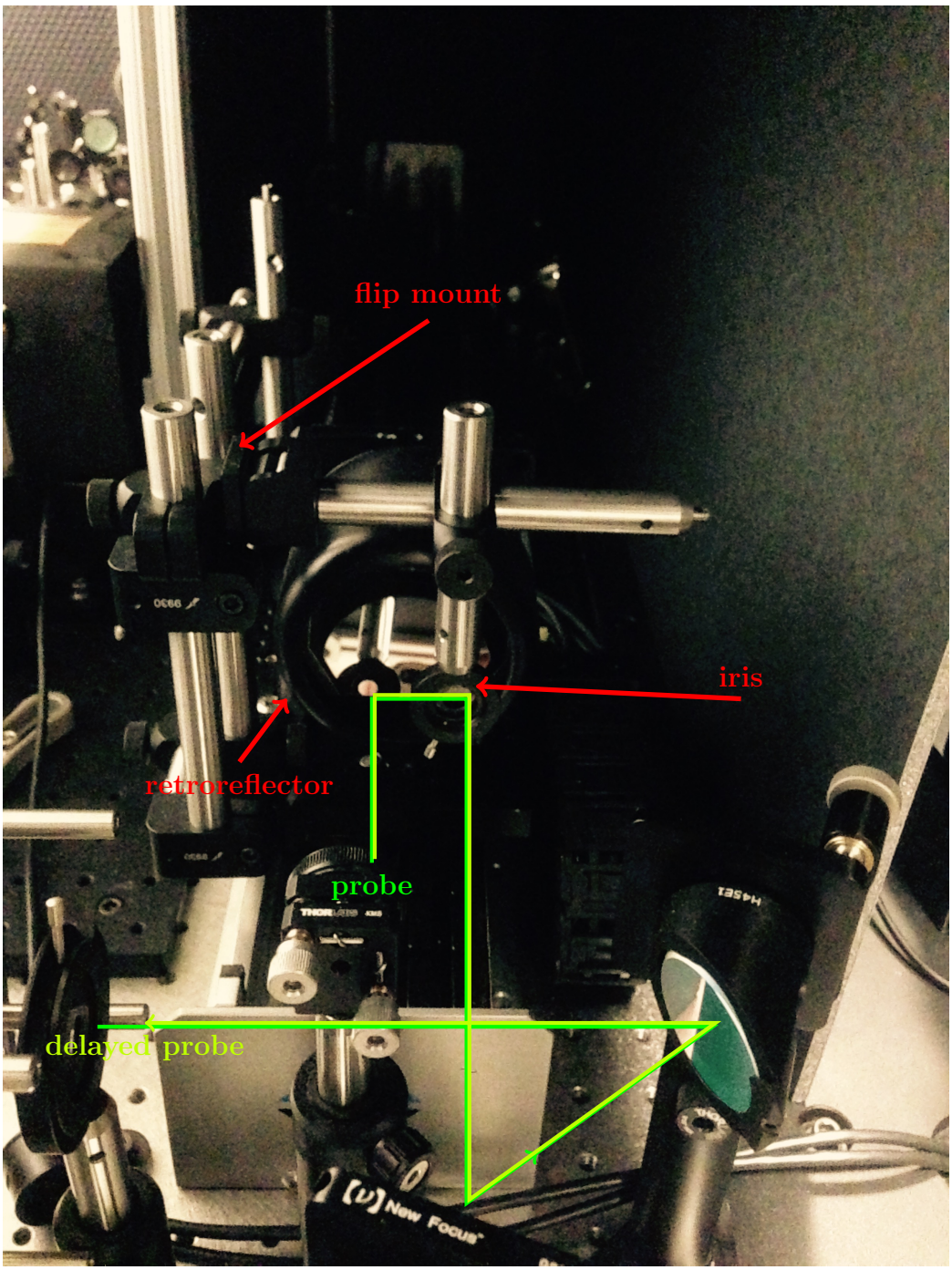

Figure 5.7: Picture of delay stage and retroreflector beam path and setup. The retroreflector mounted on the delay stage is used to reflect the probe path backwards as a delayed probe beam on the exact same path. To align the retroreflector, we use an iris mounted on a flip mount and move the delay stage back and forth while aligning onto the same iris. The whole delay stage is enclosed to minimize dust and air currents for the probe path.

double pass the beam as shown in Fig. 5.3 such that we can obtain approximately 4 m of travel delay corresponding to around 13 ns in time delay. A quarter-wave plate allows the beam to pass pick up a $\pi/2$ phase when passed through twice and be reflected at the PBS rather than being transmitted. Alignment of this long beam path is tricky and requires the use of a flip iris as in Fig. 5.7 that can indicate the beam position throughout the length of the delay.

After exiting the PBS, the probe beam is recombined with the pump beam onto the phase mask. The diameters of the pump and probe beams are measured to be approximately 600 μm and 300 μm respectively. The phase mask consists of lithographically patterned diffraction grating which is optimized to diffract most of the power to the first order. Phase masks of different spacing are patterned on a same wafer and allows easy change of beam configuration by simply translating the mask to another point. We bought phase masks from DigitalOptics. A half-mirror used for the pump beam allows the probe beam to combine without being clipped. Upon diffracting off the phase mask, the first orders are being collected by two achromatic doublets. The achromatic doublets are Thorlabs AC508-150-B and AC508-075-B at 150 mm and 75 mm, respectively, to make a 2:1 demagnification for the TG.

From Section 5.2.3, heterodyning requires us to place the ND and the compensating glass window on the probe paths. Fig. 5.1 shows that the pump and the probe paths are not actually at the same height. This is done for two reasons. One is to ensure that we can place the ND and the window just for the probe and not for the pump. Second, we can spatially separate the pump from the probe during detection which is important for preventing pump scattering into the detector.

Figure 5.8 shows the top view of the beam path of the demagnification setup. After the second achromat, the grating is formed on the sample and the probe is diffracted and heterodyned according to Eq. 5.12. The probe is then sent to the detector, which is connected to the lock-in amplifer.

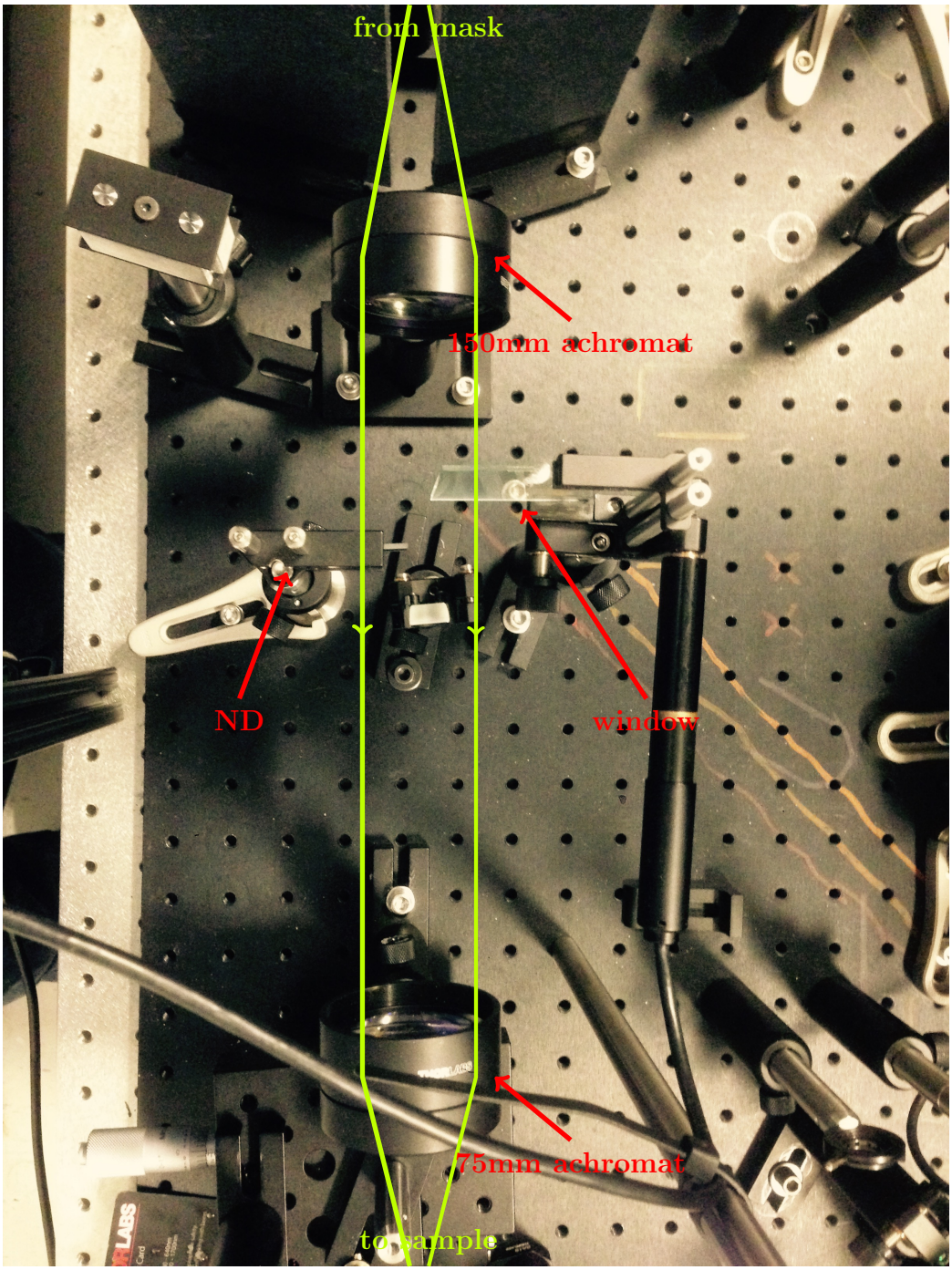

Figure 5.8: Picture of the demagnification setup to focus the pump and probe beam paths onto the sample. The relative phase of the window relative to the ND filter can be changed to allow for heterodyne detection.

5.4 Electronic System

5.4.1 Modulation and Detection

Modulating the pump using a mechanical chopper wheel in Fig. 5.3 adds a reference frequency upon which we can retrieve our signal by demodulating at the reference. This is done using the lock-in amplifier. In this setup, we use a standard Thorlabs chopper wheel (MC2000) externally synced to the 10 kHz of the laser repetition rate. The chopper then outputs a reference which is fed into the Stanford Research 830 lock-in amplifier as the reference frequency.

In Fig. 5.9, the detector is a bare Hamamatsu diode S1087. This diode is chosen due to its low dark current. Contrary to conventional wisdom that we should run the diode at reverse bias to maximize its bandwidth for ultrafast detection, here we are using a lock-in technique that is only sensitive to the reference frequency. Thus, we actually would like to restrict the bandwidth of detection to the range of the reference frequency at which the chopper is being modulated. Due to the low frequency of this detection around 1-5 kHz, we are very sensitive to $1/f$ electronic noise. Therefore, we do not have any amplifier or additional electronics before the lock-in but just place a load to terminate the photodiode at the lock-in. The cut-off frequency of detection is given by $f_c = 1/(2\pi R_L C)$ where R_L is the termination load and the C is the combined parasitic capacitance of the diode and the connections to the lock-in. Experimentally, we found $R_L = 50$ kΩ to be the best. The lock-in is connected to the computer using RS232-USB connection and data is acquired using Labview VISA interface.

5.4.2 Pump scatter

Initially, we encountered huge noise in our signal. Fig. 5.10(a) shows a plot of signal of TG from silicon membrane at a particular delay time. We can see that there is a large fluctuation about the average value. When we overlay the observed deviation change in our pump beam, they correlate well with the changes in the signal from the probe. This correlation is evident from the cross-correlation plot between the two

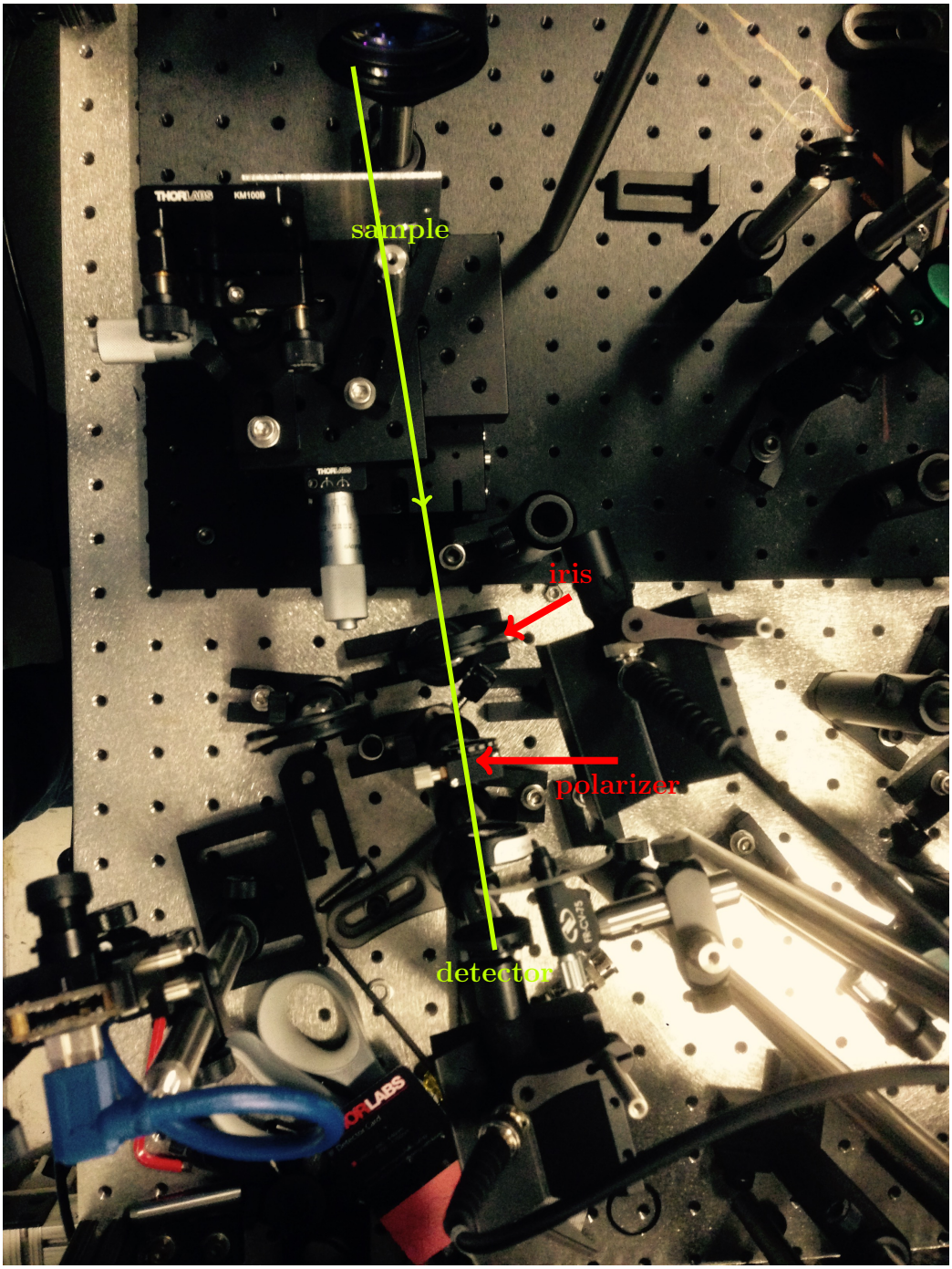

Figure 5.9: The reference beam passes through the sample onto the detector. Irises and polarizers are used to reduce pump scatter and improve the signal to noise ratio.

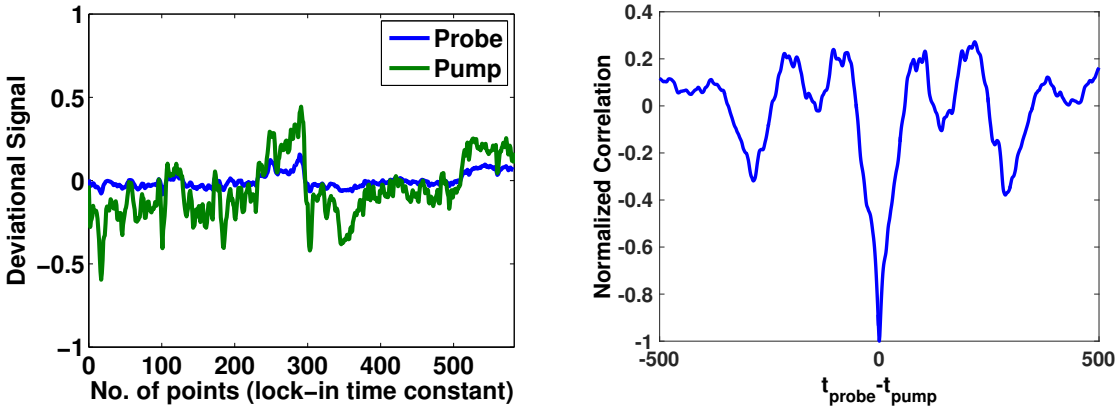

(a) (b)

Figure 5.10: (a) Lock-in voltage fluctuations of the UTG signal due to the presence of the pump scatter. A separate detector monitoring the transmitted pump beam sees the fluctuations in the same manner as the probe TG signal. Both seem to correlate with each other. (b) Cross-correlation between the pump and probe signals. The largest correlation happens at a time difference (in units of lock-in time-constant) of 0 between the two signals, indicating that the two signals change in the same way with respect to each other.

signals shown in Fig. 5.10(b).

To reduce the noise, we initially added a polarizer before the detector and set the probe to be perpendicular to the pump as shown in Fig. 5.9. This helped to reduce the noise level quite significantly.

5.5 Signal from Silicon Membrane

Silicon has been examined extensively for its electronic [176] and thermal properties using TG technique [43, 171]. Samples of etched Si membranes are made using a similar technique to Ref. [183] by Dr. Hang Zhang, a fellow post-doctoral scholar of the group. We first attmept to characterize our setup using Si membranes.

Fig. 5.11 shows a typical signal from Si membrane after 10 averages. The signal decays away within 2 ns. The small after pulse is due to the presence of another after pulse of the laser which has not been fixed yet. We have used a Hamamatsu Streak Camera C10910-21 as a high-speed photodiode and found the after pulse to occur at 2.8 ns along with other smaller pulses, as shown in Fig. 5.12.

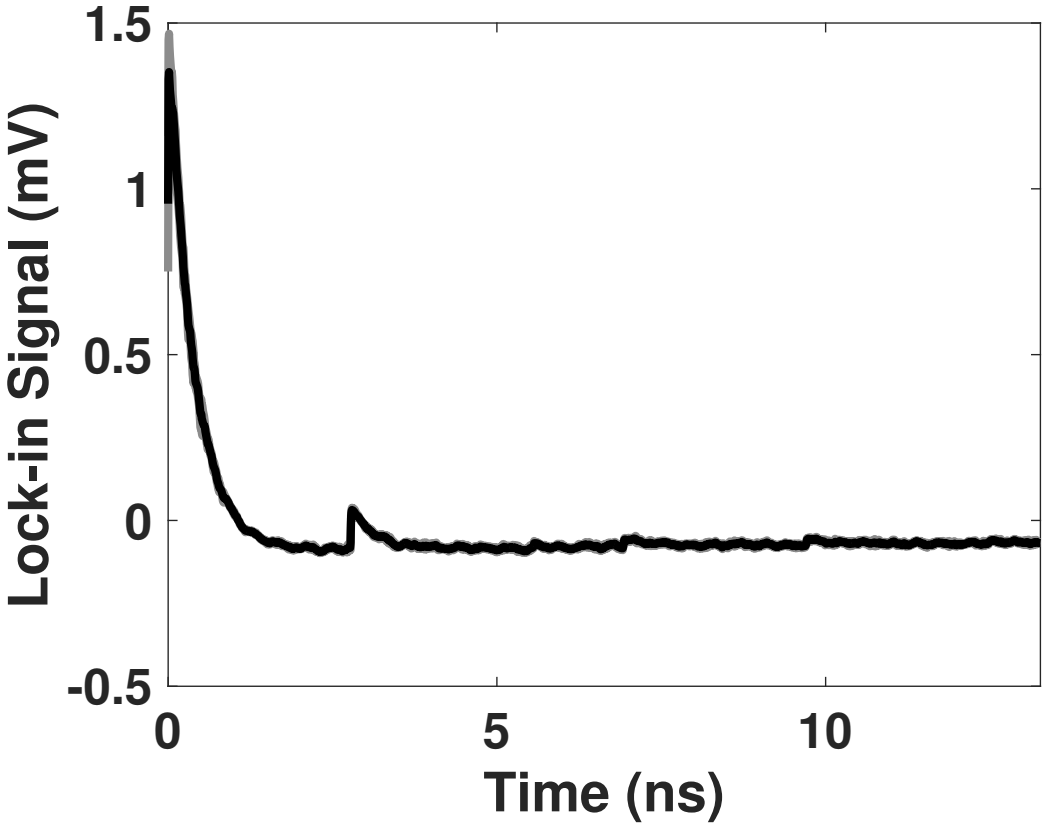

Figure 5.11: An example of a measured UTG signal of 10 averages from a 2.5 μm thick Si membrane. The grating period L on the sample is 3.5 μm. The smaller bump around 2.8 ns is caused by an after-pulse of the Libra laser system that has not been resolved yet.

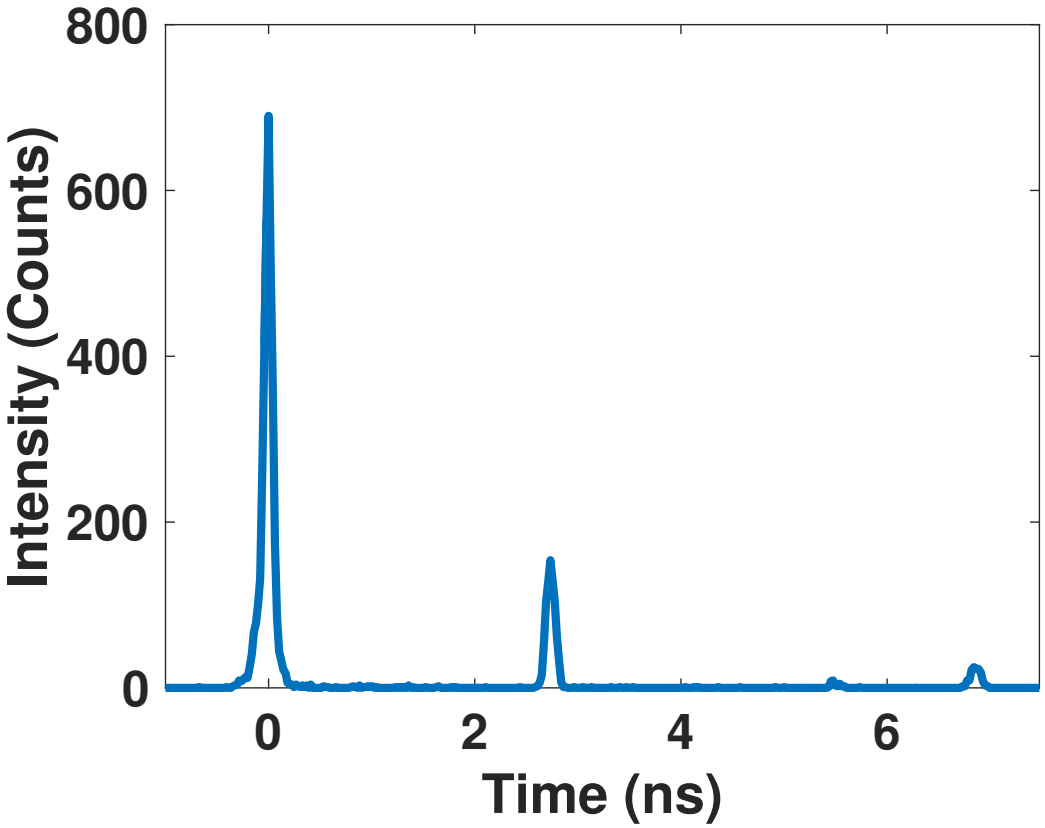

Figure 5.12: Validation of an after-pulse at 2.8 ns of delay using a Hamamatsu Universal Streak Camera Unit.

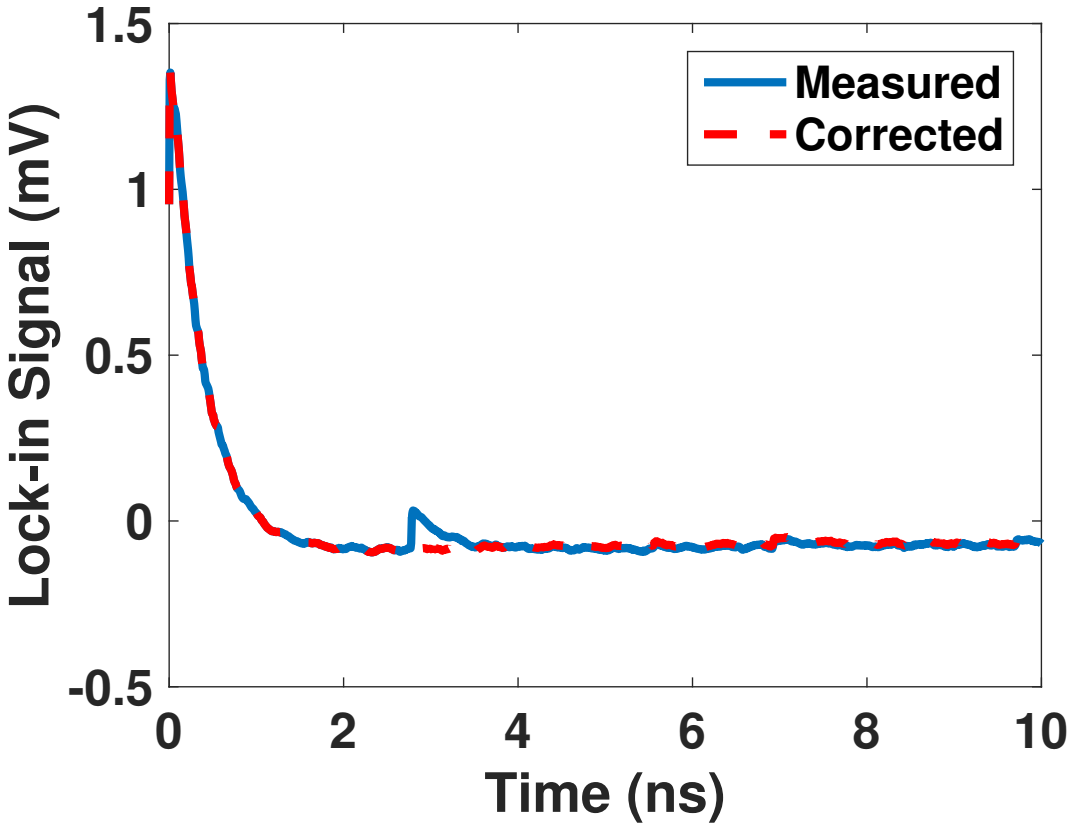

Figure 5.13: Correcting for the after-pulse by scaling the signal from $t = 0$ to $t \to 2.8$ ns and subtracting it from the data of $t > 2.8$ ns.

We adjust for the effect of the pulse by scaling the signal from $t = 0$ to $t \to 2.8$ ns and subtracting it from the data of $t > 2.8$ ns. Figure 5.13 shows the corrected signal which removes the bump caused by the after-pulse.

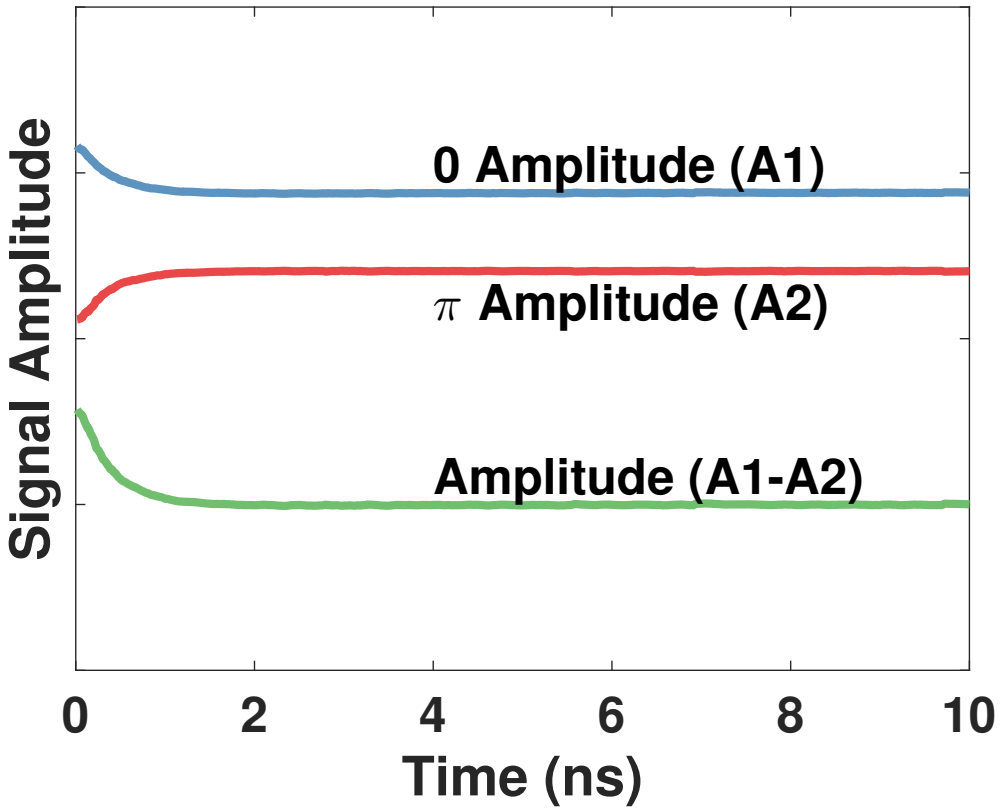

Figure 5.14: Subtracting the signal in Fig. 5.11 with its phase flipped signal by changing the tilt of the glass window relative to the ND filter in Fig. 5.1 yields the TG amplitude signal of Si membrane.

In Section 5.2.3, we discussed about how the phase of the signal can be changed from amplitude to phase grating by adjusting the phase ϕ using the tilt of the glass window relative to the ND Filter. From Eq. 5.12, we note that the signal can be flipped if the phase ϕ increase by π. The process of obtaining the amplitude (or phase) decay signal is to flip the entire signal by ϕ and subtracting them to obtain the full amplitude (or phase) signal [183]. This method also helps to get rid of any other pump-probe effects that are not sensitive to the change in phase of the probe beam. The effect of the phase adjust is shown in Fig. 5.14.

By fitting the subtracted signal in Fig. 5.14 to an exponential, we can obtain a decay time. Assuming that the grating is approximately one-dimensional the relationship of decay time τ to diffusivity α,

$$\frac{1}{\tau} = \alpha q^2 \tag{5.14}$$

where $q = \frac{2\pi}{\Lambda}$ and Λ is the grating period.

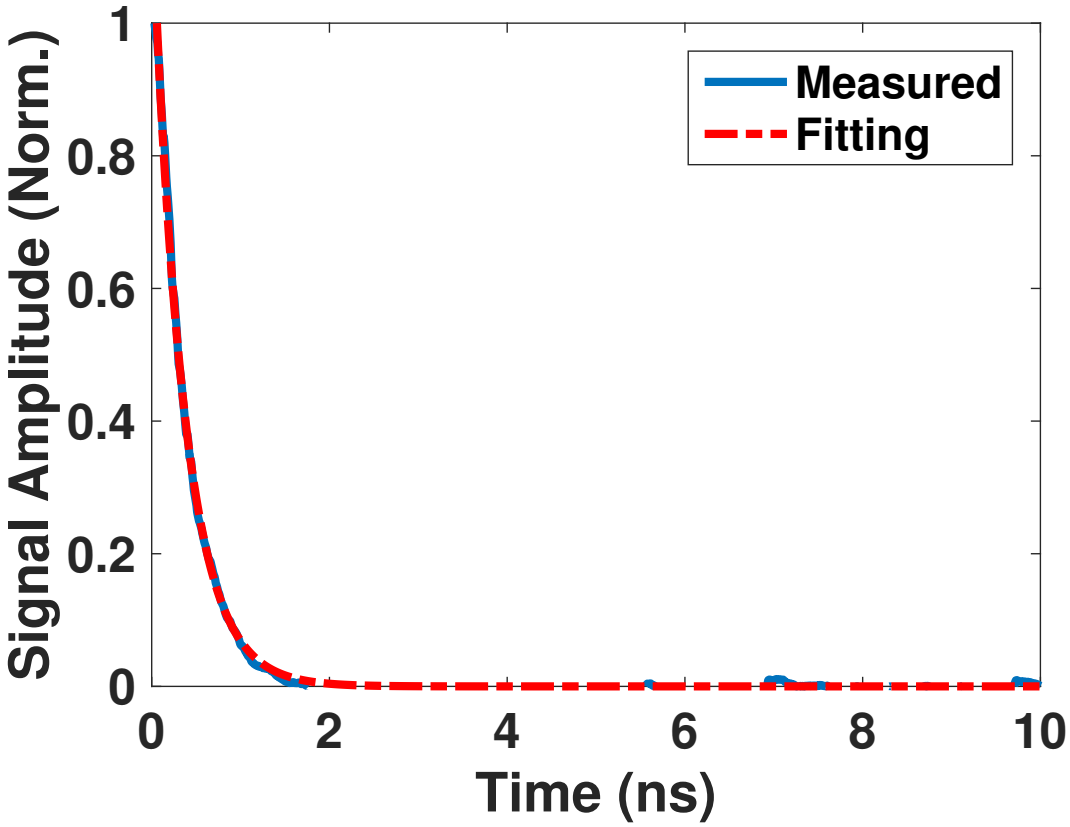

Figure 5.15: An example of a measured UTG signal from a 2.5 mum thick Si membrane. The grating period L on the sample is 3.5 μm. The smaller bump around 2.8 ns is caused by an after-pulse of the laser system that has not been fixed yet.

From the fit in Fig. 5.15, we obtain a diffusivity of 8.82 cm^2/s. This is much larger than typical thermal diffusivity of Si [43], promoting us to believe that the signal is due to changes in electronic properties of Si. There have been various early studies of photo-generated electron-hole plasma diffusion coefficient, and our measured value of diffusivity is close to the literature value of ambipolar diffusion coefficient in Si

[191–196].

To further verify that the signal indeed corresponds to ambipolar diffusion, we estimate the amount of electron-hole pairs generated from the incident photons density. In this experiment, a $\sim 1\mu$J pulse incident on the sample results in $\sim 8 \times 10^{17}$ cm^{-3} electron-holes per unit volume. This is similar to the range of electron-hole pairs generated in other works [191–196].

We were unable to obtain any thermal TG signal from the membranes unlike Ref. [43] in the current setup. We believe that this may be due to the much weaker absorption coefficient of Si at 800nm wavelength ($\sim$785 cm^{-1}) compared to 500 nm wavelength ($\sim 10^4$ cm^{-1}) in Ref. [43].

5.6 Calibration of Using Water

One way to calibrate the accuracy of the grating period on the sample is to use a test sample with a known speed of sound. Using TG technique, we can generate SAWs, which cause periodic oscillations in the TG signal. Such a technique has been used for calibration of grating periods with ethylene glycol [197]. In our case, water with dye (Epolin 2735) that absorbs around 800 nm gave us the best signal to noise, allowing for accurate calibration.

Fig. 5.16 shows the heterodyned signal after 10 averages at various grating periods. We can see that the period of the signal changes as a function of grating period. Fourier transforming the signal in Fig. 5.16 allows us to get the oscillation frequency.

If we plot the frequency at each grating period and using the linear relation between frequency and inverse of the grating period $f = v/L$, we should expect to obtain the speed of sound in water. From Fig. 5.17, we obtain the speed of sound in deionised water to be 1557 m/s, which is comparable to know values in literature (1482 m/s in Ref. [198] and 1498 m/s in Ref. [199]).

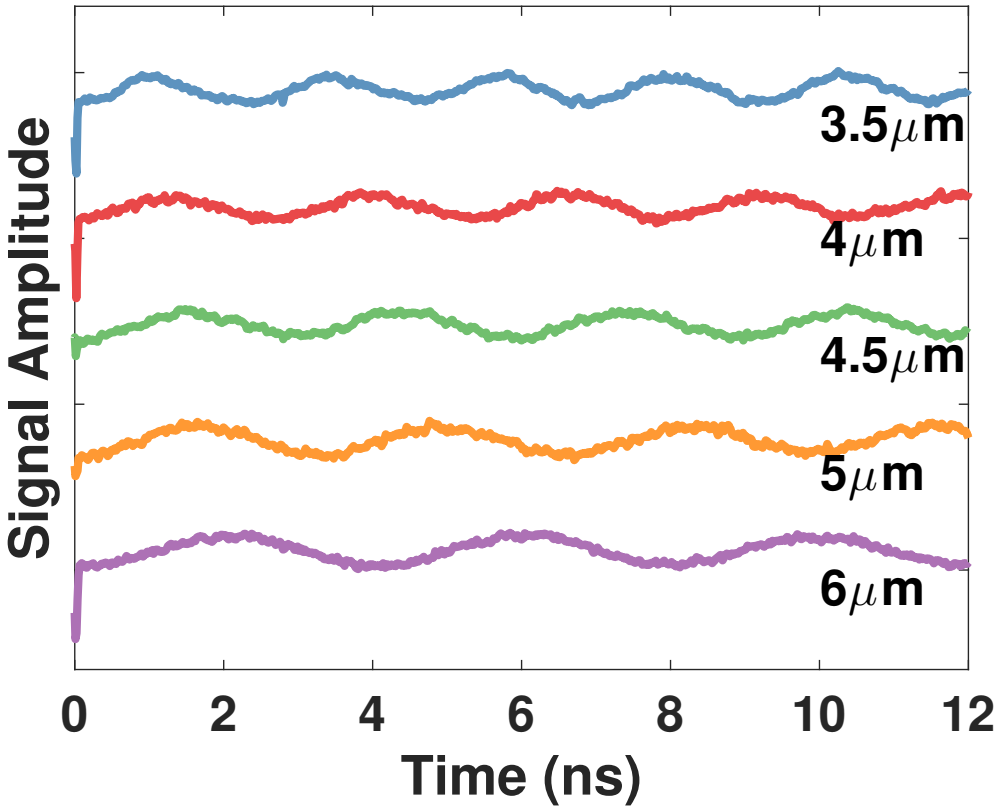

Figure 5.16: TG signal from water with dye for various grating periods. There is a fast electronic component that quickly decays away and sets off SAWs. The phase of oscillations at $t = 0$ is π, indicating that the signal is ISTS.

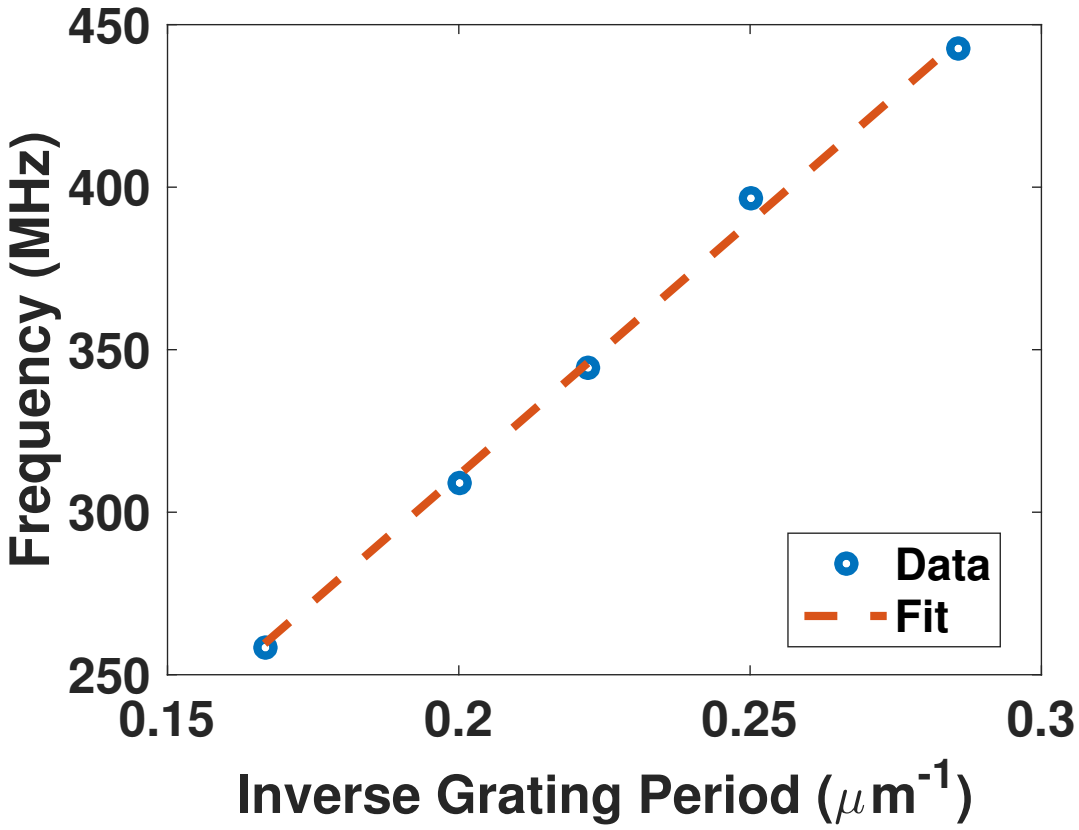

Figure 5.17: Plot of FFT peak frequency for each grating period. Speed of sound from fit is 1557 m/s.

5.7 Conclusion

We outlined the theory of TG and heterodyne detection. Then, we outlined details of how we realized an experimental setup of the UTG, including the optical and electronics. Lastly, we demonstrated the ability of the UTG using two materials, Si and water. In the following chapter, we will highlight a recent experimental characterization of the mechanical and thermal properties from suspended molybdenum disulfide (MoS_2) membranes.

Chapter 6

Measuring Mechanical and Thermal Properties of Molybdenum Disulphide

6.1 Introduction

Many two-dimensional (2D) materials, when in bulk, exist as a stack of strongly bonded layers with weak boding in between the layers. Beside the most famous graphene coming from its bulk form of graphite, there exist many other 2D materials. One important class of 2D materials is the transition metal dichalcogenides (TMDC) [200, 201], which provides a direct band gap when in their single-layer form unlike pristine graphene [202, 203]. Molybdenum disulphide (MoS_2) belongs to the class of TMDC with a high band gap and has been utilized to make electronic devices [204] and potentially as photovoltaics [205]. Knowledge of its mechanical and thermal properties are therefore important for future device applications. Mechanical properties of MoS_2 [206–212] have been studied extensively. In terms of thermal applications, MoS_2 has been shown to provide a large power factor comparable to some of the state-of-the-art commercial thermometric (TE) materials [213, 214]. The study of thermal properties of MoS_2 is important for thermal management and potential TE applications.

As mentioned in Chapter 5, a good way to characterize the elastic properties is using surface acoustic waves (SAW) generated in the transient grating technique [182].

There have been theoretical calculations of the speed of sound in MoS_2 [215–217] and experimental measurement of its longitudinal speed of phonons [218]. However, there has been no experimental measurement of the intrinsic in-plane transverse phase velocity of sound in MoS_2. The thermal conductivity of mono-layer, few layer, and bulk MoS_2 has also been measured experimentally [219–223]. However, the values vary widely from 35 W/mK to 110 W/mK. Theoretical predictions also give a very large range of values [214, 224–228].

Here, we will highlight a recent experimental characterization of the mechanical and thermal properties from suspended (MoS_2) membranes using the Ultrafast Transient Grating (UTG) described in Chapter 5. We will first show a sample signal from our measurement and describe the characteristic of the signal. Then, we go on to describe the fitting procedure and data analysis. Finally, we will describe the initially observed trend in speed of sound and thermal conductivity from our initial measurements.

6.2 Example Signal

The MoS_2 samples were obtained from our collaborator, Professor Jho of Gwangju Institute of Science and Technology (South Korea). The MoS_2 films are exfoliated and then placed onto a Si substrate. Rectangular holes of about 1-2 mm in size were already etched on the Si substrate before depositing the MoS_2. Then, the samples are secured onto the substrate using UV cured epoxy. Alpha step profile meter scanning shows the flakes to be between 4 μm to 20 μm thick. The measurement is carried out in transmission geometry as in Fig. 5.1.

Figure 6.1 shows an example of a signal from MoS_2 after 20 averages. The signal has already been processed by subtracting two phases from heterodyne detection as in Chapter 5. The signal has three distinct features. First, the signal has a large sharp rise at $t = 0$ before decaying away within 2 ns. We attribute this feature due to electronic excitation by the pump beam similar to Si membrane in Chapter 5. Second, we see an oscillating signal that also starts at $t = 0$ and persists beyond the

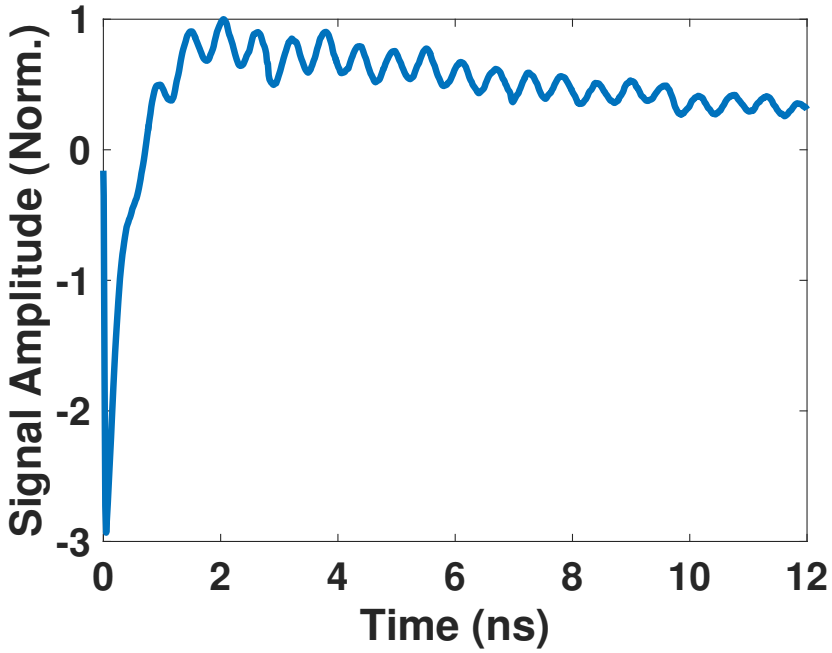

Figure 6.1: Schematic of a TG measurement on MoS_2. The grating period on the sample is 4 μm. The sharp initial rise of the signal is due to an electronic contribution with a slowly varying thermal contribution after 1 ns. The oscillations are a result of surface acoustic waves generated by thermal strain.

measurement time range of our setup. This is similar in nature to surface acoustic wave signal we observed in water in Chapter 5, albeit in a solid medium here. Third, we observe a much slower decay beyond 2 ns, which is in the opposite direction to that of the electronic excitation below 2 ns. This behavior is similar to thermal TG signal in Si membrane as of Ref. [43]. In this work, we focus our attention on the second and third feature of our signal, namely the acoustic wave and thermal component of the signal.

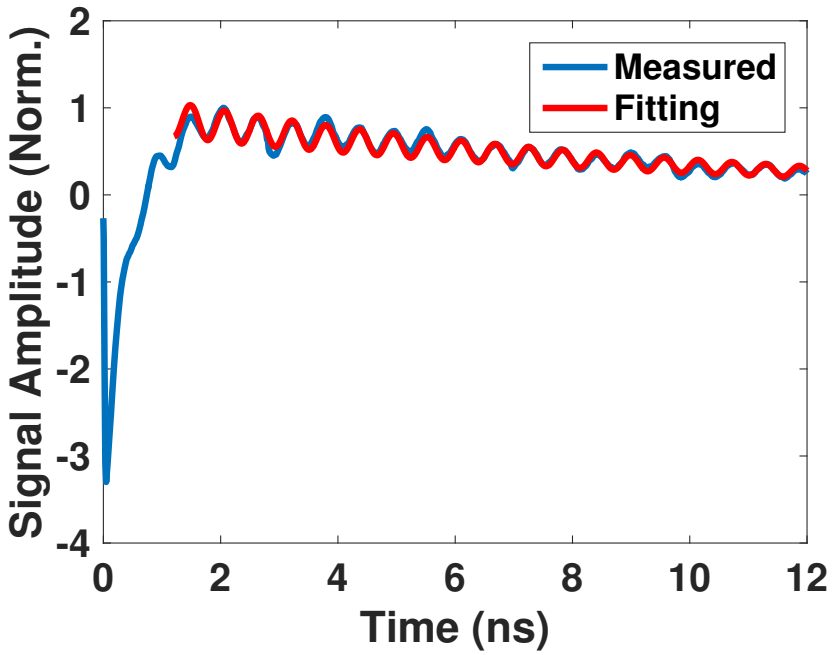

Figure 6.2: Fitting the TG signal to Eq. 6.1. The frequency of the oscillation is first obtained using Fourier Transform and then substituting into Eq. 6.1 for fitting other parameters.

We fit the signal in Fig. 6.1 using sum of an exponential decay and a sinusoidal oscillation with exponentially decaying envelope [229]. The form of the fit is

$$V(t) = A\exp(-\frac{t}{\tau_T}) + B\exp(-\frac{t}{\tau_s})\cos(2\pi\nu t + \varphi) \tag{6.1}$$

where A and B are amplitudes of the thermal and acoustic components, τ_T and τ_s are the decay time constant for the thermal and acoustic components, ν is the frequency of oscillation and φ is the initial phase of the oscillation.

Figure 6.2 shows a fit of the example signal in Fig. 6.1 using Eq. 6.1. We ignore the electronic component by only starting our fit after 2 ns. The frequency of oscillation can first be obtained from Fourier Transform and be substituted into the equation to reduce the number of fitting parameters. We use MATLAB least square fitting with Levenberg-Marquardt algorithm to fit Eq. 6.1. The fitted curve shows good agreement with the experiment data, as in Fig. 6.2

Table 6.1: Fitted values using Eq. 6.1 for the example in Fig. 6.2.

$1/\tau_T$ (GHz)	$1/\tau_s$ (GHz)	ν (GHz)	φ
0.120	0.103	1.72	0

The fitted parameters are shown in Table 6.1. First, we note the thermal decay rate $1/\tau_T$ to be 0.120 GHz. Using the relation in Eq. 5.14, we obtain the diffusivity to be 0.48 cm^2/s. Taking the volumetric specific heat of MoS_2 to be 1.89 J cm^{-3} K^{-1} [230], this corresponds to 91 W/mK for the thermal conductivity of MoS_2. From the value of the decay rate for SAW τ_s, the damping rate is $\sim$ 0.1 GHz, which corresponds to around 10 ns of decay time. We observed similar order of magnitude for SAW decay rates at other grating periods. The last term in the fit is the phase φ which is approximately 0. In Chapter 5, we discussed about the starting phase of the SAW as an indication of the nature of the TG signal as ISTS (amplitude grating) or ISBS (phase grating) [183]. When the starting phase is a multiple of π, the signal is an amplitude grating, as evident from the initial phase φ for a cosine function.

6.3 Speed of Sound

Figure 6.3 shows compiled data of MoS_2 for different grating periods, each taken with 20 averages. The frequency change with respect to the grating period is very apparent. The change in the slope of thermal decay is also noticeable. We perform numerical fitting outlined in the previous section using Eq. 6.1 for each measurement.

From a similar analysis as speed of sound calibration for water in Chapter 5, we plot the frequency of the SAW as a function of grating period for a particular

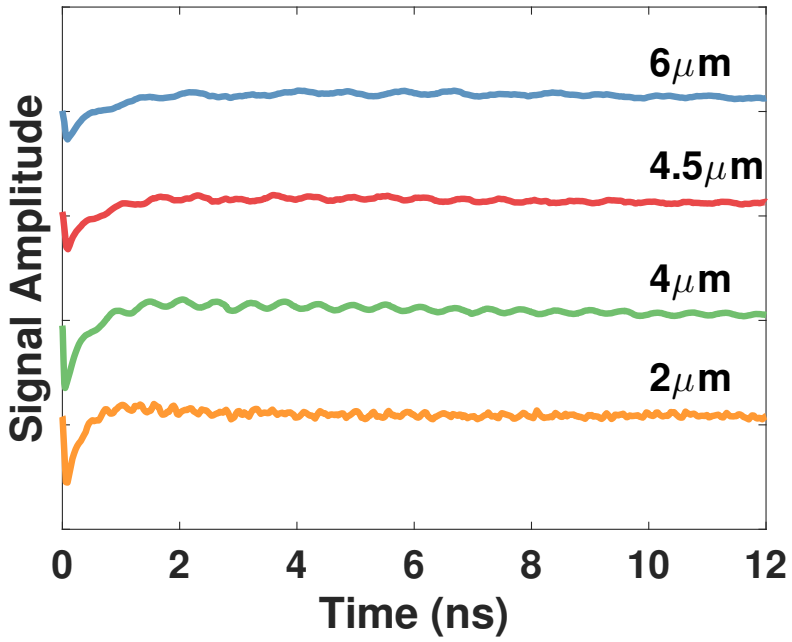

Figure 6.3: Various signals at different grating periods for a particular sample. Note the change in SAW frequency and thermal decay rate as the period is varied.

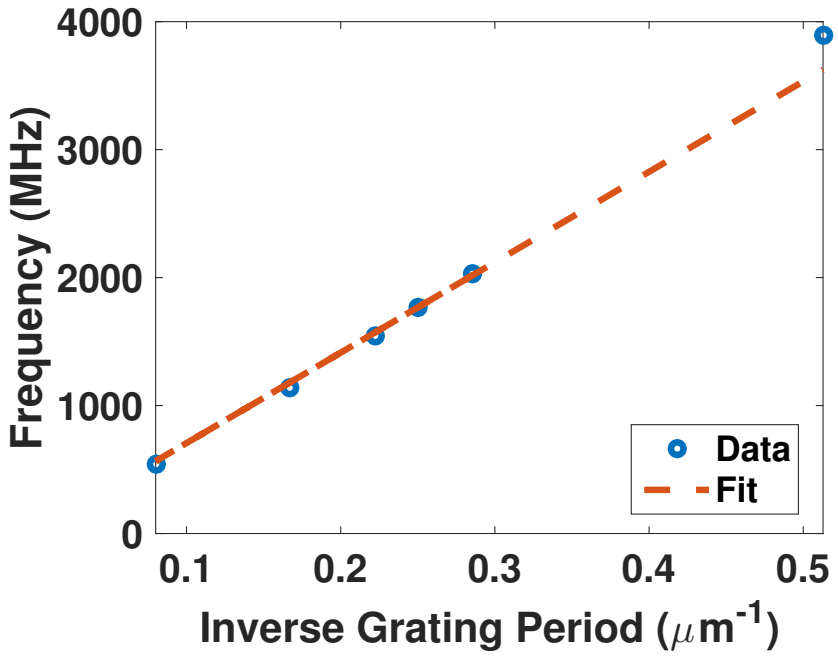

Figure 6.4: Plot of frequency of SAW for each TG period for MoS_2. The dashed line is a linear least square fit for the speed of sound, which is 7067 m/s.

sample. Figure 6.4 shows the relation between the SAW frequency as a function of grating period. We fitted the points to obtain the speed of sound as 7067 m/s. From Ref. [182], we attribute the measured speed of sound to be the intrinsic longitudinal phase velocity of sound in the film. In the low-frequency limit, the phase velocity matches the group velocity of phonons and our measured value matches well with some of the theoretical calculations for LA phonon group velocities (6700 m/s in Ref. [216] and 7930 m/s in Ref. [215]).

6.4 Thermal Conductivity of MoS_2

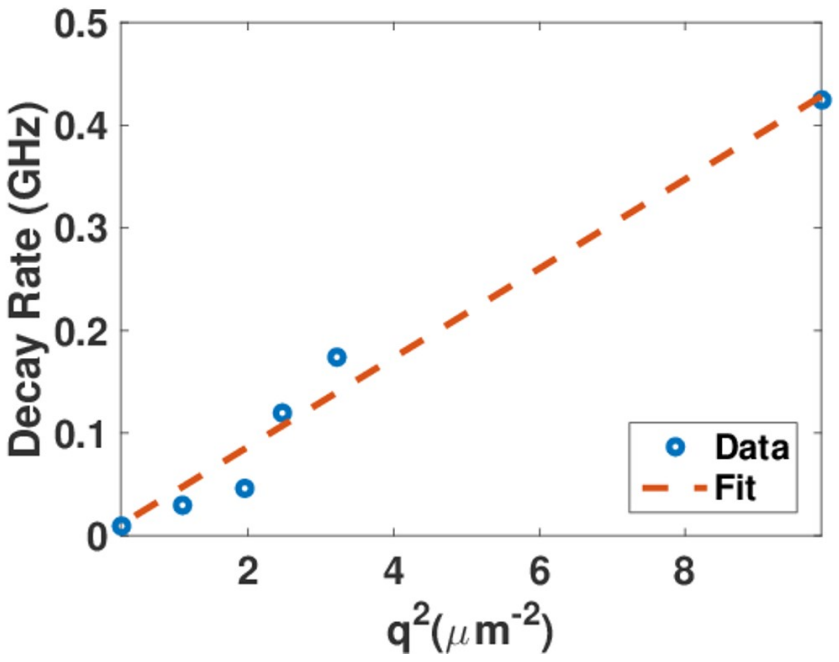

Figure 6.5: Plot of frequency of thermal decay rate $1/\tau_T$ for each TG period for MoS_2. The dashed line is a linear least square fit for the diffusivity, which is 0.43 cm^2/s.

Figure 6.5 shows the fitted thermal diffusivity fitted from experimental measurements for different grating periods. We fitted the dispersion with a linear fit and obtained a value of the thermal diffusivity from the relation in Eq. 5.14. The thermal conductivity is 82 W/mK. This value is slightly lower but much closer to the bulk value measured by Liu et al. [222] than other measurements of MoS_2 in monolayer

and thin flakes forms [219–221, 223]. Our value is also corroborated by some of the recent theory calculations [227, 228].

Also, we do not see an obvious trend of quasi-ballistic suppression in thermal conductivity from Fig. 6.5 unlike that of Si membrane in Ref. [43]. We do not believe that there will be quasiballistic effects as the MFP of MoS_2 is predicted to be <20 nm for in-plane direction [225].

6.5 Conclusion

We have described an recent experimental characterization of the mechanical and thermal properties from suspended MoS_2 membranes using UTG described in Chapter 5. We first showed a sample signal from our measurement and describe the characteristic of the signal. Then, we went on to discuss the fitting procedure and relevant fitting parameters. Finally, we discussed the initially observed speed of sound and thermal conductivity from our initial measurements. More work is needed to better understand the measured the speed of sound and confirm the measured value of thermal conductivity.

Chapters 4, 5, and 6 sum research efforts in understanding phonon transport at the nanoscale.

Chapter 7

Summary and Outlook

7.1 Overview

With advances made in this thesis and many other work, we have come to better understand and appreciate nanoscale thermal transport. For thermal conduction, phonon MFPs spectrum have now been experimentally measured in more materials [60, 172, 231]. At the same time, thermal conductivity of novel materials such as black phosphorus [232] have also been measured . Our works on understanding phonon mean free path (MFP) spectrum and measuring thermal properties of materials certainly fits well into the overall progress of the field. For thermal radiation, interest in using metamaterials [32] and resonances [233] to influence radiative thermal transport in the near-field have emergeg alongside the advances have been made to calculate [234] and measure thermal radiation [235] at even smaller separations. Once again, our interest in utilizing metamaterials to manipulate thermal radiation and in manipulating the thermal near-field is in tandem with the overall progress. In this chapter, we summarize further issues facing our work and highlight future opportunities in the fields of heat transfer by thermal photons and phonons.

7.2 Thermal Transport by Photons

Chapters 2 and 3 involves our research efforts with the photon nature of nanoscale thermal transport. Chapter 2 proposes a concept of manipulating radiative heat

transfer using hyperbolic metamaterial to create selective heat transfer. After publishing our work, we note a similar concept being proposed by Liu et al. [236] using graphene to allow selective radiative heat transfer. As discussed in Chapter 2, the need for low loss materials in the mid-infrared (MIR) can be challenging. Furthermore, cylindrically shaped layered materials with sub-wavelength thickness are in general difficult to achieve. As mentioned Chapter 2, we believe that using hexagonal boron nitride that has a natural optical anisotropy in the MIR [92] may be the a good way forward.

Chapter 3 introduces an idea of active radiative cooling using a near-field active extraction scheme. The scheme resembles laser-cooling of solids but aims to remove near-field thermal photons into the far-field rather than phonons. The project has great possibility to enable active cooling for satellite and microelectronic applications unlike conventional passive cooling techniques which is limited to the maximum possible emission from a black body. Active extraction of near-field thermal radiation has also been proposed in Ref. [237]. However, it is easy for heating of the gain medium to occur through optical pumping. We are currently working on candidate materials and system design to realize this scheme.

In the meantime, we are also working on a more generalized understanding of how active schemes couple to thermal baths. We are trying to bridge the understanding of thermodynamics of active systems [238] to how active systems respond to thermal radiation in a rate-equation-based approach. We hope to bring about a more complete understanding of how thermal radiation interacts with multi-level active medium.

Overall, utilizing interesting and novel concepts from photonics to engineer thermal radiation, such as using parity-time symmetry violation for active control of thermal radiation, can be of great potential to further develop the field of thermal radiation control.

7.3 Thermal Transport by Phonons

We have seen in Chapter 4 that we are able to use Monte-Carlo Boltzmann Transport Equation (BTE) to obtain a suppression function that predicts quasiballistic suppression in time-domain thermoreflectance (TDTR). With the advent of methods to solve BTE analytically in multi-dimensional geometries by the Minnich Group [239, 240], it is foreseeable that such a suppression function can be obtained analytically. Also, advances have been made to obtain frequency-dependent transmissivity of phonons across a aluminum silicon interface by our group [163], solving the long-standing issue of a difference in the bulk thermal conductivity between BTE and TDTR measurements as discussed in Chapter 4 and in Ref. [149]. These advances can potentially allow us to validate and further improve the suppression function by varying the spot-size in TDTR.

Chapters 5 and 6 discusses and experimental effort of setting up the ultrafast transient grating (UTG) experiment and its ability to measure surface acoustic waves (SAW) and thermal decay in molybdenum disulfide (MoS_2). In regards to the experimental setup, various technical aspects can be improved, such as suppression of pump scattering using the two-tint technique [167]. For MoS_2 measurements, more is needed to be done to corroborate the measured value of thermal conductivity and understanding elastic properties derived from the SAW signal. However, to fully utilize the potential of UTG, we should try to observe thermal signal at faster time scales. Si membrane was a candidate material for its high thermal conductivity at low temperature but we were unable to see thermal decay at room temperature as discussed in Chapter 5. Another material of interest for the group is high ordered pyrolytic graphite (HOPG), which has a very high in-plane thermal conductivity of 2000 W/mK and a strong anisotropy between the in-plane and cross-plane thermal conductivity [80, 241–244].

Overall, the progress of the field has enabled development of a good set of tools for measuring thermal conductivity and MFP spectrum and it is time for characterizing novel or nanostructured materials for their thermal properties with these techniques.

Appendix A

Derivation of Expression for Near-field Absorption

In this section, we derive the expression for the near-field absorption coefficient, given by Eq. (8) in the paper.

The absorption rate is the same as the stimulated emission rate in the absence of any degeneracy of the energy levels. The interaction with the near-field is discussed in Archambault et al. [110], where he outlines how to get the spontaneous and stimulated rates of a near-field excitation of a dipole close to the surface. We will first outline how to obtain the isotropic stimulated emission rate in Eq. (29) of [110] and then move on to show how we adopted this formulation to obtain Eq. (8) in the text.

From Eq. (C1) to (C3) of [110], the stimulated emission rate for each mode with wave vector $\mathbf{K}$ is given by

$$\gamma^{\mathbf{K}}_{stimulated} = \frac{2\pi}{\hbar}\delta(E_j - E_i - \hbar\omega)\frac{\hbar\omega n_{\mathbf{K}}}{2\epsilon_m\epsilon_0 S}|\mathbf{D_{ij}} \cdot \mathbf{u}(\mathbf{K}, z, \omega)|^2 \tag{A.1}$$

where $n_{\mathbf{K}}\hbar\omega$ is the total energy of a single mode, E_j and E_i are the excited and ground state energy levels, S is the normalization area, $\mathbf{D_{ij}}$ is the matrix element of the dipole moment operator $\hat{\mathbf{D}}_{\mathbf{ij}}$ and the vector $\mathbf{u}(\mathbf{K}, z, \omega)$ is the Fourier decomposed component of the vector potential (Eq. (3) of [110]). $\mathbf{u}(\mathbf{K}, z, \omega) = \exp(i\gamma_m z)(\hat{\mathbf{K}} - K/\gamma_m\hat{\mathbf{z}})/\sqrt{L(\omega)}$ according to Eq. (5) of [110]. The subscript p denotes the region for γ where $p = m$ for the region $z > 0$ and $p = s$ for the region inside the substrate where $z < 0$ so that $\gamma_p^2 = \epsilon_p k_0^2 - K^2$, where $k_0 = \omega/c$ and $K = |\mathbf{K}|$. $L(\omega)$ is the normalization of each

mode defined by Eq. (B5) of [110] and has the dimension of length. $\hat{\mathbf{K}}$ and $\hat{\mathbf{z}}$ are unit vectors along $\mathbf{K}$ and z axis, respectively.

Substituting Eq. (26) and Eq. (C5) of [110] into Eq. A.1

$$\begin{aligned}\gamma^{\mathbf{K}}_{stimulated} =& \frac{2\pi}{\hbar^2}\int d\omega(\hbar\delta(E_2-E_1-\hbar\omega))\frac{1}{2\epsilon_m\epsilon_0}|\mathbf{D_{ij}}\cdot\mathbf{u}(\mathbf{K},z,\omega)|^2\left\langle W(\omega)\right\rangle \\ =& \frac{2\pi}{\hbar^2}\int d\omega\delta(\omega_0-\omega)\frac{1}{2\epsilon_m\epsilon_0}|\mathbf{D_{ij}}\cdot\mathbf{u}(\mathbf{K},z,\omega)|^2\left\langle W(\omega)\right\rangle \\ =& \frac{\pi|\mathbf{D_{ij}}|^2\exp(2i\gamma_m z)}{\epsilon_m\epsilon_0\hbar^2 L(\omega_0)}\left(|\mathbf{d_{ij,\parallel}}\cdot\hat{\mathbf{K}}|^2+|d_{ij,z}\frac{K}{\gamma_m}|^2+2\mathrm{Re}(\mathbf{d_{ij,\parallel}}\cdot\hat{\mathbf{K}}d^*_{ij,z}\frac{K}{\gamma^*_m})\right)\left\langle W(\omega_0)\right\rangle\end{aligned} \tag{A.2}$$

where $\mathbf{d_{ij}}=\mathbf{D_{ij}}/|\mathbf{D_{ij}}|$ and $\langle W(\omega_0)\rangle$ is the energy density per unit surface [110].

We need to average Eq. A.2 over different orientations of $\mathbf{K}$ for different dipole orientations. Also, we need to take into account of contributions from different frequencies and wave vectors $\mathbf{K}$. First, let us consider averaging over different orientations of $\mathbf{K}$ for the case of a parallel orientation of the dipole (i.e. $d_{ij,\parallel}=1, d_{ij,z}=0$) averaged in the x-y plane.

$$\begin{aligned}&\frac{1}{4\pi^2}\int_0^{2\pi}\int_0^{2\pi}|\mathbf{d_{ij,\parallel}}\cdot\hat{\mathbf{K}}|^2+|d_{ij,z}\frac{K}{\gamma_m}|^2+2\mathrm{Re}(\mathbf{d_{ij,\parallel}}\cdot\hat{\mathbf{K}}d^*_{ij,z}\frac{K}{\gamma^*_m})d\theta d\phi \\ =&\frac{1}{4\pi^2}\int_0^{2\pi}\int_0^{2\pi}|\cos(\theta)\cos(\phi)+\sin(\theta)\sin(\phi)|^2 d\theta d\phi=\frac{1}{2}\end{aligned} \tag{A.3}$$

Likewise, one can derive an expression averaged over different orientations of $\mathbf{K}$ for the case of perpendicular orientation of the dipole (i.e. $d_{ij,\parallel}=0, d_{ij,z}=1$).

$$\begin{aligned}&\frac{1}{2\pi}\int_0^{2\pi}|\mathbf{d_{ij,\parallel}}\cdot\hat{\mathbf{K}}|^2+|d_{ij,z}\frac{K}{\gamma_m}|^2+2\mathrm{Re}(\mathbf{d_{ij,\parallel}}\cdot\hat{\mathbf{K}}d^*_{ij,z}\frac{K}{\gamma^*_m})d\theta \\ =&\frac{1}{2\pi}\int_0^{2\pi}|\frac{K}{\sqrt{\epsilon_m(\omega)k_0^2-K^2}}|^2 d\theta \\ =&|\frac{K}{\sqrt{\epsilon_m(\omega)k_0^2-K^2}}|^2\end{aligned} \tag{A.4}$$

If we consider the case for the surface plasmon dispersion in Eq. (4) of [110] such that $\epsilon_m(\omega) = 1$, we obtain

$$\begin{aligned} &|\frac{K}{\sqrt{\epsilon_m(\omega)k_0^2 - K^2}}|^2 \\ =&|\frac{k_0^2\sqrt{\frac{\epsilon_s(\omega)}{\epsilon_s(\omega)+\epsilon_m(\omega)}}}{k_0^2\sqrt{\epsilon_m(\omega) - \frac{\epsilon_s(\omega)}{\epsilon_s(\omega)+\epsilon_m(\omega)}}}|^2 \\ =&|\frac{k_0^2\sqrt{\frac{\epsilon_s(\omega)}{\epsilon_s(\omega)+\epsilon_m(\omega)}}}{k_0^2\sqrt{\epsilon_m(\omega) - \frac{\epsilon_s(\omega)}{\epsilon_s(\omega)+\epsilon_m(\omega)}}}|^2 = |\epsilon_s(\omega)| \end{aligned} \tag{A.5}$$

In [111], two-third of the contribution to the decay rate is attributed to the parallel case and one-third to the perpendicular case for isotropic averaging. These weights can be understood intuitively as two of the axes lie in the x-y plane and one in the perpendicular direction. If we use these weights to average Eq. A.2 with results from Eq. A.3 and A.5, we get Eq. (29) of [110]

$$\gamma^{\mathbf{K}}_{stimulated} = \frac{\pi|\mathbf{D_{ij}}|^2\exp(2i\gamma_1 z)}{3\epsilon_m\epsilon_0\hbar^2 L(\omega_0)}(1-\epsilon_s(\omega_0))\left\langle W(\omega_0)\right\rangle \tag{A.6}$$

Note that Archambault et al. [110] obtained Eq. (29) by integrating over possible angles of $\hat{\mathbf{K}}$ and $\mathbf{d_{ij}}$ yields the same result as above.

For the present work, this formula has to be modified in a few aspects. Firstly, our near-field energy density from the formulation in [28,34] has a different normalization in per unit volume instead of per unit area for $\langle W(\omega_0)\rangle$ in Eq. A.2. The spectral near-field energy density defined as $I(\omega)$ is plotted in Fig. 3.2 of Chapter 3. To reconcile this difference, we combine the term $\frac{\exp(2i\gamma_1 z)}{L(\omega_0)}$ together with $\langle W(\omega_0)\rangle$ from Eq. A.2 to form $I(\omega,k) = k\left\langle W(\omega_0)\right\rangle\exp(2i\gamma_1 z)/L(\omega_0)$. Here, we define $K = k_0 k$ and decompose $I(\omega) = \int_0^\infty I(\omega,k)dk$. Secondly, we sum the decay rate over all frequencies with respect to a normalized lineshape function $g(\omega,\omega_0) = \frac{\frac{\Delta\omega}{2\pi}}{(\omega-\omega_0)^2+(\Delta\omega/2)^2}$ instead of a delta function as of Eq. A.1. Here $\Delta\omega$ is the linewidth of the transition. In our

case, Eq. A.2 becomes

$$W_{ij,near-field} = \frac{2\pi}{\hbar^2}\int d\omega g(\omega,\omega_0)\frac{1}{4\pi\epsilon_m\epsilon_0}\int k dk d\theta |\mathbf{D_{ij}}\cdot\mathbf{u}(\mathbf{K},z,\omega)|^2 \langle W(\omega)\rangle \quad \text{(A.7)}$$

Using the above results, Eqs. A.3 and A.4, for isotropic orientation of emitters, we can simplify Eq. A.7 as

$$\begin{aligned} W_{ij,near-field} &= \int d\omega g(\omega,\omega_0)\int dk \frac{\pi|\mathbf{D_{ij}}|^2\exp(2i\gamma_1 z)}{2\epsilon_m\epsilon_0 3\hbar^2 L(\omega_0)}\langle W(\omega)\rangle\, k\left(1+|\frac{k}{\sqrt{\epsilon_m(\omega)-k^2}}|^2\right) \\ &= \frac{\pi|\mathbf{D_{ij}}|^2}{6\epsilon_m\epsilon_0\hbar^2}\int_0^\infty dk\int_{-\infty}^\infty d\omega\left(1+|\frac{k}{\sqrt{\epsilon_m(|\omega|)-k^2}}|^2\right) I(|\omega|,k)g(\omega,\omega_0) \end{aligned} \quad \text{(A.8)}$$

such that we sum over contributions from all k. Note that the factor of half is to account for integration from $-\infty$ to ∞ for frequency ω. If we substitute $\gamma_{ij}^0 = \omega_0^3|\mathbf{D_{ij}}|^2/(3\pi\epsilon_m\epsilon_0\hbar c^3)$ from [110] into Eq. A.8, we obtain Eq. 3.8 in the text.

$$W_{ij,near-field} = \frac{\gamma_{ij}^0\pi^2c^3}{2\hbar\omega_0^3}\int_{-\infty}^\infty\int_0^\infty(1+|\frac{k}{\sqrt{\epsilon_{medium}-k^2}}|^2)I(|\omega|,k)g(\omega)dkd\omega \quad \text{(A.9)}$$

Bibliography

[1] D. Ding, T. Kim, and A. J. Minnich. Active Thermal Extraction and Temperature Sensing of Near-field Thermal Radiation. *Scientific Reports*, 6:32744, September 2016.

[2] Sheng Shen, Arvind Narayanaswamy, and Gang Chen. Surface Phonon Polaritons Mediated Energy Transfer between Nanoscale Gaps. *Nano Letters*, 9(8):29092913, August 2009.

[3] M. Zebarjadi, K. Esfarjani, M. S. Dresselhaus, Z. F. Ren, and G. Chen. Perspectives on thermoelectrics: from fundamentals to device applications. *Energy & Environmental Science*, 5(1):51475162, January 2012.

[4] Austin Jerome Minnich. *Exploring electron and phonon transport at the nanoscale for thermoelectric energy conversion.* Thesis, Massachusetts Institute of Technology, 2011.

[5] Andrei V. Shchegrov, Karl Joulain, Rmi Carminati, and Jean-Jacques Greffet. Near-Field Spectral Effects due to Electromagnetic Surface Excitations. *Physical Review Letters*, 85(7):15481551, August 2000.

[6] Karl Joulain, Jean-Philippe Mulet, Franois Marquier, Rmi Carminati, and Jean-Jacques Greffet. Surface electromagnetic waves thermally excited: Radiative heat transfer, coherence properties and Casimir forces revisited in the near field. *Surface Science Reports*, 57(34):59112, May 2005.

[7] Jean-Philippe M. Perraud and Nicolas G. Hadjiconstantinou. Efficient simulation of multidimensional phonon transport using energy-based variance-reduced Monte Carlo formulations. *Physical Review B*, 84(20):205331, November 2011.

[8] A. J. Minnich, J. A. Johnson, A. J. Schmidt, K. Esfarjani, M. S. Dresselhaus, K. A. Nelson, and G. Chen. Thermal Conductivity Spectroscopy Technique to Measure Phonon Mean Free Paths. *Physical Review Letters*, 107(9):095901, August 2011.

[9] Alexander Franzen. ComponentLibrary: a free vector graphics library for optics.

[10] Baoan Liu, Jiawei Shi, Kaiyang Liew, and Sheng Shen. Near-field radiative heat transfer for Si based metamaterials. *Optics Communications*, 314:5765, March 2014.

[11] J.-H. Lee, Y.-S. Kim, K. Constant, and K.-M. Ho. Woodpile Metallic Photonic Crystals Fabricated by Using Soft Lithography for Tailored Thermal Emission. *Advance Materials*, 19(6):791794, March 2007.

[12] S. E. Han and D. J. Norris. Beaming thermal emission from hot metallic bull's eyes. *Optics Express*, 18(5):48294837, March 2010.

[13] Yi Xiang Yeng, Michael Ghebrebrhan, Peter Bermel, Walker R. Chan, John D. Joannopoulos, Marin Soljači, and Ivan Celanovic. Enabling high-temperature nanophotonics for energy applications. *Proceedings of the National Academy of Sciences*, 109(7):22802285, February 2012.

[14] Xianliang Liu, Talmage Tyler, Tatiana Starr, Anthony F. Starr, Nan Marie Jokerst, and Willie J. Padilla. Taming the Blackbody with Infrared Metamaterials as Selective Thermal Emitters. *Physical Review Letters*, 107(4):045901, July 2011.

[15] Peter Bermel, Michael Ghebrebrhan, Michael Harradon, Yi X. Yeng, Ivan Celanovi, John D. Joannopoulos, and Marin Soljai. Tailoring photonic metama-

terial resonances for thermal radiation. *Nanoscale Research Letters*, 6(1):549, October 2011.

[16] N. Mattiucci, G. DAguanno, Alu A., C. Argyropoulos, J. V. Foreman, and M. J. Bloemer. Taming the thermal emissivity of metals: A metamaterial approach. *Applied Physics Letters*, 100(20):201109, 2012.

[17] Hao Wang and Liping Wang. Perfect selective metamaterial solar absorbers. *Optics Express*, 21(S6):A10781093, November 2013.

[18] D. R. Smith and D. Schurig. Electromagnetic Wave Propagation in Media with Indefinite Permittivity and Permeability Tensors. *Physical Review Letters*, 90(7):077405, February 2003.

[19] S.-A. Biehs, M. Tschikin, and P. Ben-Abdallah. Hyperbolic Metamaterials as an Analog of a Blackbody in the Near Field. *Physical Review Letters*, 109(10):104301, September 2012.

[20] Yu Guo and Zubin Jacob. Thermal hyperbolic metamaterials. *Optics Express*, 21(12):1501415019, June 2013.

[21] Baoan Liu and Sheng Shen. Broadband near-field radiative thermal emitter/absorber based on hyperbolic metamaterials: Direct numerical simulation by the Wiener chaos expansion method. *Physical Review B*, 87(11):115403, March 2013.

[22] Yu Guo, Sean Molesky, Huan Hu, Cristian L. Cortes, and Zubin Jacob. Thermal excitation of plasmons for near-field thermophotovoltaics. *Applied Physics Letters*, 105(7):073903, August 2014.

[23] E. E. Narimanov, H. Li, Yu A. Barnakov, T. U. Tumkur, and M. A. Noginov. Darker than black: radiation-absorbing metamaterial. *arXiv:1109.5469 [cond-mat, physics:physics]*, September 2011.

[24] Sean Molesky, Christopher J. Dewalt, and Zubin Jacob. High temperature epsilon-near-zero and epsilon-near-pole metamaterial emitters for thermophotovoltaics. *Optics Express*, 21(S1):A96110, January 2013.

[25] Dengxin Ji, Haomin Song, Xie Zeng, Haifeng Hu, Kai Liu, Nan Zhang, and Qiaoqiang Gan. Broadband absorption engineering of hyperbolic metafilm patterns. *Scientific Reports*, 4, March 2014.

[26] Igor Nefedov and Leonid Melnikov. Super-Planckian far-zone thermal emission from asymmetric hyperbolic metamaterials. *arXiv:1402.3507 [physics]*, February 2014.

[27] E. G. Cravalho, C. L. Tien, and R. P. Caren. Effect of Small Spacings on Radiative Transfer Between Two Dielectrics. *Journal of Heat Transfer*, 89(4):351358, November 1967.

[28] D. Polder and M. Van Hove. Theory of Radiative Heat Transfer between Closely Spaced Bodies. *Physical Review B*, 4(10):33033314, November 1971.

[29] Emmanuel Rousseau, Alessandro Siria, Guillaume Jourdan, Sebastian Volz, Fabio Comin, and Jean-Jacques Chevrier, Joand Greffet. Radiative heat transfer at the nanoscale. *Nature Photonics*, 3(9):514517, September 2009.

[30] Alejandro W. Rodriguez, Ognjen Ilic, Peter Bermel, Ivan Celanovic, John D. Joannopoulos, Solja Marin, and Steven G. Johnson. Frequency-Selective Near-Field Radiative Heat Transfer between Photonic Crystal Slabs: A Computational Approach for Arbitrary Geometries and Materials. *Physical Review Letters*, 107(11):114302, September 2011.

[31] Owen D. Miller, Steven G. Johnson, and Alejandro W. Rodriguez. Effectiveness of Thin Films in Lieu of Hyperbolic Metamaterials in the Near Field. *Physical Review Letters*, 112(15):157402, April 2014.

[32] Jiawei Shi, Baoan Liu, Pengfei Li, Li Yen Ng, and Sheng Shen. Near-Field Energy Extraction with Hyperbolic Metamaterials. *Nano Letters*, 15(2):12171221, February 2015.

[33] Jean-Jacques Greffet, Rmii Carminati, Karl Joulain, Jean-Philippe Mulet, Stphane Mainguy, and Yong Chen. Coherent emission of light by thermal sources. *Nature*, 416(6876):6164, March 2002.

[34] Jon A. Schuller, Thomas Taubner, and Mark L. Brongersma. Optical antenna thermal emitters. *Nature Photonics*, 3(11):658661, November 2009.

[35] Zongfu Yu, Nicholas P. Sergeant, Torbjrn Skauli, Gang Zhang, Hailiang Wang, and Shanhui Fan. Enhancing far-field thermal emission with thermal extraction. *Nature Communications*, 4:1730, April 2013.

[36] Constantin Simovski, Stanislav Maslovski, Igor Nefedov, Sergei Kosulnikov, Pavel Belov, and Sergei Tretyakov. Hyperlens makes thermal emission strongly super-Planckian. *Photonics and Nanostructures - Fundamentals and Applications*, 13:3141, January 2015.

[37] David G. Cahill, Wayne K. Ford, Kenneth E. Goodson, Gerald D. Mahan, Arun Majumdar, Humphrey J. Maris, Roberto Merlin, and Simon R. Phillpot. Nanoscale thermal transport. *Journal of Applied Physics*, 93(2):793818, January 2003.

[38] Christopher J. Vineis, Ali Shakouri, Arun Majumdar, and Mercouri G. Kanatzidis. Nanostructured Thermoelectrics: Big Efficiency Gains from Small Features. *Advanced Materials*, 22(36):39703980, 2010.

[39] Zhiting Tian, Sangyeop Lee, and Gang Chen. Heat Transfer in Thermoelectric Materials and Devices. *Journal of Heat Transfer*, 135(6):061605, May 2013.

[40] David G. Cahill, Paul V. Braun, Gang Chen, David R. Clarke, Shanhui Fan, Kenneth E. Goodson, Pawel Keblinski, William P. King, Gerald D. Mahan,

Arun Majumdar, Humphrey J. Maris, Simon R. Phillpot, Eric Pop, and Li Shi. Nanoscale thermal transport. II. 2003-2012. *Applied Physics Reviews*, 1(1):011305, January 2014.

[41] G. Chen. Nonlocal and Nonequilibrium Heat Conduction in the Vicinity of Nanoparticles. *Journal of Heat Transfer*, 118(3):539545, August 1996.

[42] A. Ward and D. A. Broido. Intrinsic phonon relaxation times from first-principles studies of the thermal conductivities of Si and Ge. *Physical Review B*, 81(8):085205, 2010.

[43] Jeremy A. Johnson, A. A. Maznev, John Cuffe, Jeffrey K. Eliason, Austin J. Minnich, Timothy Kehoe, Clivia M. Sotomayor Torres, Gang Chen, and Keith A. Nelson. Direct Measurement of Room-Temperature Nondiffusive Thermal Transport Over Micron Distances in a Silicon Membrane. *Physical Review Letters*, 110:025901, Jan 2013.

[44] Rama Venkatasubramanian, Edward Siivola, Thomas Colpitts, and Brooks O'Quinn. Thin-film thermoelectric devices with high room-temperature figures of merit. *Nature*, 413(6856):597602, October 2001.

[45] T. C. Harman, P. J. Taylor, M. P. Walsh, and B. E. LaForge. Quantum Dot Superlattice Thermoelectric Materials and Devices. *Science*, 297(5590):22292232, 2002.

[46] Akram I. Boukai, Yuri Bunimovich, Jamil Tahir-Kheli, Jen-Kan Yu, William A. Goddard Iii, and James R. Heath. Silicon nanowires as efficient thermoelectric materials. *Nature*, 451(7175):168171, January 2008.

[47] Bed Poudel, Qing Hao, Yi Ma, Yucheng Lan, Austin Minnich, Bo Yu, Xiao Yan, Dezhi Wang, Andrew Muto, Daryoosh Vashaee, Xiaoyuan Chen, Junming Liu, Mildred S. Dresselhaus, Gang Chen, and Zhifeng Ren. High-Thermoelectric Performance of Nanostructured Bismuth Antimony Telluride Bulk Alloys. *Science*, 320(5876):634638, May 2008.

[48] Allon I. Hochbaum, Renkun Chen, Raul Diaz Delgado, Wenjie Liang, Erik C. Garnett, Mark Najarian, Arun Majumdar, and Peidong Yang. Enhanced thermoelectric performance of rough silicon nanowires. *Nature*, 451(7175):163167, January 2008.

[49] Giri Joshi, Hohyun Lee, Yucheng Lan, Xiaowei Wang, Gaohua Zhu, Dezhi Wang, Ryan W. Gould, Diana C. Cuff, Ming Y. Tang, Mildred S. Dresselhaus, Gang Chen, and Zhifeng Ren. Enhanced Thermoelectric Figure-of-Merit in Nanostructured p-type Silicon Germanium Bulk Alloys. *Nano Letters*, 8(12):46704674, 2008.

[50] Yi Ma, Qing Hao, Bed Poudel, Yucheng Lan, Bo Yu, Dezhi Wang, Gang Chen, and Zhifeng Ren. Enhanced Thermoelectric Figure-of-Merit in p-Type Nanostructured Bismuth Antimony Tellurium Alloys Made from Elemental Chunks. *Nano Letters*, 8(8):25802584, 2008.

[51] G. Pernot, M. Stoffel, I. Savic, F. Pezzoli, P. Chen, G. Savelli, A. Jacquot, J. Schumann, U. Denker, I. Monch, Ch Deneke, O. G. Schmidt, J. M. Rampnoux, S. Wang, M. Plissonnier, A. Rastelli, S. Dilhaire, and N. Mingo. Precise control of thermal conductivity at the nanoscale through individual phonon-scattering barriers. *Nature Materials*, 9(6):491495, June 2010.

[52] Rutvik J. Mehta, Yanliang Zhang, Chinnathambi Karthik, Binay Singh, Richard W. Siegel, Theodorian Borca-Tasciuc, and Ganpati Ramanath. A new class of doped nanobulk high-figure-of-merit thermoelectrics by scalable bottom-up assembly. *Nature Materials*, 11(3):233240, March 2012.

[53] Kanishka Biswas, Jiaqing He, Ivan D. Blum, Chun-I. Wu, Timothy P. Hogan, David N. Seidman, Vinayak P. Dravid, and Mercouri G. Kanatzidis. High-performance bulk thermoelectrics with all-scale hierarchical architectures. *Nature*, 489(7416):414418, September 2012.

[54] C. Dames, B. Poudel, W. Z. Wang, J. Y. Huang, Z. F. Ren, Y. Sun, J. I. Oh, C. Opeil, M. J. Naughton, and G. Chen. Low-dimensional phonon specific heat of titanium dioxide nanotubes. *Applied Physics Letters*, 87(3):031901, July 2005.

[55] Yee Koh and David Cahill. Frequency dependence of the thermal conductivity of semiconductor alloys. *Physical Review B*, 76(7):075207, August 2007.

[56] Mark E. Siemens, Qing Li, Ronggui Yang, Keith A. Nelson, Erik H. Anderson, Margaret M. Murnane, and Henry C. Kapteyn. Quasi-ballistic thermal transport from nanoscale interfaces observed using ultrafast coherent soft X-ray beams. *Nature Materials*, 9(1):2630, January 2010.

[57] Keith T. Regner, Daniel P. Sellan, Zonghui Su, Cristina H. Amon, Alan J. H. McGaughey, and Jonathan A. Malen. Broadband phonon mean free path contributions to thermal conductivity measured using frequency domain thermoreflectance. *Nature Communications*, 4:1640, March 2013.

[58] R. B. Wilson and David G. Cahill. Anisotropic failure of Fourier theory in time-domain thermoreflectance experiments. *Nature Communications*, 5:5075, October 2014.

[59] Kathleen M. Hoogeboom-Pot, Jorge N. Hernandez-Charpak, Xiaokun Gu, Travis D. Frazer, Erik H. Anderson, Weilun Chao, Roger W. Falcone, Ronggui Yang, Margaret M. Murnane, Henry C. Kapteyn, and Damiano Nardi. A new regime of nanoscale thermal transport: Collective diffusion increases dissipation efficiency. *Proceedings of the National Academy of Sciences*, page 201503449, 2015.

[60] Yongjie Hu, Lingping Zeng, Austin J. Minnich, Mildred S. Dresselhaus, and Gang Chen. Spectral mapping of thermal conductivity through nanoscale ballistic transport. *Nature Nanotechnology*, 10(8):701706, 2015.

[61] A. J. Minnich. Determining Phonon Mean Free Paths from Observations of Quasiballistic Thermal Transport. *Physical Review Letters*, 109(20):205901, November 2012.

[62] Maria N. Luckyanova, Jeremy A. Johnson, A. A. Maznev, Jivtesh Garg, Adam Jandl, Mayank T. Bulsara, Eugene A. Fitzgerald, Keith A. Nelson, and Gang Chen. Anisotropy of the Thermal Conductivity in GaAs/AlAs Superlattices. *Nano Letters*, 2013.

[63] Felix Hofmann, Daniel R. Mason, Jeffrey K. Eliason, Alexei A. Maznev, Keith A. Nelson, and Sergei L. Dudarev. Non-Contact Measurement of Thermal Diffusivity in Ion-Implanted Nuclear Materials. *arXiv:1505.05902 [cond-mat]*, 2015.

[64] Ding Ding and Austin J Minnich. Selective radiative heating of nanostructures using hyperbolic metamaterials. *Optics Express*, 23(7):A299A308, April 2015.

[65] Achim Kittel, Wolfgang Mller-Hirsch, Jrgen Parisi, Svend-Age Biehs, Daniel Reddig, and Martin Holthaus. Near-Field Heat Transfer in a Scanning Thermal Microscope. *Physical Review Letters*, 95(22):224301, November 2005.

[66] R. S. Ottens, V. Quetschke, Stacy Wise, A. A. Alemi, R. Lundock, G. Mueller, D. H. Reitze, D. B. Tanner, and B. F. Whiting. Near-Field Radiative Heat Transfer between Macroscopic Planar Surfaces. *Physical Review Letters*, 107(1):014301, June 2011.

[67] Zubin Jacob, Leonid V. Alekseyev, and Evgenii Narimanov. Optical Hyperlens: Far-field imaging beyond the diffraction limit. *Optics Express*, 14(18):82478256, September 2006.

[68] Alessandro Salandrino and Nader Engheta. Far-field subdiffraction optical microscopy using metamaterial crystals: Theory and simulations. *Physical Review B*, 74(7):075103, August 2006.

[69] Zhaowei Liu, Hyesog Lee, Yi Xiong, Cheng Sun, and Xiang Zhang. Far-Field Optical Hyperlens Magnifying Sub-Diffraction-Limited Objects. *Science*, 315(5819):16861686, March 2007.

[70] Weng Cho Chew. *Waves and Fields in Inhomogenous Media*. John Wiley & Sons, Incorporated., 1999.

[71] V. V. Nikolaev, G. S. Sokolovskii, and M. A. Kaliteevskii. Bragg reflectors for cylindrical waves. *Semiconductors*, 33(2):147152, February 1999.

[72] J. Scheuer, William M J Green, Guy A. DeRose, and A. Yariv. InGaAsP annular Bragg lasers: theory, applications, and modal properties. *IEEE Journal of Selected Topics in Quantum Electronics*, 11(2):476484, 2005.

[73] John David Jackson. *Classical electrodynamics*. Wiley, 1999.

[74] H. C. van de Hulst. *Light Scattering by Small Particles*. Dover Publications, December 1981.

[75] Craig F. Bohren and Donald R. Huffman. *Absorption and Scattering of Light by Small Particles*. Wiley-VCH, March 1998.

[76] Michael F. Modest. *Radiative Heat Transfer, Second Edition*. Academic, March 2003.

[77] B. S. Luk'yanchuk and V. Ternovsky. Light scattering by a thin wire with a surface-plasmon resonance: Bifurcations of the Poynting vector field. *Physical Review B*, 73(23):235432, June 2006.

[78] Yaxian Ni, Lei Gao, and Cheng-Wei Qiu. Achieving Invisibility of Homogeneous Cylindrically Anisotropic Cylinders. *Plasmonics*, 5(3):251258, September 2010.

[79] Snorri Ingvarsson, Levente Klein, Yat-Yin Au, James A. Lacey, and Hendrik F. Hamann. Enhanced thermal emission from individual antenna-like nanoheaters. *Optics Express*, 15(18):1124911254, September 2007.

[80] Aaron J. Schmidt, Joshua D. Alper, Matteo Chiesa, Gang Chen, Sarit K. Das, and Kimberly Hamad-Schifferli. Probing the Gold NanorodLigandSolvent Interface by Plasmonic Absorption and Thermal Decay. *The Journal of Physical Chemistry C*, 112(35):1332013323, September 2008.

[81] Zachary J. Coppens, Wei Li, D. Greg Walker, and Jason G. Valentine. Probing and Controlling Photothermal Heat Generation in Plasmonic Nanostructures. *Nano Letters*, 13(3):10231028, March 2013.

[82] Jingyu Huang, Wei Wang, Catherine J. Murphy, and David G. Cahill. Resonant secondary light emission from plasmonic Au nanostructures at high electron temperatures created by pulsed-laser excitation. *Proceedings of the National Academy of Sciences*, page 201311477, January 2014.

[83] Joseph B. Herzog, Mark W. Knight, and Douglas Natelson. Thermoplasmonics: Quantifying Plasmonic Heating in Single Nanowires. *Nano Letters*, 14(2):499503, February 2014.

[84] Jack Ng, Huanyang Chen, and C. T. Chan. Metamaterial frequency-selective superabsorber. *Optics Letters*, 34(5):644646, March 2009.

[85] Rafif E. Hamam, Aristeidis Karalis, J. D. Joannopoulos, and Marin Soljacic. Coupled-mode theory for general free-space resonant scattering of waves. *Physical Review A*, 75(5):053801, May 2007.

[86] Zhichao Ruan and Shanhui Fan. Superscattering of Light from Subwavelength Nanostructures. *Physical Review Letters*, 105(1):013901, June 2010.

[87] Sander A. Mann and Erik C. Garnett. Extreme Light Absorption in Thin Semiconductor Films Wrapped around Metal Nanowires. *Nano Letters*, 13(7):31733178, July 2013.

[88] Omar Kidwai, Sergei V. Zhukovsky, and J. E. Sipe. Effective-medium approach to planar multilayer hyperbolic metamaterials: Strengths and limitations. *Physical Review A*, 85(5):053842, May 2012.

[89] Yu Guo, Ward Newman, Cristian L. Cortes, and Zubin Jacob. Applications of Hyperbolic Metamaterial Substrates. *Advances in OptoElectronics*, 2012, December 2012.

[90] Yiguo Chen, Yan Francescato, Joshua D. Caldwell, Vincenzo Giannini, Tobias W. W. Maβ, Orest J. Glembocki, Francisco J. Bezares, Thomas Taubner, Richard Kasica, Minghui Hong, and Stefan A. Maier. Spectral Tuning of Localized Surface Phonon Polariton Resonators for Low-Loss Mid-IR Applications. *ACS Photonics*, 1(8):718724, 2014.

[91] S. Dai, Z. Fei, Q. Ma, A. S. Rodin, M. Wagner, A. S. McLeod, M. K. Liu, W. Gannett, W. Regan, K. Watanabe, T. Taniguchi, M. Thiemens, G. Dominguez, A. H. Castro Neto, A. Zettl, F. Keilmann, P. Jarillo-Herrero, M. M. Fogler, and D. N. Basov. Tunable Phonon Polaritons in Atomically Thin van der Waals Crystals of Boron Nitride. *Science*, 343(6175):11251129, March 2014.

[92] Joshua D. Caldwell, Andrey V. Kretinin, Yiguo Chen, Vincenzo Giannini, Michael M. Fogler, Yan Francescato, Chase T. Ellis, Joseph G. Tischler, Colin R. Woods, Alexander J. Giles, Minghui Hong, Kenji Watanabe, Takashi Taniguchi, Stefan A. Maier, and Kostya S. Novoselov. Sub-diffractional volume-confined polaritons in the natural hyperbolic material hexagonal boron nitride. *Nat. Commun.*, 5, October 2014.

[93] D. Ding, T. Kim, and A. J. Minnich. Active thermal extraction of near-field thermal radiation. *Physical Review B*, 93(8):081402, February 2016.

[94] L. Buller and B. McNelis. Effects of radiation on enhanced electronic cooling. *IEEE Transactions on Components, Hybrids, and Manufacturing Technology*, 11(4):538544, December 1988.

[95] J.R. Jenness. Radiative Cooling of Satellite-Borne Electronic Components. *Proceedings of the IRE*, 48(4):641643, April 1960.

[96] Aaswath P. Raman, Marc Abou Anoma, Linxiao Zhu, Eden Rephaeli, and Shanhui Fan. Passive radiative cooling below ambient air temperature under direct sunlight. *Nature*, 515(7528):540544, November 2014.

[97] T. W. Hansch and A. L. Schawlow. Cooling of gases by laser radiation. *Optics Communications*, 13(1):6869, January 1975.

[98] William D. Phillips. Nobel Lecture: Laser cooling and trapping of neutral atoms. *Review of Modern Physics*, 70(3):721741, July 1998.

[99] Peter Pringsheim. Zwei Bemerkungen uber den Unterschied von Lumineszenz- und Temperaturstrahlung. *Zeitschrift fr Physik*, 57(11-12):739746, November 1929.

[100] Mansoor Sheik-Bahae and Richard I. Epstein. Optical refrigeration. *Nature Photonics*, 1(12):693699, December 2007.

[101] Denis V. Seletskiy, Seth D. Melgaard, Stefano Bigotta, Alberto Di Lieto, Mauro Tonelli, and Mansoor Sheik-Bahae. Laser cooling of solids to cryogenic temperatures. *Nature Photonics*, 4(3):161164, March 2010.

[102] Jun Zhang, Dehui Li, Renjie Chen, and Qihua Xiong. Laser cooling of a semiconductor by 40 kelvin. *Nature*, 493(7433):504508, January 2013.

[103] M. Sheik-Bahae and R.i. Epstein. Laser cooling of solids. *Laser & Photon. Rev.*, 3(1-2):6784, February 2009.

[104] Galina Nemova and Raman Kashyap. Laser cooling of solids. *Reports on Progress in Physics*, 73(8):086501, August 2010.

[105] Anthony E. Siegman. *Lasers*. University Science Books, Mill Valley, Calif., new edition, May 1986.

[106] T. Schweizer, B. N. Samson, J. R. Hector, W. S. Brocklesby, D. W. Hewak, and D. N. Payne. Infrared emission and ion-ion interactions in thulium- and

terbium-doped gallium lanthanum sulfide glass. *Journal of Optical Society of America B*, 16(2):308316, February 1999.

[107] Angela B Seddon, Zhuoqi Tang, David Furniss, Slawomir Sujecki, and Trevor M Benson. Progress in rare-earth-doped mid-infrared fiber lasers. *Optics Express*, 18(25):2670426719, December 2010.

[108] Hiroyuki Yayama, Shigeru Fujino, Kenji Morinaga, Hiromichi Takebe, Daniel W. Hewak, and David N. Payne. Refractive index dispersion of gallium lanthanum sulfide and oxysulfide glasses. *Journal of Non-Crystalline Solids*, 239(13):187191, October 1998.

[109] Ross Stanley. Plasmonics in the mid-infrared. *Nature Photonics*, 6(7):409411, July 2012.

[110] Alexandre Archambault, Franois Marquier, Jean-Jacques Greffet, and Christophe Arnold. Quantum theory of spontaneous and stimulated emission of surface plasmons. *Physical Review B*, 82(3):035411, July 2010.

[111] R. R. Chance, A. Prock, and R. Silbey. Molecular Fluorescence and Energy Transfer Near Interfaces. In I. Prigogine and Stuart A. Rice, editors, *Advances in Chemical Physics*, page 165. John Wiley & Sons, Inc., 1978.

[112] Amnon Yariv. *Quantum Electronics*. Wiley, New York, 3 edition edition, January 1989.

[113] K. T. Shimizu, W. K. Woo, B. R. Fisher, H. J. Eisler, and M. G. Bawendi. Surface-Enhanced Emission from Single Semiconductor Nanocrystals. *Physical Review Letters*, 89(11):117401, August 2002.

[114] Koichi Okamoto, Isamu Niki, Alexander Shvartser, Yukio Narukawa, Takashi Mukai, and Axel Scherer. Surface-plasmon-enhanced light emitters based on InGaN quantum wells. *Nature Materials*, 3(9):601605, September 2004.

[115] J. Seidel, Grafstrm S., and L. Eng. Stimulated Emission of Surface Plasmons at the Interface between a Silver Film and an Optically Pumped Dye Solution. *Physical Review Letters*, 94(17):177401, May 2005.

[116] M. A. Noginov, G. Zhu, M. Bahoura, J. Adegoke, C. E. Small, B. A. Ritzo, V. P. Drachev, and V. M. Shalaev. Enhancement of surface plasmons in an Ag aggregate by optical gain in a dielectric medium. *Optics Letters*, 31(20):3022, 2006.

[117] M. A. Noginov, G. Zhu, A. M. Belgrave, R. Bakker, V. M. Shalaev, E. E. Narimanov, S. Stout, E. Herz, T. Suteewong, and U. Wiesner. Demonstration of a spaser-based nanolaser. *Nature*, 460(7259):11101112, August 2009.

[118] E.-G. Scharmer, M. Leiss, and G. Huber. Efficient energy transfer from band excitation to Nd3+ in β-La2S3:Nd, Ce. *Journal of Physics C: Solid State Physics*, 15(5):1071, February 1982.

[119] Richard I. Epstein, Melvin I. Buchwald, Bradley C. Edwards, Timothy R. Gosnell, and Carl E. Mungan. Observation of laser-induced fluorescent cooling of a solid. *Nature*, 377(6549):500503, October 1995.

[120] C. W. Hoyt, M. Sheik-Bahae, R. I. Epstein, B. C. Edwards, and J. E. Anderson. Observation of Anti-Stokes Fluorescence Cooling in Thulium-Doped Glass. *Physical Review Letters*, 85(17):36003603, October 2000.

[121] Paden B. Roder, Bennett E. Smith, Xuezhe Zhou, Matthew J. Crane, and Peter J. Pauzauskie. Laser refrigeration of hydrothermal nanocrystals in physiological media. *PNAS*, page 201510418, November 2015.

[122] Son-Tung Ha, Chao Shen, Jun Zhang, and Qihua Xiong. Laser cooling of organicinorganic lead halide perovskites. *Nat Photon*, advance online publication, December 2015.

[123] Elika Sadi, Benjamin Samson, Lionel Aigouy, Sebastian Volz, Peter Lw, Christian Bergaud, and Michel Mortier. Scanning thermal imaging by near-field fluorescence spectroscopy. *Nanotechnology*, 20(11):115703, 2009.

[124] Fiorenzo Vetrone, Rafik Naccache, Alicia Zamarrn, Angeles Juarranz de la Fuente, Francisco Sanz-Rodrguez, Laura Martinez Maestro, Emma Martn Rodriguez, Daniel Jaque, Jos Garca Sol, and John A. Capobianco. Temperature Sensing Using Fluorescent Nanothermometers. *ACS Nano*, 4(6):32543258, June 2010.

[125] Michael T. Carlson, Aurangzeb Khan, and Hugh H. Richardson. Local Temperature Determination of Optically Excited Nanoparticles and Nanodots. *Nano Lett.*, 11(3):10611069, March 2011.

[126] Lorenz H. Fischer, Gregory S. Harms, and Otto S. Wolfbeis. Upconverting Nanoparticles for Nanoscale Thermometry. *Angew. Chem. Int. Ed.*, 50(20):45464551, May 2011.

[127] Andreas Sedlmeier, Daniela E. Achatz, Lorenz H. Fischer, Hans H. Gorris, and Otto S. Wolfbeis. Photon upconverting nanoparticles for luminescent sensing of temperature. *Nanoscale*, 4(22):70907096, October 2012.

[128] Bin Dong, Baosheng Cao, Yangyang He, Zhuang Liu, Zhipeng Li, and Zhiqing Feng. Temperature Sensing and In Vivo Imaging by Molybdenum Sensitized Visible Upconversion Luminescence of Rare-Earth Oxides. *Adv. Mater.*, 24(15):19871993, April 2012.

[129] Xiangfu Wang, Jin Zheng, Yan Xuan, and Xiaohong Yan. Optical temperature sensing of NaYbF4: Tm3+@SiO2 core-shell micro-particles induced by infrared excitation. *Opt Express*, 21(18):2159621606, September 2013.

[130] Juyao Dong and Jeffrey I. Zink. Taking the Temperature of the Interiors of Magnetically Heated Nanoparticles. *ACS Nano*, April 2014.

[131] X. L. Ruan and M. Kaviany. Advances in Laser Cooling of Solids. *Journal of Heat Transfer*, 129(1):3, 2007.

[132] Albert Einstein. Zur Quantentheorie der Strahlung. *Physikalische Zeitschrift*, 18:121128, 1917.

[133] L. A. Riseberg and H. W. Moos. Multiphonon Orbit-Lattice Relaxation of Excited States of Rare-Earth Ions in Crystals. *Physical Review*, 174(2):429438, October 1968.

[134] J. M. F. van Dijk and M. F. H. Schuurmans. On the nonradiative and radiative decay rates and a modified exponential energy gap law for 4f4f transitions in rare-earth ions. *The Journal of Chemical Physics*, 78(9):53175323, May 1983.

[135] *Novel materials for laser refrigeration*, volume 7228, 2009.

[136] P. R. N. Childs, J. R. Greenwood, and C. A. Long. Review of temperature measurement. *Review of Scientific Instruments*, 71(8):29592978, August 2000.

[137] Brent Griffith, Daniel Trler, Howdy Goudey, and Joseph P. Hornak. Infrared thermographic systems. *The Encyclopedia of Imaging Science and Technology*, 2001.

[138] Yannick De Wilde, Florian Formanek, Rmi Carminati, Boris Gralak, Paul-Arthur Lemoine, Karl Joulain, Jean-Philippe Mulet, Yong Chen, and Jean-Jacques Greffet. Thermal radiation scanning tunnelling microscopy. *Nature*, 444(7120):740743, December 2006.

[139] Andrew C. Jones and Markus B. Raschke. Thermal Infrared Near-Field Spectroscopy. *Nano Lett.*, 12(3):14751481, March 2012.

[140] Jacob B. Khurgin. Surface Plasmon-Assisted Laser Cooling of Solids. *Physical Review Letters*, 98(17):177401, April 2007.

[141] J. Cuerda, F. Rting, F. J. Garca-Vidal, and J. Bravo-Abad. Theory of lasing action in plasmonic crystals. *Physical Review B*, 91(4):041118, January 2015.

[142] Peter Bermel, Elefterios Lidorikis, Yoel Fink, and John D. Joannopoulos. Active materials embedded in photonic crystals and coupled to electromagnetic radiation. *Physical Review B*, 73(16):165125, April 2006.

[143] Sebastian Wuestner, Andreas Pusch, Kosmas L. Tsakmakidis, Joachim M. Hamm, and Ortwin Hess. Overcoming Losses with Gain in a Negative Refractive Index Metamaterial. *Physical Review Letters*, 105(12):127401, September 2010.

[144] Xingjie Ni, Satoshi Ishii, Mark D. Thoreson, Vladimir M. Shalaev, Seunghoon Han, Sangyoon Lee, and Alexander V. Kildishev. Loss-compensated and active hyperbolic metamaterials. *Optics Express*, 19(25):2524225254, December 2011.

[145] D. Ding, X. Chen, and A. J. Minnich. Radial quasiballistic transport in time-domain thermoreflectance studied using Monte Carlo simulations. *Applied Physics Letters*, 104(14):143104, April 2014.

[146] Eric Pop. Energy dissipation and transport in nanoscale devices. *Nano Research*, 3(3):147169, May 2010.

[147] G. D. Mahan and Francisco Claro. Nonlocal theory of thermal conductivity. *Physical Review B*, 38(3):19631969, July 1988.

[148] Y. Ezzahri and A. Shakouri. Ballistic and diffusive transport of energy and heat in metals. *Physical Review B*, 79(18):184303, May 2009.

[149] A. J. Minnich, G. Chen, S. Mansoor, and B. S. Yilbas. Quasiballistic heat transfer studied using the frequency-dependent Boltzmann transport equation. *Physical Review B*, 84(23):235207, December 2011.

[150] Carolina Abs da Cruz, Wu Li, Nebil A. Katcho, and Natalio Mingo. Role of phonon anharmonicity in time-domain thermoreflectance measurements. *Applied Physics Letters*, 101(8):083108, August 2012.

[151] R. B. Wilson, Joseph P. Feser, Gregory T. Hohensee, and David G. Cahill. Two-channel model for nonequilibrium thermal transport in pump-probe experiments. *Physical Review B*, 88(14):144305, October 2013.

[152] Jean-Philippe M. Perraud and Nicolas G. Hadjiconstantinou. An alternative approach to efficient simulation of micro/nanoscale phonon transport. *Applied Physics Letters*, 101(15):153114, 2012.

[153] A. Majumdar. Microscale Heat Conduction in Dielectric Thin Films. *Journal of Heat Transfer*, 115(1):716, February 1993.

[154] David G. Cahill. Analysis of heat flow in layered structures for time-domain thermoreflectance. *Review of Scientific Instruments*, 75(12):51195122, November 2004.

[155] R. B. Peterson. Direct Simulation of Phonon-Mediated Heat Transfer in a Debye Crystal. *Journal of Heat Transfer*, 116(4):815822, 1994.

[156] Sandip Mazumder and Arunava Majumdar. Monte Carlo Study of Phonon Transport in Solid Thin Films Including Dispersion and Polarization. *Journal of Heat Transfer*, 123(4):749759, 2001.

[157] David Lacroix, Karl Joulain, and Denis Lemonnier. Monte Carlo transient phonon transport in silicon and germanium at nanoscales. *Physical Review B*, 72(6):064305, 2005.

[158] Ming-Shan Jeng, David Song, Gang Chen, and Ronggui Yang. Modeling the Thermal Conductivity and Phonon Transport in Nanoparticle Composites Using Monte Carlo Simulation. *Journal of Heat Transfer*, 130(4):042410, March 2008.

[159] Qing Hao, Gang Chen, and Ming-Shan Jeng. Frequency-dependent Monte Carlo simulations of phonon transport in two-dimensional porous silicon with aligned pores. *Journal of Applied Physics*, 106(11):114321, 2009.

[160] Thomas M. M. Homolle and Nicolas G. Hadjiconstantinou. Low-variance deviational simulation Monte Carlo. *Physics of Fluids (1994-present)*, 19(4):041701, 2007.

[161] Arun Majumdar and Pramod Reddy. Role of electronphonon coupling in thermal conductance of metalnonmetal interfaces. *Applied Physics Letters*, 84(23):47684770, 2004.

[162] William H. Press, Saul A. Teukolsky, William T. Vetterling, and Brian P. Flannery. *Numerical Recipes in C (2Nd Ed.): The Art of Scientific Computing*. Cambridge University Press, 1992.

[163] Chengyun Hua, Xiangwen Chen, Navaneetha K. Ravichandran, and Austin J. Minnich. Fresnel transmission coefficients for thermal phonons at solid interfaces. *arXiv:1509.07806 [cond-mat]*, 2015.

[164] M Grant and S Boyd. CVX: Matlab Software for Disciplined Convex Programming | CVX Research, Inc., 2011.

[165] Keivan Esfarjani, Gang Chen, and Harold T. Stokes. Heat transport in silicon from first-principles calculations. *Physical Review B*, 84(8):085204, August 2011.

[166] A. V. Inyushkin, A. N. Taldenkov, A. M. Gibin, A. V. Gusev, and H.-J. Pohl. On the isotope effect in thermal conductivity of silicon. *physica status solidi (c)*, 1(11):29952998, 2004.

[167] Kwangu Kang, Yee Kan Koh, Catalin Chiritescu, Xuan Zheng, and David G. Cahill. Two-tint pump-probe measurements using a femtosecond laser oscillator and sharp-edged optical filters. *Review of Scientific Instruments*, 79(11):114901, 2008.

[168] G.m. Pharr and W.c. Oliver. Measurement of Thin Film Mechanical Properties Using Nanoindentation. *MRS Bulletin*, 17(07):2833, July 1992.

[169] Jan-ke Schweitz. Mechanical Characterization of Thin Films by Micromechanical Techniques. *MRS Bulletin*, 17(07):3445, July 1992.

[170] Richard P. Vinci and Joost J. Vlassak. Mechanical behavior of thin films. *Annual Review of Materials Science*, 26(1):431462, 1996.

[171] Markus Schmotz, Patrick Bookjans, Elke Scheer, and Paul Leiderer. Optical temperature measurements on thin freestanding silicon membranes. *Review of Scientific Instruments*, 81(11):114903, November 2010.

[172] Jeremy A. Johnson, Jeffrey K. Eliason, Alexei A. Maznev, Tengfei Luo, and Keith A. Nelson. Non-diffusive thermal transport in GaAs at micron length scales. *Journal of Applied Physics*, 118(15):155104, 2015.

[173] Aaron J. Schmidt, Matteo Chiesa, Darius H. Torchinsky, Jeremy A. Johnson, Keith A. Nelson, and Gang Chen. Thermal conductivity of nanoparticle suspensions in insulating media measured with a transient optical grating and a hotwire. *Journal of Applied Physics*, 103(8):083529, April 2008.

[174] Koichi Okamoto, Zhaoyu Zhang, Axel Scherer, and David T. Wei. Mask pattern transferred transient grating technique for molecular-dynamics study in solutions. *Applied physics letters*, 85(21):48424844, 2004.

[175] Keith A. Nelson, Roger Casalegno, R. J. Dwayne Miller, and M. D. Fayer. Lasernduced excited state and ultrasonic wave gratings: Amplitude and phase grating contributions to diffraction. *The Journal of Chemical Physics*, 77(3):11441152, August 1982.

[176] Hans Joachim Eichler, Peter Gnter, and Dieter W. Pohl. *Laser-Induced Dynamic Gratings*, volume 50 of *Springer Series in Optical Sciences*. Springer Berlin Heidelberg, Berlin, Heidelberg, 1986.

[177] John T. Fourkas and M. D. Fayer. The transient grating: a holographic window to dynamic processes. *Accounts of Chemical Research*, 25(5):227233, May 1992.

[178] Yong-Xin Yan, Edward B. Gamble Jr, and Keith A. Nelson. Impulsive stimulated scattering: General importance in femtosecond laser pulse interactions with matter, and spectroscopic applications. *The Journal of Chemical Physics*, 83(11):53915399, December 1985.

[179] J. F. Nye. *Physical Properties of Crystals: Their Representation by Tensors and Matrices*. Clarendon Press, 1985.

[180] Lev Davidovich Landau, Lifshits Evgeni Mikhalovich, Arnold Markovich Kosevich, and Lev Petrovich Pitaevski. *Theory of Elasticity*. Elsevier, 1986.

[181] J. A. Rogers, Y. Yang, and K. A. Nelson. Elastic modulus and in-plane thermal diffusivity measurements in thin polyimide films using symmetry-selective real-time impulsive stimulated thermal scattering. *Applied Physics A*, 58(5):523534, May 1994.

[182] John A. Rogers, Alex A. Maznev, Matthew J. Banet, and Keith A. Nelson. OPTICAL GENERATION AND CHARACTERIZATION OF ACOUSTIC WAVES IN THIN FILMS: Fundamentals and Applications. *Annual Review of Materials Science*, 30(1):117157, 2000.

[183] Jeremy A. (Jeremy Andrew) Johnson. *Optical characterization of complex mechanical and thermal transport properties*. Thesis, Massachusetts Institute of Technology, 2011. Thesis (Ph. D.)Massachusetts Institute of Technology, Dept. of Chemistry, 2011.

[184] Bruce J. Berne and Robert Pecora. *Dynamic Light Scattering: With Applications to Chemistry, Biology, and Physics*. Courier Corporation, 1976.

[185] A. A. Maznev, K. A. Nelson, and J. A. Rogers. Optical heterodyne detection of laser-induced gratings. *Optics Letters*, 23(16):1319, 1998.

[186] Heterodyne, 2015. Page Version ID: 695093231.

[187] Robert Jacob Collier, Christoph B. Burckhardt, and Lawrence H. Lin. *Optical holography*. Academic Press, 1971.

[188] Coherent Inc.

[189] Aaron Jerome Schmidt. *Optical characterization of thermal transport from the nanoscale to the macroscale*. Thesis, Massachusetts Institute of Technology, 2008. Thesis (Ph. D.)Massachusetts Institute of Technology, Dept. of Mechanical Engineering, 2008.

[190] E. Hecht. *Optics*. Addison-Wesley, 4 edition edition, 2001.

[191] J. P. Woerdman. *Some Optical and Electrical Properties of a Laser-generated Free-carrier Plasma in Si*. N.V. Philips' Gloeilampenfabrieken, 1971.

[192] K. Jarainas and J. Vaitkus. Investigation of non-equilibrium processes in semiconductors by the method of transient holograms. *Physica Status Solidi (a)*, 44(2):793800, December 1977.

[193] E. Gaubas, K. Jarainas, and J. Vaitkus. Light Induced Transient Grating Decay in Si and Some AIIBIV Compounds. *Physica Status Solidi (a)*, 69(1):K87K90, 1982.

[194] Jan Linnros and Vytautas Grivickas. Carrier-diffusion measurements in silicon with a Fourier-transient-grating method. *Physical Review B*, 50(23):1694316955, 1994.

[195] Chun-Mao Li, Theodore Sjodin, and Hai-Lung Dai. Photoexcited carrier diffusion near a Si(111) surface: Non-negligible consequence of carrier-carrier scattering. *Physical Review B*, 56(23):1525215255, 1997.

[196] Xiren Zhang, Bincheng Li, and Chunming Gao. Electronic transport characterization of silicon wafers by laterally resolved free-carrier absorption and multiparameter fitting. *Applied Physics Letters*, 89(11):112120, 2006.

[197] Scott Silence. Time-Resolved Light Scattering Studies of Structural Rearrangements in Disordered Condensed Phase Systems. *Ph.D. Thesis*, 1991.

[198] John D. Cutnell and Kenneth W. Johnson. *Physics*. Wiley, 1997.

[199] David R Lide and W. M. Mickey. *Handbook of chemistry and physics: a ready-reference book of chemical and physical data.* Boca Raton:. CRC,, 2009.

[200] L. F. Mattheiss. Band Structures of Transition-Metal-Dichalcogenide Layer Compounds. *Physical Review B*, 8(8):37193740, October 1973.

[201] J. A. Wilson and A. D. Yoffe. The transition metal dichalcogenides discussion and interpretation of the observed optical, electrical and structural properties. *Advances in Physics*, 18(73):193335, 1969.

[202] Nasim Alem, Rolf Erni, Christian Kisielowski, Marta D. Rossell, Will Gannett, and A. Zettl. Atomically thin hexagonal boron nitride probed by ultrahigh-resolution transmission electron microscopy. *Physical Review B*, 80(15):155425, 2009.

[203] Qing Hua Wang, Kourosh Kalantar-Zadeh, Andras Kis, Jonathan N. Coleman, and Michael S. Strano. Electronics and optoelectronics of two-dimensional transition metal dichalcogenides. *Nature Nanotechnology*, 7(11):699712, 2012.

[204] B. Radisavljevic, A. Radenovic, J. Brivio, V. Giacometti, and A. Kis. Single-layer MoS2 transistors. *Nature Nanotechnology*, 6(3):147150, 2011.

[205] Marco Bernardi, Maurizia Palummo, and Jeffrey C. Grossman. Extraordinary Sunlight Absorption and One Nanometer Thick Photovoltaics Using Two-Dimensional Monolayer Materials. *Nano Letters*, 13(8):36643670, 2013.

[206] Simone Bertolazzi, Jacopo Brivio, and Andras Kis. Stretching and Breaking of Ultrathin MoS2. *ACS Nano*, 5(12):97039709, 2011.

[207] Won Seok Yun, S. W. Han, Soon Cheol Hong, In Gee Kim, and J. D. Lee. Thickness and strain effects on electronic structures of transition metal dichalcogenides: 2H-$M{X}_{2}$ semiconductors (M $=$ Mo, W; X $=$ S, Se, Te). *Physical Review B*, 85(3):033305, 2012.

[208] H. Peelaers and C. G. Van de Walle. Effects of strain on band structure and effective masses in MoS${}_{2}$. *Physical Review B*, 86(24):241401, 2012.

[209] Yeung Yu Hui, Xiaofei Liu, Wenjing Jie, Ngai Yui Chan, Jianhua Hao, Yu-Te Hsu, Lain-Jong Li, Wanlin Guo, and Shu Ping Lau. Exceptional Tunability of Band Energy in a Compressively Strained Trilayer MoS2 Sheet. *ACS Nano*, 7(8):71267131, 2013.

[210] Andres Castellanos-Gomez, Rafael Roldn, Emmanuele Cappelluti, Michele Buscema, Francisco Guinea, Herre S. J. van der Zant, and Gary A. Steele. Local Strain Engineering in Atomically Thin MoS2. *Nano Letters*, 13(11):53615366, 2013.

[211] J. L. Feldman. Elastic constants of 2H-MoS2 and 2H-NbSe2 extracted from measured dispersion curves and linear compressibilities. *Journal of Physics and Chemistry of Solids*, 37(12):11411144, 1976.

[212] H. Peelaers and C. G. Van de Walle. Elastic Constants and Pressure-Induced Effects in MoS $_2$. *The Journal of Physical Chemistry C*, 118(22):1207312076, 2014.

[213] Morteza Kayyalha, Li Shi, and Yong P. Chen. Gate-Tunable and Thickness-dependent Electronic and Thermoelectric Transport in few-layer MoS2. *arXiv:1505.05891 [cond-mat]*, 2015.

[214] Zelin Jin, Quanwen Liao, Haisheng Fang, Zhichun Liu, Wei Liu, Zhidong Ding, Tengfei Luo, and Nuo Yang. A Revisit to High Thermoelectric Performance of Single-layer MoS2. *arXiv preprint arXiv:1504.03852*, 2015.

[215] Wenxu Zhang, Zhishuo Huang, Wanli Zhang, and Yanrong Li. Two-dimensional semiconductors with possible high room temperature mobility. *Nano Research*, 7(12):17311737, 2014.

[216] Kristen Kaasbjerg, Kristian S. Thygesen, and Karsten W. Jacobsen. First-principles study of the phonon-limited mobility in n-type single-layer MoS2. *arXiv preprint arXiv:1201.5284*, 2012.

[217] Yingchun Ding and Bing Xiao. Thermal expansion tensors, Grneisen parameters and phonon velocities of bulk MT2 (M = W and Mo; T = S and Se) from first principles calculations. *RSC Advances*, 5(24):1839118400, 2015.

[218] Shaofeng Ge, Xuefeng Liu, Xiaofen Qiao, Qinsheng Wang, Zhen Xu, Jun Qiu, Ping-Heng Tan, Jimin Zhao, and Dong Sun. Coherent Longitudinal Acoustic Phonon Approaching THz Frequency in Multilayer Molybdenum Disulphide. *Scientific Reports*, 4, 2014.

[219] Satyaprakash Sahoo, Anand P. S. Gaur, Majid Ahmadi, Maxime J.-F. Guinel, and Ram S. Katiyar. Temperature-Dependent Raman Studies and Thermal Conductivity of Few-Layer MoS2. *The Journal of Physical Chemistry C*, 117(17):90429047, 2013.

[220] Insun Jo, Michael Thompson Pettes, Eric Ou, Wei Wu, and Li Shi. Basal-plane thermal conductivity of few-layer molybdenum disulfide. *Applied Physics Letters*, 104(20):201902, 2014.

[221] Rusen Yan, Jeffrey R. Simpson, Simone Bertolazzi, Jacopo Brivio, Michael Watson, Xufei Wu, Andras Kis, Tengfei Luo, Angela R. Hight Walker, and Huili Grace Xing. Thermal Conductivity of Monolayer Molybdenum Disulfide Obtained from Temperature-Dependent Raman Spectroscopy. *ACS Nano*, 8(1):986993, 2014.

[222] Jun Liu, Gyung-Min Choi, and David G. Cahill. Measurement of the anisotropic thermal conductivity of molybdenum disulfide by the time-resolved magneto-optic Kerr effect. *Journal of Applied Physics*, 116(23):233107, 2014.

[223] Xian Zhang, Dezheng Sun, Yilei Li, Gwan-Hyoung Lee, Xu Cui, Daniel Chenet, Yumeng You, Tony F. Heinz, and James C. Hone. Measurement of Lateral and Interfacial Thermal Conductivity of Single- and Bilayer MoS $_2$ and MoSe $_2$ Using Refined Optothermal Raman Technique. *ACS Applied Materials & Interfaces*, 7(46):2592325929, 2015.

[224] Wu Li, J. Carrete, and Natalio Mingo. Thermal conductivity and phonon linewidths of monolayer MoS2 from first principles. *Applied Physics Letters*, 103(25):253103, 2013.

[225] Yongqing Cai, Jinghua Lan, Gang Zhang, and Yong-Wei Zhang. Lattice vibrational modes and phonon thermal conductivity of monolayer MoS${}_{2}$. *Physical Review B*, 89(3):035438, 2014.

[226] Zhiwei Ding, Jin-Wu Jiang, Qing-Xiang Pei, and Yong-Wei Zhang. In-plane and cross-plane thermal conductivities of molybdenum disulfide. *Nanotechnology*, 26(6):065703, 2015.

[227] Xufei Wu, Nuo Yang, and Tengfei Luo. Unusual Isotope Effect on Thermal Transport of Single Layer Molybdenum Disulphide (MoS2). *arXiv preprint arXiv:1510.00693*, 2015.

[228] Xiaokun Gu, Baowen Li, and Ronggui Yang. Layer thickness-dependent phonon properties and thermal conductivity of MoS2. *arXiv preprint arXiv:1601.00227*, 2016.

[229] Akira Harata, Hiroyuki Nishimura, and Tsuguo Sawada. Lasernduced surface acoustic waves and photothermal surface gratings generated by crossing two pulsed laser beams. *Applied Physics Letters*, 57(2):132134, 1990.

[230] Jong-Young Kim, Soon-Mok Choi, Won-Seon Seo, and Woo-Seok Cho. Thermal and Electronic Properties of Exfoliated Metal Chalcogenides. *Bulletin of the Korean Chemical Society*, 31(11):32253227, 2010.

[231] Hang Zhang, Xiangwen Chen, Young-Dahl Jho, and Austin J. Minnich. Temperature Dependent Mean Free Path Spectra of Thermal Phonons Along the c-axis of Graphite. *arXiv:1509.05092 [cond-mat]*, 2015.

[232] Sangwook Lee, Fan Yang, Joonki Suh, Sijie Yang, Yeonbae Lee, Guo Li, Hwan Sung Choe, Aslihan Suslu, Yabin Chen, Changhyun Ko, Joonsuk Park, Kai Liu, Jingbo Li, Kedar Hippalgaonkar, Jeffrey J. Urban, Sefaattin Tongay, and Junqiao Wu. Anisotropic in-plane thermal conductivity of black phosphorus nanoribbons at temperatures higher than 100 K. *Nature Communications*, 6:8573, October 2015.

[233] Hamidreza Chalabi, Erez Hasman, and Mark L. Brongersma. Near-field radiative thermal transfer between a nanostructured periodic material and a planar substrate. *Physical Review B*, 91(1):014302, January 2015.

[234] Vazrik Chiloyan, Jivtesh Garg, Keivan Esfarjani, and Gang Chen. Transition from near-field thermal radiation to phonon heat conduction at sub-nanometre gaps. *Nature Communications*, 6, April 2015.

[235] Kyeongtae Kim, Bai Song, Vctor Fernndez-Hurtado, Woochul Lee, Wonho Jeong, Longji Cui, Dakotah Thompson, Johannes Feist, M. T. Homer Reid, Francisco J. Garca-Vidal, Juan Carlos Cuevas, Edgar Meyhofer, and Pramod Reddy. Radiative heat transfer in the extreme near field. *Nature*, advance online publication, December 2015.

[236] Baoan Liu, Yongmin Liu, and Sheng Shen. Thermal plasmonic interconnects in graphene. *Physical Review B*, 90(19):195411, 2014.

[237] Kaifeng Chen, Parthiban Santhanam, Sunil Sandhu, Linxiao Zhu, and Shanhui Fan. Heat-flux control and solid-state cooling by regulating chemical poten-

tial of photons in near-field electromagnetic heat transfer. *Physical Review B*, 91(13):134301, 2015.

[238] P. T. Landsberg and G. Tonge. Thermodynamic energy conversion efficiencies. *Journal of Applied Physics*, 51(7):R1R20, 1980.

[239] Chengyun Hua and Austin J. Minnich. Transport regimes in quasiballistic heat conduction. *Physical Review B*, 89(9):094302, 2014.

[240] A. J. Minnich. Multidimensional quasiballistic thermal transport in transient grating spectroscopy. *Physical Review B*, 92(8):085203, August 2015.

[241] M. R. Null, W. W. Lozier, and A. W. Moore. Thermal diffusivity and thermal conductivity of pyrolytic graphite from 300 to 2700 K. *Carbon*, 11(2):8187, 1973.

[242] Joseph P. Feser and David G. Cahill. Probing anisotropic heat transport using time-domain thermoreflectance with offset laser spots. *Review of Scientific Instruments*, 83(10):104901, 2012.

[243] Insun Jo, Michael T. Pettes, Lucas Lindsay, Eric Ou, Annie Weathers, Arden L. Moore, Zhen Yao, and Li Shi. Reexamination of basal plane thermal conductivity of suspended graphene samples measured by electro-thermal micro-bridge methods. *AIP Advances*, 5(5):053206, 2015.

[244] A. J. Minnich. Phonon heat conduction in layered anisotropic crystals. *Physical Review B*, 91(8):085206, 2015.